TECHNISCHE
UNIVERSITÄT
WIEN
Vienna University of Technology

Diplomarbeit

Influence of Roughness on Sputter Yields of Tungsten-Coatings relevant for Nuclear Fusion Devices

zur Erlangung des akademischen Grades
Diplom-Ingenieur
im Rahmen des Studiums
Physikalische Energie- und Messtechnik

eingereicht von
Christian CUPAK, BSc.
Schlachthausgasse 41/1/23
1030 Wien

Ausgeführt am
Institut für Angewandte Physik
der Technischen Universität Wien
Wiedner Hauptstraße 8-10 / E134
1040 Wien

unter der Anleitung von
Univ. Prof. Dr. Friedrich AUMAYR
Ing. Dipl.-Ing. Reinhard STADLMAYR, BSc.

Wien, am 2. Dezember 2019

Prof. Friedrich Aumayr

Christian Cupak, BSc.

Kurzfassung

Kernfusionsreaktoren haben das Potential, in der Zukunft einen grundlegenden Beitrag zur Energieversorgung für die Menschheit zu liefern. Für einen effizienten Betrieb eines solchen Kraftwerks ergeben sich äußerst intensive physikalische Bedingungen im Inneren des Reaktors, welche hohe Anforderungen an potentielle Materialien für die Reaktorwand darstellen. Es ist somit von fundamentalem Interesse, die Wechselwirkungen zwischen Plasmateilchen und möglichen Wandmaterialien zu untersuchen. Eigenschaften wie die Erosionsbeständigkeit unter Ionenbeschuss stellen ein wichtiges Auswahlkriterium dar, da abgetragene Wandpartikel im Plasma zu massiven Auswirkungen auf die Effizienz des Energieeinschlusses führen können. Wolfram hat vorteilhafte Eigenschaften, wie zum Beispiel den höchsten Schmelzpunkt aller Metalle, niedrige Lösbarkeit von Wasserstoffisotopen, sowie eine vergleichbar niedrige Zerstäubungsrate (Sputter Yield), welche die physikalische Größe zur Beschreibung von Erosion unter Partikelbeschuss ist. Aus diesem Grunde ist Wolfram auch im Fokus der aktuellen Kernfusionsforschung.

Das grundlegende Ziel dieser Diplomarbeit war, die Zerstäubungsrate für Wolframschichten mit variablen Oberflächenrauhigkeiten zu ermitteln. Der Einfluss von Rauhigkeit auf die Zerstäubungsrate ist von grundlegendem Interesse, da auch für die innere Reaktorwand eines zukünftigen Kernfusionskraftwerks eine gewisse technische Rauhigkeit angenommen werden kann. Die Methode der Quartzkristall-Mikrowaage (QCM) bietet die Möglichkeit, Zerstäubungsraten direkt zu messen, wobei jedoch die Proben für den Ionenbeschuss in Form von beschichteten Quarzkristallen vorliegen müssen. Um diese Limitation zu umgehen, wurde ein neuer und flexibler Fänger-QCM-Apparat gebaut, mit dem eine Bestimmung der Zerstäubungsrate von den gewünschten Wolframschichten ermöglicht wurde. Nachdem diese Wolframschichten bezüglich ihrer Rauhigkeit und elementarer Zusammensetzung charakterisiert wurden, sind Experimente mithilfe von 2 keV Ar^{1+} Ionen unter einem Einfallswinkel von 60° im Ultrahochvakuum durchgeführt worden. Des Weiteren wurden die experimentellen Ergebnisse mit Daten aus numerischen Simulationen verglichen, die auf Basis des Binary Collision Approximation (BCA) Codes *TRI3DYN* durchgeführt wurden.

Die Resultate dieser Diplomarbeit wurden weiters für den wissenschaftlichen Fortschritt des europäischen Kernfusionsforschungsnetzwerks *EUROfusion* berücksichtigt, welches die grundlegenden Ziele für diese Untersuchungen in der Kampagne *PFC-SP 2.4.2* definiert hatte.

Abstract

Nuclear fusion reactors have the potential to become a major energy source for humanity in future. Due to the intense physical conditions necessary for adequate energy yields, high requirements on first-wall coatings at the inside of a fusion reactor are demanded. It is therefore of fundamental interest to investigate the interactions of plasma particles with probable first wall materials. Properties regarding erosion under ion bombardment form a crucial selection criteria for utilisation, since eroded wall atoms drastically decrease the energy confinement efficiency of the plasma in the vessel. Tungsten has advantageous characteristics, like the highest melting point of all metals, low solubility for hydrogen isotopes and a comparable low sputter yield, which is the physical quantity describing the erosion by particle impact. Therefore, this material is in focus of current nuclear fusion research.

In the course of this diploma thesis, the sputter yield of tungsten coatings with varying surface roughness had to be determined. Roughness effects are of fundamental interest, since a technical rough surface finish also has to be expected for the first wall of a future fusion power plant. The Quartz Crystal Microbalance (QCM) technique offers a direct determination of sputter yields, but is limited to coated quartz crystals as target samples for ion bombardment only. Via development of a new flexible catcher - QCM apparatus, this limitation was successfully circumvented and provided a basis for sputter yield determination of the desired samples. After initial sample characterisation regarding surface topography and elemental composition, the main experiments were executed via bombardment of the tungsten coatings utilising 2 keV Ar^{1+} ions under 60° angle of incidence under Ultra High Vacuum (UHV) conditions. In addition, the experimental results were compared to numerical simulation data originating from the BCA code *TRI3DYN*.

The outcome of this thesis contributed to the scientific progress of the European nuclear fusion research network *EUROfusion*, which defined a corresponding key task in the collaborative campaign *PFC-SP 2.4.2*.

Contents

1 Introduction

Energy. A word which is widely used in regular conversations and commonly known for a vast majority of people on earth. The popularity of it is certainly based on an intuitive interpretation of the underlying physical concept. It is easy to observe energy transformation processes for everyone in daily life, like for instance by transforming the potential energy of a stone positioned in relative height to the ground into kinetic energy by dropping it.
Physically speaking, energy is the quantity which describes the capacity of a physical system for executing work. Therefore, there is always energy transformation behind dynamic processes in nature. This is also the reason, why it is crucial for a civilisation to master several energy transformation processes in order to reach further steps in development. For humans, one of the first groundbreaking discoveries of a new energy transformation method was made approximately 1.5 million years ago, when our early ancestors started to utilise controlled fires for cooking, protection against wild animals and for heating their shelters [1]. Since then, subsequent steps of perfectionisation provided further basis for various modern technologies, like the steam turbine, the combustion engine or space rockets. During the last centuries, discoveries and innovations in energy technology supported fundamental societal and economical developments. This further led to an ongoing steep increase of energy resource demand.
The following figure 1.1 provides an overview on the historic evolution of total energy resource demand based on data provided by the *International Energy Agency (IEA)* [2]. Between 1971 and 2017, the amount of primary energy resource consumption increased from approximately 5500 Megaton oil equivalents (Mtoe) to more than 13500 Mtoe. This trend is not expected to change in the next years, since driving forces for energy resource consumption like economic development or the increase of world population are ongoing.
Even though various energy technologies are available nowadays, the major primary resources used for heating, electricity generation and mobility are fossil fuels like coal, crude oil or natural gas [2]. Within the last decades and especially during the latest years, an increased public sensibility for environmental protection and climate change emphasised many governments to include topics like renewable energies to their political agenda. A drawback of common renewable energy technologies, like wind power or photovoltaic systems, is the high volatility of energy production due to the fluctuations in wind or solar radiation availability. It is therefore of fundamental interest to develop new energy concepts which meet criteria like high security of supply, tolerable environmental impact and also scalability.

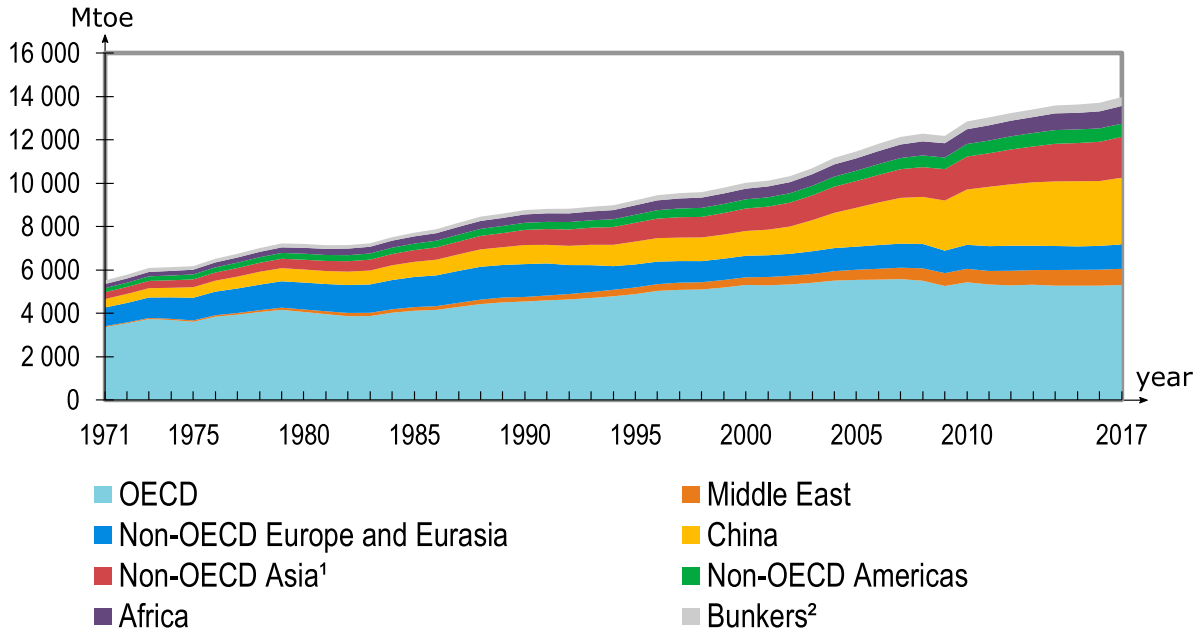

Figure 1.1 – World total primary energy supply for different regions between 1971 to 2017. The unit Mtoe corresponds to the amount of heat released by burning 1.0×10^6 tons of oil. OECD is an acronym for *Organisation for Economic Co-operation and Development*. Bunkers indicate backup fuel tanks. Graph is taken from the IEA Statistics Report 2019 [2].

Nuclear fusion is expected to meet these criteria. The fuel for the underlying fusion reaction consists of deuterium and tritium. While deuterium is almost globally available via extraction from seawater, tritium is intended to get produced on-site in a so-called breeding blanket [3,4]. The expected electrical output powers are in the order of Gigawatts on a base-load scenario, which provides a good opportunity for substitution of big coal, oil or nuclear fission power plants. Also, the fusion reaction does not produce CO_2 or other emission of green house gases. Even though a fusion power plant on the basis of a deuterium - tritium reaction will definitely be a radioactive facility, the reaction product is the stable isotope ${}^4_2\mathrm{He}$. This constitutes an advantage in comparison to nuclear fission power plants, where various fission products with long radioactive decay times imply problems in terms of permanent and safe storage for thousands of years [5]. Intended for a first demonstration of net-energy production, the research fusion reactor ITER currently being built in France should start operation by the end of 2025 [6].
Substantial gains in the field of nuclear fusion research were achieved during the last decades, but there are still many challenges to solve. One big task is to understand and solve erosion issues of first wall materials in a fusion device. This master thesis should therefore support developments towards an operating nuclear fusion reactor.
In section 1.1 a brief overview on nuclear fusion is given, before section 1.2 provides a detailed scientific motivation of this thesis. Section 1.3 offers an outline of the whole document, accompanied by a list of published contributions and scientific journeys undertaken during this project in section 1.4.

1.1 Nuclear Fusion

Nuclear fusion describes the physical unification process of two atom nuclei. By principle, not only Coulomb force but also the strong interaction force of the nuclei plays a role in such a process. This is a fundamental difference to chemical reactions, which base on interactions between electrons bound in atoms or molecules. Generally, there is a wide variety of possible fusion reactions, while only some of them yield a significant exothermic energy release. The nuclear binding energy of a nucleus is an important quantity for the determination of energy released by such a reaction. Based on experiments, figure 1.2 shows the nuclear binding energy per nucleon over increasing atomic mass number A [7].

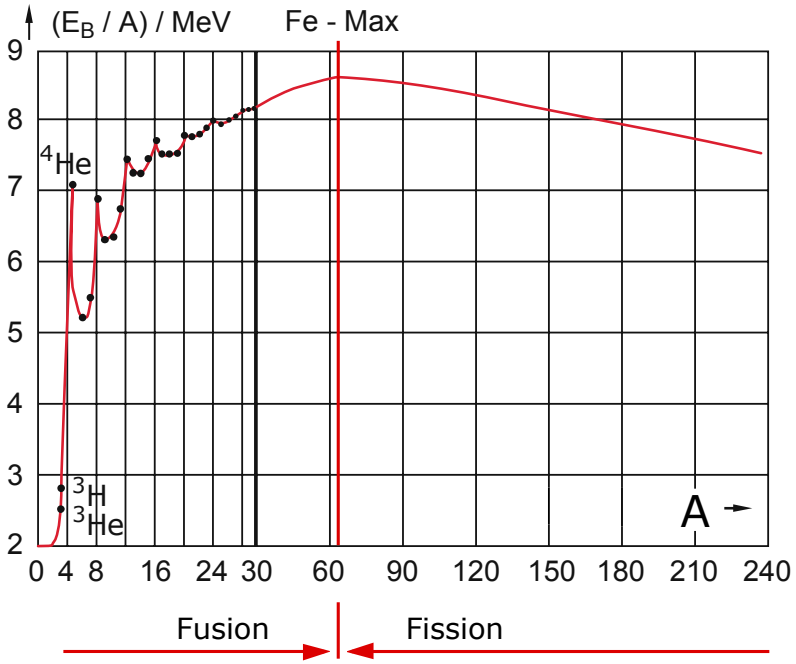

Figure 1.2 – Nuclear binding energy per nucleon as a function of atomic mass number A. Graph taken and modified from reference [7].

Principally, two options for nuclear reactions with an energy gain are possible in this picture:

- A very heavy nucleus decays into two or more smaller residual nuclei (nuclear fission)
- Two or more light nuclei form a heavier nucleus (nuclear fusion)

The difference of product and educt binding energy ΔE_B is equal to a mass defect of the involved nuclei according to Einstein's relation:

$$\Delta E_B = \Delta m \cdot c^2 \tag{1.1.1}$$

ΔE_B is released in form of kinetic energy via the resulting product nuclei. It has to be mentioned, that the energy values for these reactions are in the order of mega electron volt (MeV), compared to energies of electron volt (eV) released during a chemical reaction like oxidation. Therefore, the theoretical energy densities of fusion and fission fuels are much higher than for conventional fuels.
One of the most prominent fusion reactions is performed in the central celestial body of our solar system - the sun. Here, protons undergo fusion reactions at temperatures up to 15×10^6 K and pressures of 10^{16} Pa in the so-called pp-cycle, which yields a final ${}^4_2$He nucleus and exothermal energy [8]. The resulting radiant energy of our sun is furthermore the fundamental origin for most energy resources on earth. Photovoltaic systems and wind power, but also hydro energy and (fossil) biofuels are a direct result of energy transformation processes starting from radiated energy of the sun. Even nuclear fission fuels like ${}^{235}_{92}$U originate from an endothermal fusion process during a supernova long time before our solar system was formed [9].
Even though the pp-cycle is the driving reaction inside the sun, it is not assumed as a probable reaction in a fusion reactor on earth. The reaction rate of the total pp-chain is very low, since the reaction cross section for proton fusion is even low inside the comparable hot and dense centre of the sun. This is equalised in numbers by the huge mass of the sun and a long confinement time (see next section) due to gravitation. For a technical utilisation, other approaches are necessary to gain reasonable energy outputs.

1.1.1 The D-T Reaction and the Triple Product

Within the field of nuclear fusion research, the deuterium-tritium (D-T) reaction is prominent for a high total energy output and a comparable high reaction rate coefficient. This reaction reads as follows:

$$ {}^2_1D \; + \; {}^3_1T \; \Rightarrow \; {}^4_2He \; + \; {}^1_0n \; + \; 17.6\,\mathrm{MeV} \tag{1.1.2} $$

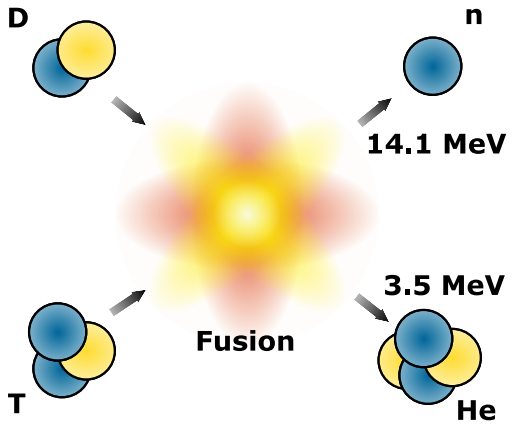

Figure 1.3 – Fusion reaction by deuterium and tritium.

The total energy of 17.6 MeV is released in form of the reaction products kinetic energy, which is illustrated in figure 1.3. $^4_2$He receives 3.5 MeV while the residual 14.1 MeV are transferred to the neutron. In order to successfully perform a nuclear fusion reaction, the initial D and T nuclei need to overcome the so-called Coulomb barrier. Since the Coulomb potential of two positive charges is long-ranging and repelling, a high kinetic energy of the initial particles is needed during a collision, so that the strong but short-ranged nuclear force can gain influence. The tunnelling effect enables significant reaction rates already at lower kinetic energies then expected from the classical collision theory [10].
Via the following equation, the total power density p_{fus} of a nuclear fusion device can be written with usage of the mean plasma density $\bar{n}$, the temperature dependent rate coefficient $\langle \sigma_{fus} u \rangle$ and the total energy release from a single fusion reaction ΔE_{D-T}.

$$\frac{\bar{n}^2}{2} \cdot \langle \sigma_{fus} u \rangle (T) \cdot \Delta E_{D-T} = p_{fus}(\bar{n}, T) \tag{1.1.3}$$

The neutron can't get captured within magnetic confinement systems (see more in section 1.1.2) as it has no charge. Nevertheless, the kinetic neutron energy can still get transferred to the first wall of a reactor and is therefore available for the total energy output calculation. In order to reach a self sustaining thermonuclear reaction, only the helium atom energy is considerable, since the ion remains in the plasma and also distributes it's kinetic energy to other plasma particles via scattering events. The equation 1.1.3 can be modified for the kinetic energy of $^4_2$He only to derivate a power balance criterion. Main energy loss effects induced by radiating impurities or transport losses need to be compensated by fusion power dissipated by $^4_2$He ions, which can be written via a triple product [10].

$$\bar{n} \cdot \bar{T} \cdot \tau_E \quad \left[eV \cdot s \cdot m^{-3} \right] > 3 \times 10^{24} \tag{1.1.4}$$

In equation 1.1.4, the parameters $\bar{n}$ and $\bar{T}$ represent the mean density and mean temperature of the plasma, while τ_E denotes the characteristic energy confinement time of the reactor system. If the triple product of a certain configuration satisfies equation 1.1.4, the plasma is called *ignited* and would in principle provide conditions for a self sustaining fusion reaction without any need of auxillary heating systems. Nevertheless, additional loss effects like Bremsstrahlung further increase the necessary triple product value. Until now, a full ignition of a plasma was not yet achieved and auxillary heating systems were necessary during the whole time in fusion experiments. Another important quantity for fusion research is the Q-value, which describes the ratio between total power gained from fusion P_{fus} and the auxiliary power P_{aux}.

$$Q = \frac{P_{fus}}{P_{aux}} \quad \propto \quad \bar{n} \cdot \bar{T} \cdot \tau_E \tag{1.1.5}$$

A main goal for future experiments with the next big fusion device ITER is to reach levels of $Q \geq 10$. This would constitute a first demonstration of net energy production via nuclear fusion, even though auxiliary heating systems are still necessary and no intentions for actual electricity production by ITER are considered in the moment [11]. More details regarding nuclear fusion can be found in the following references [6, 10].

1.1.2 Tokamak Reactor Concept

In this section, a short overview on the technological fusion reactor concept called TOKAMAK is given. It was developed 1952 in Moscow and is a prominent representative of magnetic confinement systems [12]. Compared to other concepts it is the most developed reactor type. Figure 1.4 shows a simplified sketch of the TOKAMAK and its fundamental components.

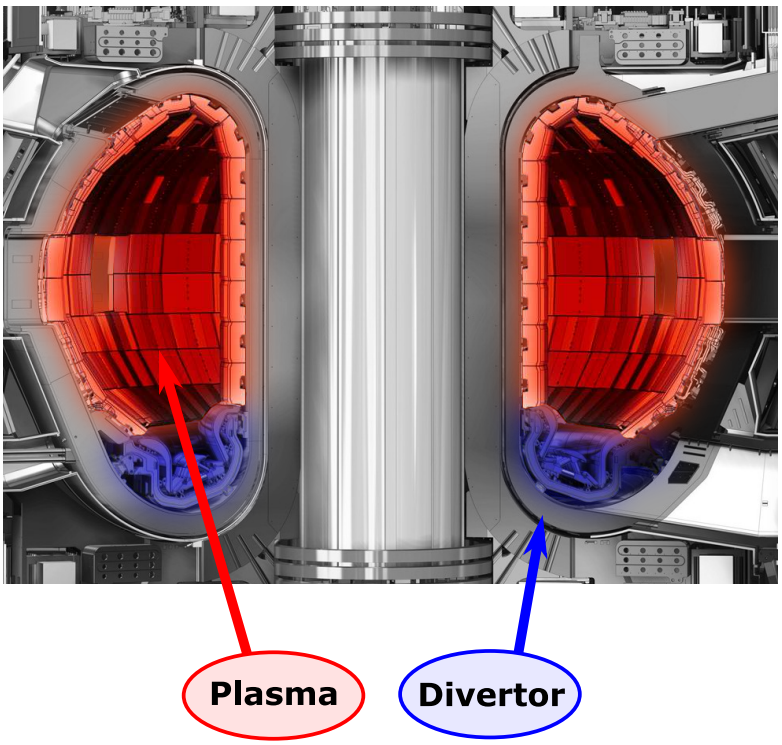

Figure 1.4 – Cross section of the TOKAMAK concept. Picture taken from [6].

The primary transformer in the centre drives a current through the plasma, which is a characteristic property of the TOKAMAK. Toroidal field coils force the ions to gyrate around toroidal magnetic field lines, which are further twisted via superposition with the induced poloidal magnetic field from the plasma current. This supports the confinement of charged plasma particles. Additional vertical field coils are used to further shape the plasma. Fuel and heat exchange will be done by utilisation of a tungsten divertor (blue in 1.4), where the last closed magnetic field lines are ending and seeding gases like argon are used to distribute the heat load onto the wall [13, 14].
Also ITER will be a TOKAMAK with a major radius of 6.2 metres. Next to the $Q \geq 10$ criterion, technological concepts like the tritium breeding blanket and first wall materials will be tested. Furthermore, ITER constitutes an intermediate step towards a first nuclear fusion power plant called DEMO, which should finally produce electric energy and prove technical applicability of nuclear fusion as energy source [15].

1.2 Motivation of the Thesis

A comparable low sputtering yield, high melting point and low solubility for hydrogen isotopes are favourable properties of tungsten, which accentuates it's utilisation as a first wall material especially in the divertor region of a future fusion reactor. Here, high heat loads up to 20 MW per m^2, neutron damage, but also sputter erosion via ions originating from the fuel (deuterium or tritium) or seeding gas (nitrogen or argon) have to be faced. Off-sputtered tungsten wall atoms are unfavourable inside the fusion reactor, since they cool down the plasma via strong radiant energy emission. Therefore, tungsten and it's properties are under current investigation within nuclear fusion research, which is also expressed in the scientific work task *PFC-SP 2.4.2* organised by the *EUROfusion* research network [16]. In detail, experimental data regarding the sputter yield of tungsten for samples with different surface roughness values is desired. The influence of surface topology on erosion processes of plasma facing components is highly relevant for a technical utilisation, since it can be estimated that a vessel coating of a future fusion reactor will have a technical roughness.
The main goal of this master thesis was therefore to develop a dedicated experimental method for (indirect) sputter yield measurements. A catcher QCM technique should provide a basis for such an apparatus, and successful application has to be demonstrated in-situ by investigation of tungsten coatings with variable surface roughness values exposed to argon ion bombardment under UHV conditions.
In addition, a comparison between selected experimental results and numerical data from simulations should complement the outcome of this thesis.

1.3 Outline

Within this chapter, a short introduction to the scientific frame of this master thesis was given. As a next step, chapter 2 offers theoretical background to the physical effects of sputtering by ion bombardment. In addition, the theory of sputter yield measurements via the QCM method is provided, before an overview on numerical simulation methods for ion solid interactions is shortly sketched. Chapter 3 highlights properties of the experimental setup and also offers details regarding the executed measurement procedure during the investigations. Then, a focus is set on the characteristics and preparation of the utilised tungsten samples in chapter 4. In the following, chapter 5 provides results of the experiments, before a comparison with data from numerical simulations performed by *Reinhard Stadlmayr* (Institute of Applied Physics, TU WIEN) is shown in chapter 6 thereafter. This is a basis for chapter 7, which summarises the main conclusions obtained from this project including limitations and ideas for further investigations. In addition to the main part of this document, a short overview on general project management statistics is provided in the appendix, before a set of experimental details and technical drawings is added as a backup for future projects.

1.4 Scientific Experiences

This section highlights the contribution of results obtained within this master project for scientific projects and publications. Some results are intended to get published in a scientific journal after completion of the thesis. In addition, experimental work executed in the course of scientific journeys contributed also to research projects which reached even further than the scope of this master thesis.

Publications in Scientific Journals:

R. Stadlmayr, P. S. Szabo, C. Cupak, D. Mayer, T. Dittmar, L. Bischof, S. Möller, M. Rasinski, R. A. Wilhelm, W. Möller and F. Aumayr. *Sputtering of nanostructured tungsten and comparison to modelling with TRI3DYN.* Journal of Nuclear Materials (2019), submitted.

Talks:

C. Cupak, R. Stadlmayr, P.S. Szabo, H. Biber, D. Mayer, F. Aumayr
EUROfusion PFC-SP2 annual meeting: "Erosion Studies with the Vienna QCM"
TU WIEN + European research partner institutions (Online Meeting), 2019

Scientific Journeys:

Uppsala Universitet, Department of Physics and Astronomy, Prof. Daniel Primetzhofer
Experimental campaign: In-situ measurement of implanted H concentrations in thin W-films via NRA and simultaneous TDS investigation, TOF-ERDA measurements
Uppsala (Sweden) from 11/06/2019 - 20/06/2019

Max Planck Institute for Plasma Physics
IPP Summer University for Plasma Physics and Fusion Research
Garching (Germany) from 16/09/2019 - 20/09/2019

Uppsala Universitet, Department of Physics and Astronomy, Prof. Daniel Primetzhofer
Experimental campaign: In-situ measurement of implanted D concentrations in W bulk samples via ERDA and simultaneous TDS investigation
Uppsala (Sweden) from 29/09/2019 - 05/10/2019

2 Theory of Sputtering by Ion Impact

This chapter provides theoretical background to the physical effects which were investigated in the course of this thesis. In the beginning, a short overview on general aspects and characteristic quantities of ion induced sputter processes is given in section 2.1. In the following, section 2.2 offers detailed insights into the theory of sputter yield measurement via the utilised QCM technique. Complementary, an introduction to the theoretical concepts behind the simulation code *TRI3DYN*, which delivered several numerical results within this thesis, is offered in section 2.3.

2.1 Overview on Sputtering Processes

Sputtering is a prominent effect induced by particle impingment on solid materials. It describes the erosion which occurs during the bombardment and is quantitatively characterised via the so-called sputter yield. The definition of this quantity reads as follows:

$$Y = \frac{\text{mean number of sputtered atoms}}{\text{incident particle}} \tag{2.1.1}$$

If an incident projectile reaches the surface of the target, a so called collision cascade is initiated. Via subsequent collisions between projectile and target particles, linear momentum and also kinetic energy is transferred. If the collision cascade propagates back towards the surface of the target, sputtering can occur [17]. A successful sputtering event demands on one side a perpendicular component of the atom's linear momentum respective to the surface plane. Furthermore, sufficient kinetic energy is needed to overcome the surface binding energy of the target material, which is often denoted as *threshold* energy [18]. This process is also called *kinetic* sputtering and is visualised in figure 2.1. The kinetic sputter yield depends on both incident angle ϕ and kinetic energy of the incoming projectiles. In addition, the atomic mass ratio between target and projectile atoms is a significant parameter as well. Kinetic sputtering is the most relevant effect for material erosion processes which were investigated in the course of this thesis.
Once sputtered particles have left the target surface, they propagate further into space in the direction of their linear momentum. The angular distribution of those sputtered particles is significantly influenced by surface topology, as recent experiment and numerical studies have shown [20]. An example for various effects on rough surfaces is shown in figure 2.2. Since the

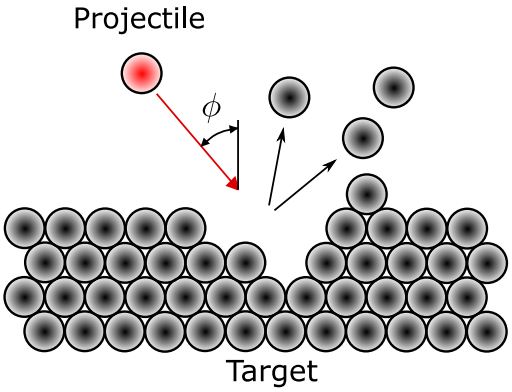

Figure 2.1 – Sketch of kinetic sputtering process induced by ion impact under incident angle ϕ. Picture taken and modified from reference [19].

sputter yield depends on the incident angle of a respective ion (see figure 2.2 A), the local ion incident angle distribution forms a dependency for the total sputter yield. Dependent on the global incident angle of the ion beam ϕ, more or less regions of the surface are shadowed (figure 2.2 B) from direct ion impact. For increasing local incident angles, ion reflection can become more dominant (figure 2.2 C). Furthermore, re-deposition effects (figure 2.2 D) can lead to reduced total sputter yields, especially for comparable rough surfaces [21, 22].

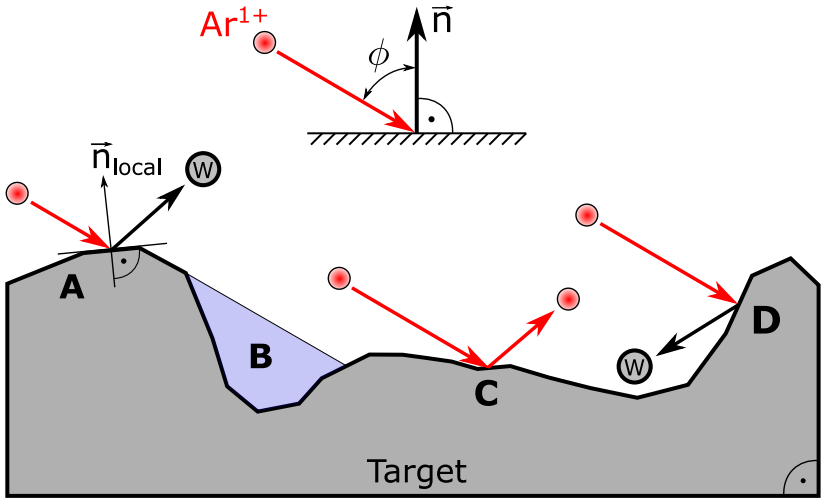

Figure 2.2 – Sketch of a rough surface under ion bombardment. Ar^{1+} ions imping under incident angle ϕ respective to the global surface normal $\vec{n}$. A - Sputtering of W atom via ion impact at local position, B - Region shadowed from ions due to surface structure, C - Ion reflection, D - Redeposition of W atom initially sputtered by ion.

Opportunities for description of a surface topography are quantitative values like the roughness value R_Q or the surface inclination distribution (distribution of local impact angles).

Generally, the effect of re-deposition can be expected to become stronger for higher R_Q values and for inclination distributions with preference on steeper angles, as has been found by *Küstner et. al.* 1998 [21]. Here, roughness effects led to redeposition of sputtered particles by about 25%. In addition, the total sputter yield of rough surfaces, having a broad Full Width Half Maximum (FWHM) of the inclination distributions, was much less dependent on the incident angle ϕ of the ion beam than for smoother samples. A good agreement between numerical Monte-Carlo simulations and experimental data obtained by measurements with graphite samples was shown as well. Studies on the sputter yield of molybdenum samples by *Li et al.* [23], where also a QCM method was utilised, did show decreases of the target sputter yield for rougher samples at low ion fluence of 1.0×10^{20} ions/m^2. In addition, significant changes in the off-sputtered particles angular distribution in comparison with flat molybdenum targets was recognised, highlighting a strong effect of surface topology on the kinetic sputtering process.
Next to kinetic sputtering and surface topology effects, there are also other phenomena based on ion induced sputtering which are of interest in research. Especially for highly charged ions at comparably low kinetic energies, the so-called *potential* sputtering effect can occur and drastically change the total sputter yield for electrically insulating target materials [24]. Another prominent effect is *preferential* sputtering, which is relevant for target materials which consist of more than one element. Here, different sputter yields for each elemental component can lead to dynamic processes like surface composition changes [25]. Since the experiments executed during this thesis were focusing on bombardments by Ar^{1+} ions on tungsten coatings with high purity, effects like potential and preferential sputtering were assumed to play a rather small role. For further insights into sputter processes and ion - solid interaction theory in general, please compare further literature [17].

2.2 Theory of QCM Measurement Technique

A Quartz Crystal Microbalance (QCM) is a sensitive method for measuring small mass change rates down to the order of 10^{-9} g/s. At the *TU WIEN*, already substantial experience was made by various in-situ utilisations of this method for ion induced erosion and deposition studies [26–28]. In order to provide a theoretical background for this method, a derivation of the fundamental quantities is offered.
The main sensor component of every QCM is a quartz crystal platelet, which has to be coated with a thin film of the desired target material of interest. Via the piezoelectric effect, a resonant thickness shear mode with characteristic eigenfrequency f_0 can get excited by application of a suitable alternating electrical current through the quartz (see figure 2.3 for an illustration). For erosion studies, the target quartz is exposed to an ion beam and the coating will decrease in thickness. The quartz's resonance frequency will rise by Δf during the bombardment time Δt, as it is linked to a decrease of thickness Δd and therefore mass change Δm. A mathematical relation between mass, thickness and frequency change is given via the Sauerbrey equation [29]:

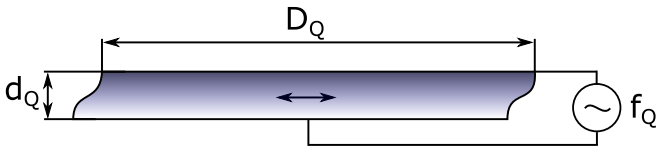

Figure 2.3 – Sketch of a quartz crystal driven at resonance frequency f_Q. Dimension d_Q denotes the crystal's thickness. Via the quartz diameter D_Q, one can calculate the surface area A_Q.

$$\frac{\Delta m}{m_Q} = \frac{\Delta d}{d_Q} = -\frac{\Delta f}{f_Q} \tag{2.2.1}$$

In equation (2.2.1), m_Q, d_Q and f_Q denote known quantities like the total mass, thickness and eigenfrequency of the quartz, respectively. One can therefore calculate the temporal mass change $\Delta m(\Delta t)$ by accurate measurement of $\Delta f(\Delta t)$, which is technically achievable via dedicated electronic circuits [30]. It is important to mention, that equation (2.1.1) is only satisfied if the coating is much thinner in comparison to the total thickness of the quartz. Furthermore, deviations were found for inhomogeneous irradiation beam profiles, as the radial quartz sensitivity is a Gaussian function of the distance between ion impact position and quartz centre [31, 32].
Via usage of the quartz surface area A_Q and the atomic mass unit m_0, the occurring mass change can be formulated in atomic mass units per unit area in equation (2.2.2):

$$\Delta m_{amu}(\Delta t) \left[\frac{amu}{cm^2}\right] = \frac{\Delta m(\Delta t)}{A_Q \cdot m_0} \tag{2.2.2}$$

Equation (2.2.2) can get further modified by insertion of (2.2.1) and $m_Q = A_Q \cdot d_Q \cdot \rho_Q$:

$$\Delta m_{amu}(\Delta t) = -\frac{\Delta f(\Delta t) \cdot m_Q}{A_Q \cdot m_0 \cdot f_Q} = -\frac{\Delta f(\Delta t) \cdot d_Q \cdot \rho_Q}{m_0 \cdot f_Q} \tag{2.2.3}$$

The quantity ρ_Q denotes the quartz mass density. In order to transform $\Delta m_{amu}(\Delta t)$ into a sputter yield formulation, following assumptions for the ion beam were made. As one can see in equation (2.1.1), the total number of incident particles impinging onto the target during bombardment time Δt is of importance. If the ion beam current density j_c is known, a calculation of the total amount of incident ions per unit area is feasible:

$$N_{ions}(\Delta t) \left[\frac{ions}{cm^2}\right] = \frac{\int_{t_1}^{t_2} j_c \cdot dt}{q \cdot e_0} \qquad t_2 = t_1 + \Delta t \tag{2.2.4}$$

Here, q represents the charge state of the ion and e_0 indicates the elementary charge. The parameters t_1 and t_2 highlight start and end time of ion bombardment, respectively. If j_c is

constant over time, equation (2.2.4) simplifies to the following expression:

$$N_{ions}(\Delta t) = \frac{j_c \cdot \Delta t}{q \cdot e_0} \tag{2.2.5}$$

This formulation can now get used to define the mass removal per incident ion y. By division of (2.2.3) via (2.2.5), following expression is obtained:

$$y \left[\frac{amu}{ion}\right] = -\frac{\Delta m_{amu}(\Delta t)}{N_{ions}(\Delta t)}$$

$$y = \frac{\Delta f(\Delta t)}{\Delta t} \cdot \frac{1}{j_c} \cdot \frac{q \cdot e_0 \cdot d_q \cdot \rho_Q}{m_0 \cdot f_Q} \tag{2.2.6}$$

The negative sign in the definition of y is introduced in order to attribute positive values to mass removals. The equation is valid for pure targets and also for any kind of composite coatings, as it denotes a total mass change in amu/ion. Since the coatings investigated in the course of this thesis consisted of tungsten only, the mass removal per ion y can directly get transformed into the formulation of a tungsten target sputter yield Y_T. For this, the atomic mass of tungsten needs to be considered, which is $m_W = 183.84$u.

$$Y_T \left[\frac{W\ atoms}{ion}\right] = \frac{y}{m_W}$$

$$Y_T = \frac{\Delta f(\Delta t)}{\Delta t} \cdot \frac{1}{j_c} \cdot \frac{q \cdot e_0 \cdot d_q \cdot \rho_Q}{m_0 \cdot f_Q \cdot m_W} \tag{2.2.7}$$

In (2.2.7), several constants can get substituted via introduction of a global constant C_1, which yields a simplified equation for the sputter yield of tungsten:

$$Y_T = \frac{\Delta f(\Delta t)}{\Delta t} \cdot \frac{1}{j_c} \cdot C_1 \tag{2.2.8}$$

$$C_1 = \frac{q \cdot e_0 \cdot d_q \cdot \rho_Q}{m_0 \cdot f_Q \cdot m_W} \tag{2.2.9}$$

Equation (2.2.8) is utilised for sputter yield determination during direct ion impact on coated quartz targets, which are called *Target* sputter yield measurements in the course of this project. This approach was mainly used to determine the sputter yield of a reference quartz crystal, which formed a basis for interpretation of data originating from other targets (see chapter 5).

In contrast to direct sputter yield investigations, the QCM method can also get used to determine mass increase from atoms deposited on a quartz surface. This was used to investigate angular distributions of sputtered tungsten atoms from a primary target, which is denoted as *Catcher* yield measurement in this thesis. For a derivation of the catcher yield Y_C, some modifications of the upper equations have to be obtained. Similar to definition (2.1.1), the catcher yield can be interpreted as the mean number of deposited (tungsten) atoms per ion impinging the primary target. Thus, the total number of ions incoming during the bombardment time Δt is necessary. In this view, the total ion current I_c applied within the ion beam scan area A_{scan} can substitute j_c in equation (2.2.5), which delivers:

$$I_c = j_c \cdot A_{scan} \tag{2.2.10}$$

$$N_{ions}^{tot}(\Delta t) \ \left[ions\right] \ = \frac{I_c \cdot \Delta t}{q \cdot e_0} \tag{2.2.11}$$

Similar to (2.2.2), the total mass change during Δt in atomic mass units is written as:

$$\Delta m_{amu}^{tot}(\Delta t) \ \left[amu\right] \ = \frac{\Delta m(\Delta t)}{m_0}$$

$$\Delta m_{amu}^{tot}(\Delta t) = - \frac{\Delta f(\Delta t) \cdot A_Q \cdot d_Q \cdot \rho_Q}{m_0 \cdot f_Q} \tag{2.2.12}$$

Division of (2.2.12) via (2.2.11) and consideration of the atomic mass of tungsten m_W provides a catcher yield formula as follows:

$$Y_C = - \frac{\Delta f(\Delta t)}{\Delta t} \ \cdot \ \frac{1}{I_c} \ \cdot \ C_2 \tag{2.2.13}$$

$$C_2 = \frac{q \cdot e_0 \cdot A_Q \cdot d_q \cdot \rho_Q}{m_0 \cdot f_Q \cdot m_W} \tag{2.2.14}$$

Y_C is defined such that positive catcher yields can be identified as a net mass increase. Due to the analogue derivation of Y_T and Y_C, equations (2.2.8) and (2.2.13) appear similar. Nevertheless, the constants C_1 and C_2 differ by the parameter A_Q. For an accurate evaluation, it is crucial to have reliable methods for determination of $\Delta f(\Delta t)$ and j_c, which is described in chapter 3.2.
Since the underlying equation (2.1.1) is only valid for spatially homogeneous particle bombardment or deposition, the QCM measurements demand a uniform irradiation over the quartz's total sensitive area [29,31]. While this condition was satisfactorily met for Y_T during experiments via homogeneous ion beam scanning, the angular distribution of the sputtered particles can not be assumed to be homogeneous. Therefore, the value Y_C can rather be

interpreted as a mathematical convolution of the sensitivity function of the quartz and the angular distribution of sputtered atoms integrated over the quartz surface. Additionally, it was assumed that incoming atoms were directly deposited onto the quartz, assessing an ideal sticking probability of 100% during derivation of equation (2.2.13). Studies of silver and gold sticking coefficients supported this assumption, but experimental data regarding tungsten sticking coefficients was not known upon completion of this thesis [33]. Furthermore, reflected ions from the target may hit the catcher quartz and induce secondary sputtering events, resulting in a decrease of the total mass change. More details about the mathematical background of sputter yield determination via the QCM technique can be found in the outlined literature [29–31].

2.3 Numerical Simulation Methods

In chapter 5, experimental results obtained during this project are compared with data originating from numerical simulations. Therefore, background information about the used simulation code *TRI3DYN* is given in this section.
TRI3DYN is a code for dynamic Monte Carlo simulations of ion solid interactions, which also allows consideration of three dimensional features of the target surface [34]. Like it's predecessor *TRIDYN*, which is a code only suitable for simulating flat surfaces, the Binary Collision Approximation (BCA) forms a basis for the calculation of various key parameters like sputter yields, ion ranges, dynamic variation of surface structure or elemental compositions and also allows to determine the flight directions of the sputtered and reflected particles [35]. Especially the latter can be used to reconstruct the catcher yield signal from a QCM measurement, which is of fundamental interest in the course of this thesis.
For the simulation, a three dimensional surface structure needs to get defined initially by usage of a so-called *VOXEL* discretisation. It has to be mentioned, that the maximum size of the computational volume for these simulations was crucially limited due to performance trade-offs. Therefore, surfaces with roughness values higher than 100 nm were hard to implement, as the size of individual surface features became comparable to the lateral size of simulated region of interest. The virtual surfaces originated from a dedicated random surface generator code, based on *PYTHON*. Thus, these virtual surfaces did not directly correspond to any of the measured sample topologies. The *PYTHON* program used a loop of random trials, until a surface which favourable roughness value R_q was generated [36]. Nevertheless, the surface inclination distribution of these surfaces was not considered during the modelling, and might lead to significant differences respective their behaviour under ion bombardment. More information regarding *TRI3DYN* and the simulation of ion-solid interaction can be found in the references [34, 35].
The simulation of various tungsten surfaces was executed by *Reinhard Stadlmayr*, (IAP TU WIEN) who developed a substantial amount of experience with *TRI3DYN* [20].

3 Experimental Methods

This master thesis was carried out with a strong focus on experimental work. Therefore, comprehensive information regarding the application of utilised measurement techniques is given in the following chapter.
As a starting point, the general experimental setup is described in section 3.1, before the technical implementation of the QCM method is shown in section 3.2. Here, special focus is directed on the development of a new catcher QCM apparatus, which was a major part during elaboration of this thesis. In section 3.3, empirical knowledge from the calibration procedure of the catcher QCM is stated, which was of importance in terms of reproducibility of the measurements. At last, a demonstration of the general experimental procedure is described in form of a protocol in section 3.4.

3.1 Overview Experimental Setup

Sputter yield measurements via ion bombardment demand well defined environmental conditions. In order to successfully direct an ion beam onto a target by transmission over several centimetres, low pressure conditions need to be obtained within the experimental chamber. In addition, adsorbates on the target surface like water or also organic molecules as well as oxidation, need to be kept on a minimum. Therefore, the experimental chamber was evacuated down to UHV base pressures of 10^{-9} mbar via turbomolecular pumps, which was controlled with Bayard-Alpert pressure gauges. Figure 3.1 shows a photo of the experimental setup and highlights crucial components. The ion beam was generated via a *Specs IQE 12/38* ion source (figure 3.1 A), which was fed by defined amounts of argon from a *Linde (Ar 5.0) HiQ Minican*, regulated via a pressure controlled *Balzers RVG 050 B* thermovalve (TV). In this type of ion source, the gas atoms were ionised by interaction with free electrons emitted from a thorium coated tungsten filament, before they got accelerated towards the target sample via application of a certain acceleration voltage. The utilisation of argon ions in this case was favourable, since argon is also relevant as seeding gas for fusion reactors (compare section 1.1.2, [14]). A Wienfilter (figure 3.1 B) was utilised as m/q filter, so that only Ar^{1+} ions were forwarded to the target and all other ions and neutral atoms originating from residual gas impurities were filtered out. Deflection plates allowed scanning of the focused ion beam, which was used to irradiate the target sample quasi-homogeneous over a desired surface region and also to determine the mean current density via a Faraday-Cup.

An ion flux of about 1.5×10^{16} ions/(m^2·s) was usually reached during experiments. Sample positioning was obtained via usage of multi-axis manipulators. The manipulator C (figure 3.1) allows linear movement along all three space axes and one rotational degree of freedom along the z-axis. Similar to earlier studies [37], it was used to support both a Faraday-Cup for ion beam current measurements and the target, which was either a quartz crystal during direct sputter yield determination (3.2.1) or a tungsten coated sample during all other measurements. Manipulator D (figure 3.1) offered five degrees of freedom, three main linear movements, one rotation along the y-axis and one additional linear movement into the y - direction. This was a basis for supporting the new catcher QCM hardware, which was used during all of the experiments. A simplified sketch of a top view on the experimental setup is provided in figure 3.2 for comparison. Power supplies and control panels of the setup components were positioned in an industrial rack for electronic devices directly next to the vacuum chamber. Analogue output signals of all sensors were forwarded to a computer for data acquisition via A/D converters. Visual observation of the experimental chamber was obtained by usage of a commercially available webcam and an endoscopic cold-light source.

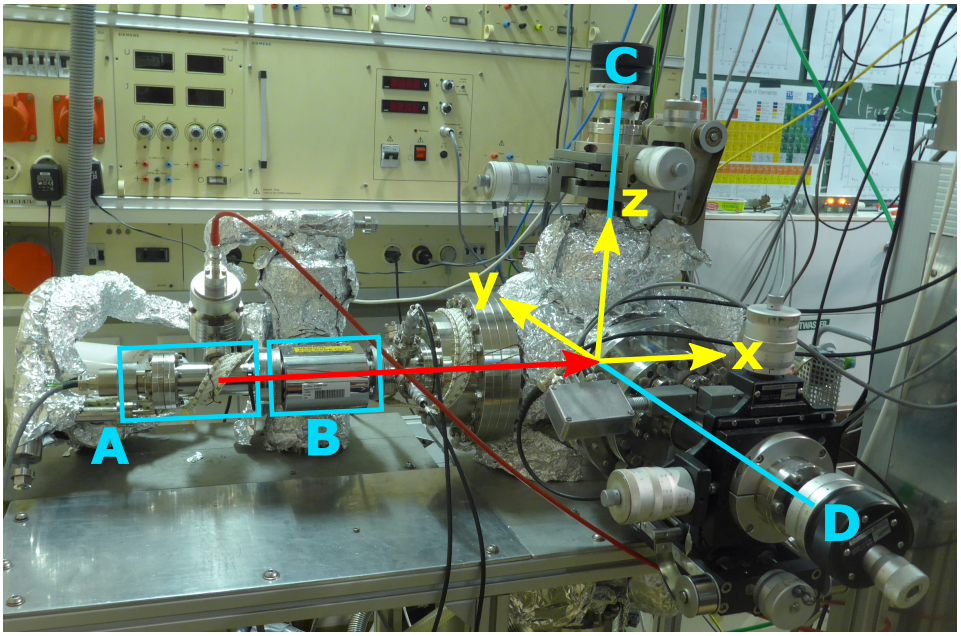

Figure 3.1 – Photo of the experimental setup. The laboratory coordinate system was added in yellow colour with it's origin at the approximate target position. The direction of the argon ion beam is highlighted via a red arrow. Region A and B indicate the *Specs IQE 12/38* ion source and the Wienfilter, respectively. C and D both represent the manipulator stages of target and catcher QCM.

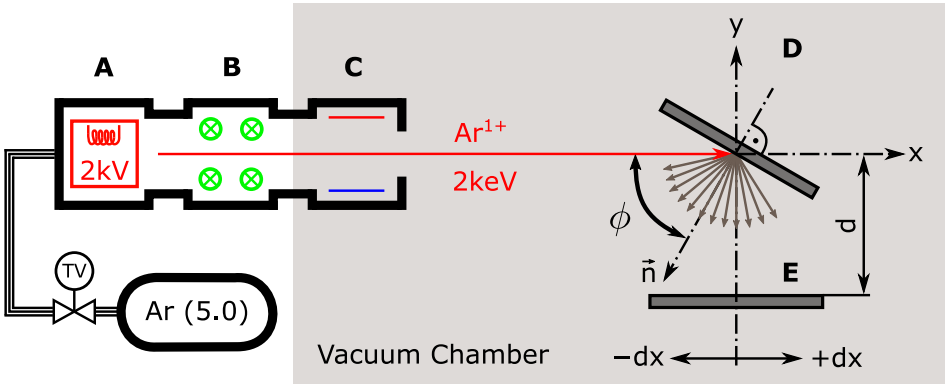

Figure 3.2 – Sketch of the experimental setup. A - Ion source fed with argon from a bottle via pressure controlled thermovalve, B - Wienfilter, C - Deflection plates for beam positioning and scanning, D - target under ion beam bombardment, E - Catcher QCM with distance d towards target center.

3.2 Quartz Crystal Microbalance Experiments

In order to take full advantage of the high QCM sensitivity, it was necessary to have precise measurement methods for the two main parameters $\Delta f(\Delta t)$ and j_c. In chapter 2.2, an equation for the sputter yield Y_T was derived and especially equations (2.2.8) and (2.2.13) highlight the importance of both ion current determination and measurement of the temporal eigenfrequency change of the quartz.
Irrespective to the actual QCM approach (see following subsections), the utilised quartz crystal was always a thin quartz platelet of 13 mm diameter and 0.35 mm thickness. On both sides, a gold electrode with 140 nm thickness was applied as electrical contact. In addition, a layer of desired material needed to be deposited on one side with a thickness of several 100 nm. A photo of a representative quartz for the QCM is shown in figure 3.3. If such a platelet is driven by an alternating current which fits to it's eigenfrequency f_Q, the quartz impedance Z becomes minimal. This effect can be utilised to regulate the driving frequency, which was successfully achieved via the QCM electronics and enables direct determination of the frequency change over time during target or catcher QCM experiments. The driving AC voltage was provided via a *Tektronix AFG3022 C* function generator, which was regulated by a virtual PID controller executed on the computer for impedance minimisation . A *LabVIEW* program was used to log the frequency change over time for further data evaluation.
The ion beam current density j_c was quantified via measurements with a Faraday-Cup, which was also mounted on the target manipulator stage. This apparatus consisted of an aperture with 0.97 mm^2 areal size and a metal cup behind it, which was grounded via a *KEITHLEY 6485* picoamperemeter. It enabled to measure the total current of ions coming inside the pinhole, while electrons originating from secondary processes were repelled by application of a suppressor voltage. In order to get the ion beam current density, a cross profile measure-

ment of Faraday-Cup currents along the y and z-direction with increments of 1 mm was obtained. The range of measurement interval is usually about the size of ion beam scanning. By calculating the mean and standard deviation of the values and further division by the area of the Faraday-Cup aperture, a quantification of the ion beam current density j_C and also an error estimation for this quantity was achievable. It has to be mentioned, that the projected current density changes for ion beams impinging with a different angle than zero respective to the surface normal of the target. This can be compensated via multiplication with the value of $cos(\phi)$. The ion beam cross profile measurement was executed right before and after the sputter yield experiments in order to quantify variations of the beam profile that occurred in the meantime. Even though the ion beam current density normally changed less than 5% respective the initial value, this led to a major contribution to the final sputter yield error. More details regarding evaluation of a sputter yield from the measured quantities are available in section 3.4.
In the following subsections, two different approaches for QCM measurements are highlighted.

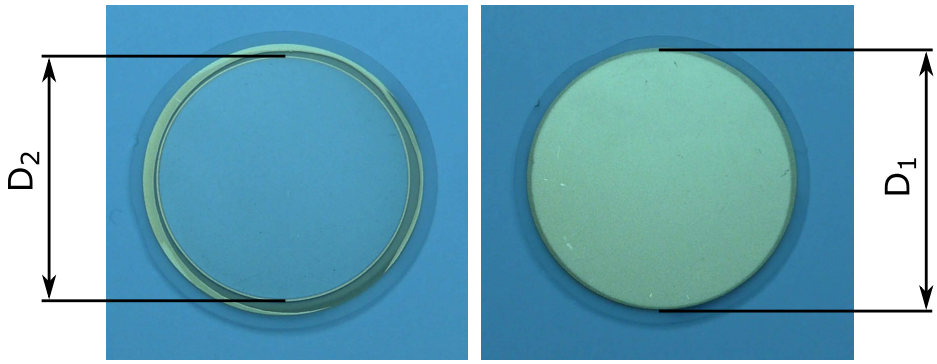

Figure 3.3 – Photos of front- and backside of a coated quartz crystal utilised for the QCM measurements. D_1 - Diameter of gold electrode, D_2 - Diameter of coating.

3.2.1 Target QCM Approach

In the target QCM approach, only the measurement of primary target sputter yield Y_T was of interest. Here, it was essential to use a quartz with the coating of desired material as a target for exposition to the ion beam. During bombardment, this coating decreased in thickness, which lead to an increase of the quartz resonance frequency f_Q. Via the general method for determination of $\Delta f(\Delta t)$ and j_c explained in chapter 2.2 and utilisation of the equation (2.2.8), the target sputter yield Y_T was calculated. It has to be mentioned, that this approach did not provide any information about the angular distribution of the off-sputtered target atoms, but only regarding the net-sputter yield. A sketch of the target QCM under ion bombardment is provided in figure 3.4.
The target QCM approach was the most common measurement procedure executed with the experimental setup shown in figure 3.1. It was used to determine Y_T as a function of total

fluence, incident angle or kinetic ion energy for various materials of interest, like it has been done in earlier studies [19,28,37]. In the course of this thesis, the target QCM approach was only used during measurements with a reference sample, which was a quartz crystal coated with a tungsten layer of certain roughness.

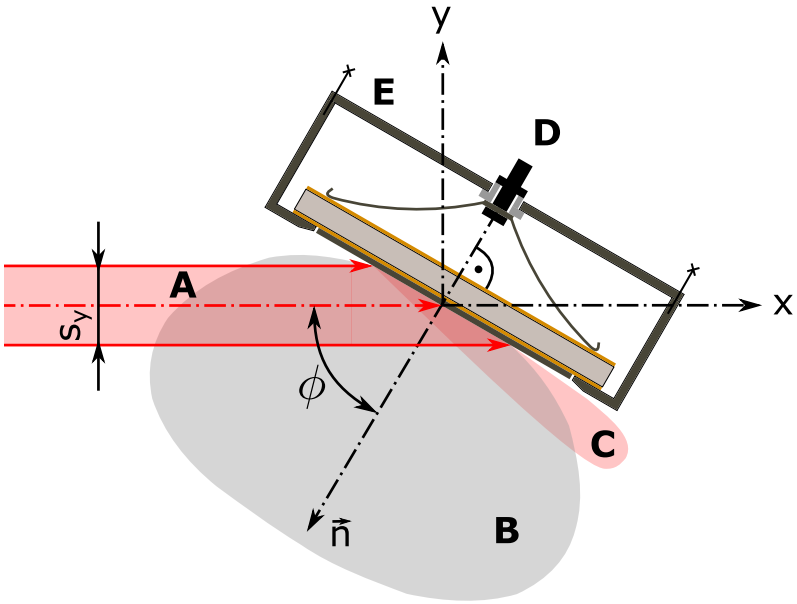

Figure 3.4 – Sketch Target QCM approach. A - Argon ion beam under incident angle ϕ with projected scanning width s_y, B - Angular distribution of sputtered atoms, C - Angular distribution of reflected ions, D - Spring construction for both mechanical support and electrical contact to quartz, E - Chassis for mechanical support of quartz.

3.2.2 Catcher QCM Approach

As mentioned in the previous section, the target QCM approach did not provide any information about the angular distribution of sputtered target atoms, but only gave a value for the target sputter yield Y_T. Another intrinsic limitation of this measurement approach was the necessity of a quartz crystal as a target. In order to circumvent these limitations, a new apparatus for the studies undertaken in the course of this thesis was developed. In principle, again the QCM technique was utilised, in combination with a tilt mechanism and a manipulator with five degrees of freedom. This new setup is called "catcher" QCM, since it is used to "catch" sputtered atoms from a target by redeposition. An advantage was, that the target could be any piece of sheet material without limitation to a thin film. A rendered picture of the new design, obtained via the CAD software *SolidWorks*, is shown in figure 3.5. The manipulator axis consisted of two movable, axially symmetric shafts: a wider one which acted as mechanical support for the catcher hardware via the lever construction A (figure 3.5) and also a thinner one, which could be moved in y-direction independently. The movement

of this thinner shaft was transformed into a well defined tilt rotation of the catcher quartz holder C by acting on the movable lever construction B (see 3.5). All necessary steel parts of the developed design were manufactured at the in-house workshop of the IAP, TU WIEN. Corresponding technical drawings are available in the appendix of this document.
With the new hardware, the catcher quartz crystal could be moved and oriented in a desired position respective the sample. Therefore, straight lines along but also circular tracks around the target could be followed during positioning. The latter constituted an incremental innovation in respect to former catcher QCM designs developed at the IAP, TU WIEN [31, 38]. Especially for the circular track positioning, the absolute distance between the target and catcher quartz centre remained constant and much less influences on the signal by geometrical offsets were expected. In addition, the surface was always oriented perpendicular to the centre of the target, which eliminates signal decreases induced by projection effects. A simplified sketch of the catcher QCM approach is provided via figure 3.6.
In order to circumvent additional effects originating from different coating compositions, also the catcher quartz was equipped with a tungsten layer. Therefore, a sticking probability of 100% was expected for the incoming tungsten atoms (compare chapter 2.2). Since these deposited atoms led to an increase in thickness and therefore to a decrease of resonance frequency f_Q of the quartz, a calculation of the catcher yield Y_C via equation (2.2.13) derived in chapter 2.2 was feasible. Here, only the total ion beam current I_c irrespective to any projection effects on the target was of interest. Thus, the value of $cos(\phi)$ must not be considered.
The measured values of Y_C at certain catcher positions did not directly correspond to the angular distribution of sputtered particles from the target. A variety of ion impact positions on the target contributed to the total angular distribution of sputtered atoms due to ion beam scanning. Since the catcher quartz diameter was furthermore about the same size as the distance between sample and catcher quartz, the signal obtained via this experimental approach rather gave a value for the convolution of total angular distribution of sputtered target atoms and the sensitivity function of the catcher quartz. In addition, reflected ions may significantly contributed via secondary sputtering of the catcher quartz to the net signal. More theoretical insights regarding the catcher yield Y_C can be found in reference [31] and the theory chapter 2.

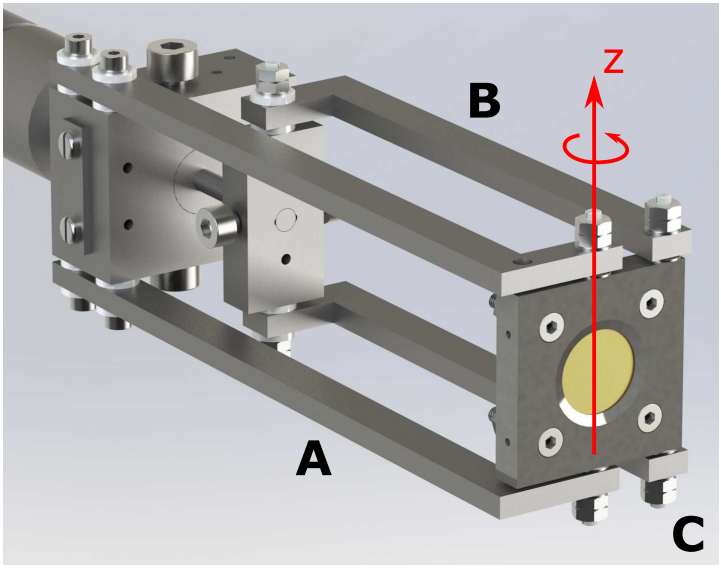

Figure 3.5 – CAD rendered picture of Catcher-QCM. A - Stationary lever construction, B - Movable lever construction, C - Catcher quartz front (can be tilted around z-axis).

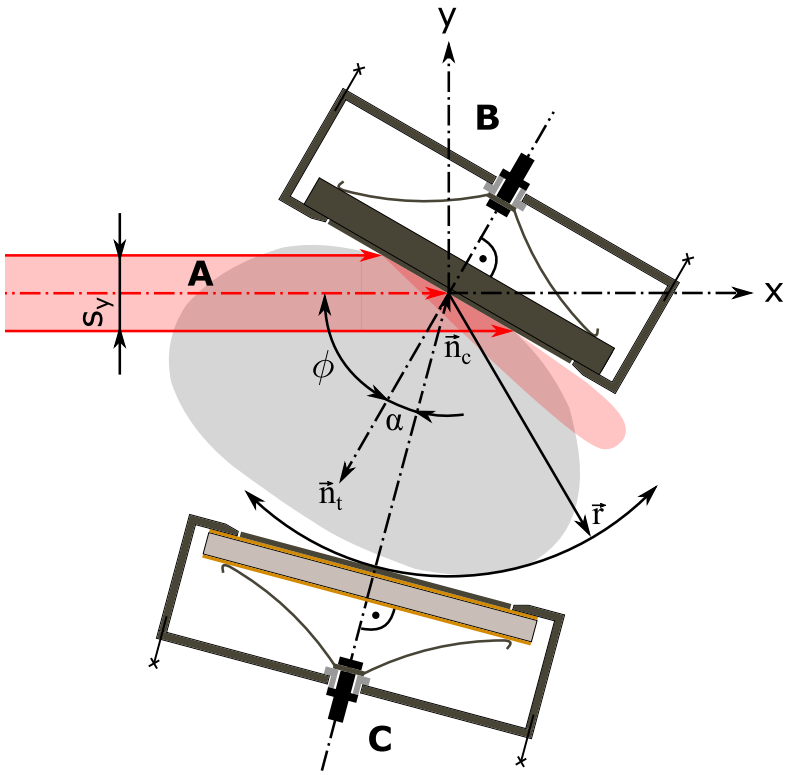

Figure 3.6 – Sketch of the Catcher QCM approach, shown for circular track positioning. A - Argon ion beam under incident angle ϕ with projected scanning width s_y, B - Target QCM or tungsten coated sample, C - Catcher QCM, α - Angle between both surface normal directions of target and catcher quartz, repsectively. $\vec{r}$ is the radius of the catcher track.

3.3 Calibration Procedure

This section provides important comments regarding the calibration of both target and catcher QCM apparatus, which was a crucial phase during the experimental part of this thesis. The QCM technique is generally a sensitive measurement method. Therefore, influences of side-effects may need to be considered if they contribute significantly during the experiments. Compared to values of sputter yield Y_T measured via the target QCM approach, the catcher yield values Y_C appeared to be about two orders of magnitude lower. This corresponded to much smaller frequency changes in the range of about 0.1 mHz/min during tungsten deposition on the catcher quartz, compared to Hz/min for direct ion impact erosion (depending on incident ion energy and flux) .
The quartz crystal's resonance frequency f_Q does not only depend on it's thickness d_Q (compare chapter 2.2), but is also sensitive to a variety of other environmental parameters. Dependencies of f_Q are known for the quartz temperature [39]. In addition, the power supplies and electronic circuits providing the alternating current for the resonant quartz drive are also sensitive to temperature variations. Further, mechanical stresses on the cables induced by positioning of the QCM can lead to substantial influences on the resonant frequency, as the cables also contribute via their capacity to the whole electric circuit characteristics. All of these effects needed to be taken into account for measurements. During initial calibration of the catcher QCM apparatus, a protocol for the experiments was developed to ensure reproducibility of the results.
In addition, also geometrical alignment of the crucial components like ion source, target QCM and catcher QCM was validated to provide well defined experimental conditions. Furthermore, the catcher QCM hardware was tested prior implementation to the vacuum chamber in order to verify the precision of the tilt mechanism. As described in section 3.2.2, the linear movement of a manipulator shaft is transformed to a rotation of the catcher QCM front along the vertical z-axis via a lever mechanism. This transformation can be analytically formulated via basic goniometric calculations, which represents an idealistic description of this construction. Since geometrical errors of the individual hardware parts had to be expected within technical tolerances of manufacturing, a test of the tilt mechanism was done to determine error estimations for positioning. An optical experiment was executed, using a commercial positioning laser for creation of a well defined optical light beam and a metal platelet with a mirror-like finish as a reflector mounted in the catcher QCM hardware. Laser and catcher QCM were located at defined positions in a horizontal plane with a certain distance and angle γ to each other (see figure 3.7). Label marks on a long wall were placed at analytically calculated positions. The linear position of the manipulator was adjusted such that the mirror in the QCM front was tilted by the angle β, resulting in a reflected beam pointing to the corresponding label marks accurately. The nonius scale values of the manipulator were compared to the ones calculated analytically. Via linear error propagation, a determination of the angular positioning error was feasible, which is shown in table 3.1 for all measured angles β. The procedure was repeated several times for each angle to check influences by bearing gaps. Calculations led to the result, that the maximum error $\Delta\beta_{max}$ determined for any of the measured angles was 1.71°. Projection effects due to tilt angle errors can be assumed

to scale via $\sim \big(1 - cos(\Delta\beta)\big)$, which would result in an estimated projection error of only $\pm 0.04\%$.
Via fixations of the bearing gap at the tilt axis, further improvements were obtained such that the errors between analytical and empirical values were low enough to be neglected. Thus, the analytical values for positioning were used for the catcher QCM experimental procedure, which can be found in the appendix of this thesis.

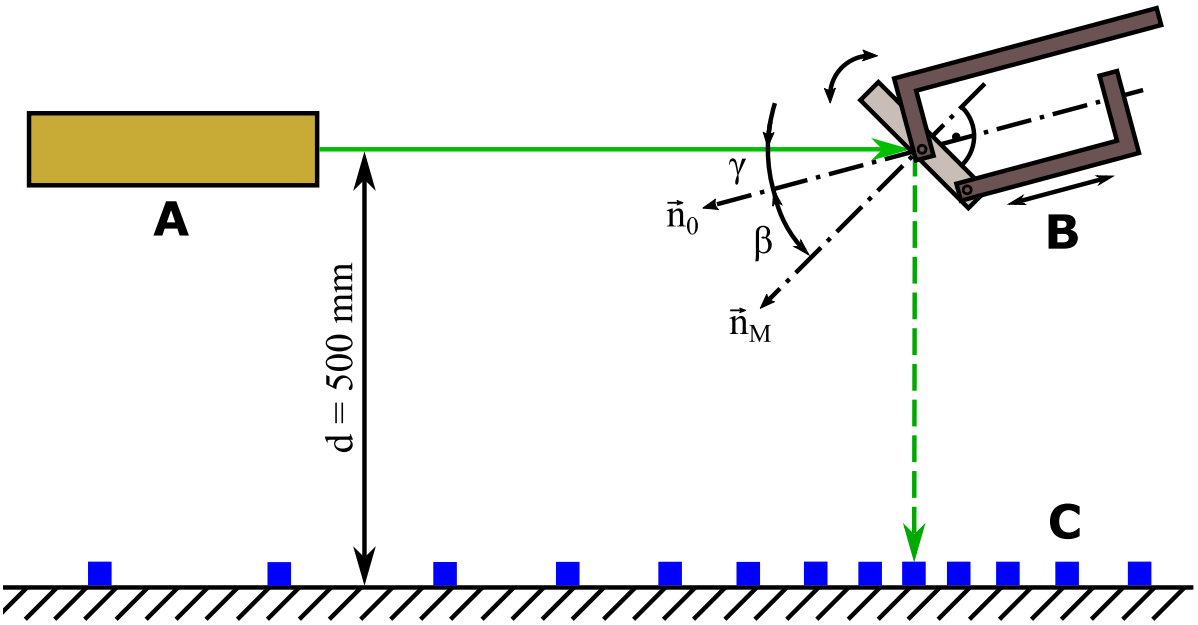

Figure 3.7 – Top-view Sketch Catcher QCM positioning test. A - Laser providing optical beam towards catcher QCM - B which is mounted with a mirror metal platelet. C - Wall with defined labels corresponding to analytical positions. β - Tilt angle of catcher QCM front, γ - Initial angle between beam and mirror surface normal for $\beta = 0°$, d - Distance between wall and optical axis.

β	-10°	-5°	0°	5°	10°	15°	20°	25°	30°	35°	40°	45°
$\Delta\beta$	1.6°	1.7°	1.7°	1.5°	1.6°	1.2°	0.9°	1.0°	0.9°	0.9°	0.9°	0.9°

Table 3.1 – Table with the results of an error evaluation test for the tilt mechanism of the catcher hardware. The individual angles β were checked in terms of reproducible positioning via the linear nonius scale. Further improvements were obtained via fixation of the bearing gap at the tilt axis of the construction.

3.4 General Data Acquisition and Evaluation Process

This section offers a detailed overview on the experimental protocol which was developed in the course of this thesis, in order to provide a basis for future studies with this setup. At first, the preparation procedure is described, followed by the experimental protocol for data acquisition. Finally, some comments regarding the data evaluation are completing this section.

3.4.1 Measurement Preparation Procedure

In the initial phase of each experiment, a desired target needed to be mounted in the corresponding target holder. Depending on the actual experimental intention, this was either a tungsten coated quartz for direct determination of target sputter yield values (compare 3.2.1), or other tungsten coated sample platelets. The chamber necessarily needed to be opened for mounting the target, leading to exposition of the inner walls and devices towards atmosphere. This is not favourable in terms of contamination with oxygen, water and carbohydrates, which influence the residual gas properties during the experiments. Therefore, the chamber was flooded prior opening with dry N_2 gas to reduce water contaminations, while the actual time with open chamber lid was kept to a minimum. When the mounting of target holder onto the corresponding manipulator was successful, the chamber was closed and evacuated to UHV pressure. Additionally, a heating system raised the chamber temperature higher than 100 °C for at least 24 hours to support desorption of water and carbohydrates from the inner surfaces, which is called "baking" of the vacuum chamber. To prevent temperature induced damages, all sensitive components like pressure gauge magnets, BNC cables, peripheral QCM electronics and also the Wienfilter magnet were removed. After the baking procedure was finished and room temperature was reached, the obtained base pressure in the chamber settled around 10^{-9} mbar. All components were again attached to the chamber and peripheral electronic devices were switched on, such that initial thermal drifts declined well before the experiment starts. Via activation of the thermovalve set-point setting, the ion source was flooded with argon gas at a constant local pressure of 7.7×10^{-5} mbar, which also led to an increase of the chamber pressure to 2.2×10^{-8} mbar. Once the pressures settled, the suppressor for the Faraday-Cup, the ion source and the Wienfilter were activated. By that, a electrical current through the ion source filament was applied, leading to local temperature increase and further desorption of adsorbated contaminations. After sufficient idle time of about half an hour, desired ion source settings like 2 kV accelerator voltage and geometrical parameters were tuned before the source was switched into operating mode. Now, the *PYTHON* code for the QCM frequency control was initialised on the computer, where a digital PID controller is implemented. Depending on the actual utilisation of either target, catcher or both QCM's, the corresponding frequencies delivered from the function generator got controlled such that they fitted to the respective resonance frequencies f_Q of the quartz crystals (compare section 3.2). Generally, two main *EXCEL* documents

were created per experiment, where crucial information regarding both experimental setup and the measurement procedure was logged.

3.4.2 Experimental Protocol

Once the preparation procedure was finished successful, the actual execution of the experiment was done. In order to obtain reproducible data, a general protocol was elaborated in the course of this thesis, which is described hereinafter:

1. **Ion Source optimisation:** As a start, the Faraday-Cup with active suppressor voltage was used to maximise the total ion beam current at the exact centre position of the setup. This was achieved by fine tuning of the ion source parameters on it's control panel, which were further logged into the experimental setup *EXCEL* document. The beam scanning with a desired range was activated afterwards. A table with prominent settings is added to the appendix of this document.

2. **Target Cleaning:** As mentioned in section 3.3, adsorbates were expected also on the target surface. In order to clean it, the ion beam was scanned 7 x 7 mm across the target surface, which was oriented to the ion beam without inclination angle. If a quartz target was utilised for the experiment, the software *LabVIEW* could be used to track the target frequency f_Q during bombardment. Since the sputter yield for adsorbates is much higher than for tungsten, it was assumed to have a clean surface once the signal slope and therefore $\Delta f(\Delta t)$ decreased significantly and remained constant. The total cleaning time was about five minutes. Since a direct signal feedback is only possible for quartz targets, the other samples were also cleaned for five minutes on the basis of this experience.

3. **Catcher Cleaning:** Similar to the target cleaning procedure, the quartz of the catcher system was cleaned as well. This opportunity forms another key advantage of the new developed hardware, since direct ion cleaning was not possible for earlier catcher designs at the *IAP, TU WIEN*. A frequency feedback was always available during catcher cleaning, since the corresponding quartz was never changed for any of the experiments.

4. **Ion beam Cross Profie 1:** To provide well defined bombardment conditions on the target, the Faraday-Cup was used to measure ion current "cross" profiles of the scanned beam at the central position of the chamber. The incident ion impact angle ϕ for all of the experiments executed during this project was 60°. In order to project a quadratic profile on the tilted target, a scanning of 2.5 x 5 mm was chosen. The beam profile was measured both in vertical and horizontal direction, which provided data for the ion current density calculation. Profile values were recorded in the experimental setup *EXCEL* document.

5. **Pre-Coating of the Catcher Quartz:** The catcher quartz was coated prior to the actual start of the experiment for about half an hour at the initial position of the positioning track to ensure optimal catcher surface conditions. Via this, a good reproducibility was obtained.

6. **Execution of the Sputter Measurements:** In general, two different experimental procedures were executed in the course of this thesis. They differed in terms of the followed positioning tracks of the catcher QCM apparatus (compare figure 5.1 in chapter 5) and also in terms of the drift compensation approach. Therefore, the following step was chosen by consideration of the actual experimental approach. Generally, the frequency values were both recorded and visualised with a dedicated program executed via *LabVIEW*.

   For the *Linear Track* experimental approach, the catcher quartz orientation remained parallel towards the laboratory y-axis (compare figure 3.1 in section 3.1). In respect to the catcher QCM zero position in x-direction, a distance of 13 mm between the target and catcher quartz was kept constant. The profile was measured between dx = -5 and 5 mm, following a discretisation of one millimetre. Initially, the frequency drift of the catcher quartz (or also target quartz, if available) was measured for 200 seconds, before the ion bombardment was started. After another 200 seconds of irradiation, the catcher QCM was moved to the next position. In total, the whole positioning interval was measured back and forth during each experiment to validate reproducibility. Frequency drifts with deactivated ion beam were recorded every five measurement points, which was sufficient since the catcher QCM was not tilted during the linear track profile. The start and end time of each experimental phase was recorded in the dedicated measurement procedure *EXCEL* document.

   In contrast to the *Linear Track* profile approach, also a *Circular Track* around the target centre could be obtained with the catcher QCM. The absolute distance between both target and catcher quartz centre was kept constant at 21.4 mm. Via the tilt mechanism and the linear degrees of freedom by the catcher QCM manipulator, an angular interval between -15° and 37.5° respective the target surface normal was obtained with a general discretisation of 5° (except of the last step, where a shift of 2.5° led to the final angle 37.5°). Since the tilt mechanism strongly influenced the frequency signal, the *Circular Track* measurements demanded significant amounts of idle time during the measurement. Similar to the linear profile measurement, the frequency drift was measured for 60 seconds before and also after each measurement step for compensation. After the posteriori drift measurement, the catcher quartz was moved to the next position, resulting in a frequency jump (compare section 3.3). After the drift declined to linear tendencies with acceptable low values, the next measurement step was undertaken. This procedure resulted in a total experimental duration of more than three hours. A fundamental error originating from ion source instabilities can be estimated for such long operation times (see next step). Therefore, only some points of the angular interval were measured twice to check the reproducibility.

7. **Ion beam Coss Profile 2:** To check if the ion source was working sufficiently reliable during the experiment, a second current "cross" profile was measured with the Faraday Cup. By comparison to the values obtained from the first cross profile, temporal variations of the ion beam current can get determined (more details at next page).

8. **Data storage and Setup Shutdown:** To finish the experiment, all the data was saved on the computer and a backup drive, before peripheral electronic devices, the ion source and the computer were shut down. Finally, the argon gas supply was closed and the chamber pressure values decreased to base levels of 10^{-9} mbar.

3.4.3 Data Evaluation

The evaluation of sputter or catcher yields requires knowledge of both $\Delta f(\Delta t)$ and j_c from the experiment, as described in chapter 2.2. The latter was obtained via comparison of both ion beam cross profile measurements. In the *EXCEL* document regarding experimental setup information, a procedure for the determination of j_c and it's absolute error was included, which delivered both a mean value and standard deviation for sputter yield calculations. The determination of $\Delta f(\Delta t)$ was achieved via usage of a dedicated evaluation programme developed in the course of earlier studies by *Reinhard Stadlmayr* on the basis of *PYTHON*. Here, the accurate start and end time points, which were recorded in the experimental procedure *EXCEL* file, were used to determine the frequency slopes for each measurement position, respectively. By consideration of the ion current density j_c, a sputter yield value and corresponding absolute error for the sputter yield was calculated. It has to be noted, that the deviations in both ion beam profile and temporal ion current variations contributed significantly to the total error of the determined sputter yield [37].
This procedure was similar for a catcher yield determination. Here, also the ion beam scanning area and the incident angle of the ion bombardment on the target needed to be included (compare section 3.2.2). To exclude the frequency drifts originating from the catcher tilt mechanism, artificial sputter and catcher yields were calculated via the respective $\Delta f(\Delta t)$ measured slopes. The obtained values before and after the corresponding measurement step were averaged and subtracted from the experimental value, providing a good reproducibility. The resulting numerical values from data evaluation were saved as text files and provided the basis for further data analysis and visualisation procedures developed via *PYTHON*.
The sputter yield determination was mostly executed on the basis of procedures already elaborated for earlier studies. Therefore, more fundamental insights into sputter yield, catcher yield and the error calculation can be found in the outlined references [31, 37].

4 Target Sample Characterisation

In this chapter, a characterisation of the used samples is provided. At first their individual origin is outlined, before detailed results of investigations regarding roughness and local surface inclination angles are provided. Finally, experimental results concerning the elemental composition of the target samples are shown.
In total, five different samples were chosen as targets for subsequent ion bombardment. Initially, measurements on a quartz crystal coated with a thin layer of tungsten were providing values not only for the catcher yield Y_C, but also for the target sputter yield Y_T. These measurements were primarily executed to have an experimental reference, to which all the other results were compared in the course of this thesis.
The samples of main interest were tungsten coated silicon wafer platelets with varying R_q roughness values ranging from nanometres up to micrometres. Here, only the catcher QCM approach was followed, since no direct determination of the sputter yield can be obtained for such samples. Nevertheless, quantitative calculations regarding Y_T were feasible by comparison of the angular distributed catcher yield tendencies in respect to the reference sample. In total, four different samples of this kind were investigated, which are labelled via the name *19WSi-xx* (the last two indices xx indicate production batch and specimen, respectively).
To provide a better overview, the samples are shortly characterised in table 4.1:

Label	**Details**
18W4	W coated quartz crystal, Direct Y_T and Y_C profile measured as reference
19WSi-1a	Si coated by W, deposition time 80 min, only Y_C profile
19WSi-2b	Si coated by W, deposition time 40 min, only Y_C profile
19WSi-3a	Si coated by W, deposition time 1 min, blisters found, only Y_C profile
19WSi-3b	Same as *19WSi-3a*, but no blisters observed, only Y_C profile

Table 4.1 – Table with general sample description.

4.1 Origin of the Samples

18W4 Reference Sample

The reference sample *18W4* consisted of a quartz crystal coated with a tungsten layer, which was a commonly utilised target system for sputter yield measurements at the Institute for Applied Physics, TU WIEN (IAP). The virgin quartz disk (*KVG Quartz Crystal Technology Model XA3641*) was a stress compensated (SC-cut) crystal and equipped with two gold electrodes of 140 nm thickness to provide electrical contact [40]. The eigenfrequency f_Q of this quartz was exactly 6.0×10^6 Hz.
The tungsten layer on one side of the quartz was obtained by magnetron sputter deposition in the course of a collaboration with the Max-Planck Institute for Plasma Physics, Garching (IPP Garching), *Germany*. The tungsten layer thickness was about 500 nm, which was validated via Rutherford Backscattering Spectroscopy (RBS) measurements.

19WSi Samples

The main target samples *19WSi-xx* originated from a collaboration with the Forschungszentrum Jülich (FZJ) research facility in *Germany*. As initial step, several silicon wafer platelets with a thickness of about 1 mm were cut at the IAP TU WIEN, and mounted on three different sample holders for transportation. Each of these sample holders carried two platelets with a size of 10 x 10 mm and one with 10 x 5 mm, respectively. All sample holders were sent to the FZJ and coated with a layer of tungsten via Chemical Vapour Deposition (CVD). Different deposition times were chosen for each sample holder, such that a variation in tungsten layer thickness and also roughness was achieved. For samples mounted on the same holder, the exposition parameters were therefore the same. Thus, a batch of three similar samples per tungsten deposition parameter was obtained. For the declaration, *19WSi-1x* can be identified with the longest deposition time and also highest roughness. *19WSi-2x* and *19WSi-3x* correspond to gradually lower deposition times. The second index describes the individual specimen of a certain batch. Here, *a* and *b* indicate 10 x 10 mm samples, while *c* denotes a smaller 10 x 5 mm platelet. A photo of the samples after CVD can be seen in figure 4.1. Unfortunately, the sample *19WSi-1c* was destroyed during the tungsten coating process. A reason for that could be thermal induced stresses or too strong clamping forces of the sample holder. In addition, also the samples *19WSi-1a* and *19WSi-1b* did show some crack formation. After transportation back to the *TU VIENNA*, *19WSi-1b* was even more damaged, but still big enough to use it for determinations regarding elemental composition (more details in section 4.4). An interesting observation was made for batch *19WSi-3*, which appeared to be covered with blisters except specimen *19WSi-3b*. Literature investigations and consultation of the research partners did not yet lead to satisfying explanations regarding

the origin of those blisters. The tungsten deposition was executed by *Leonard Raumann*, FZ Jülich (*Germany*).

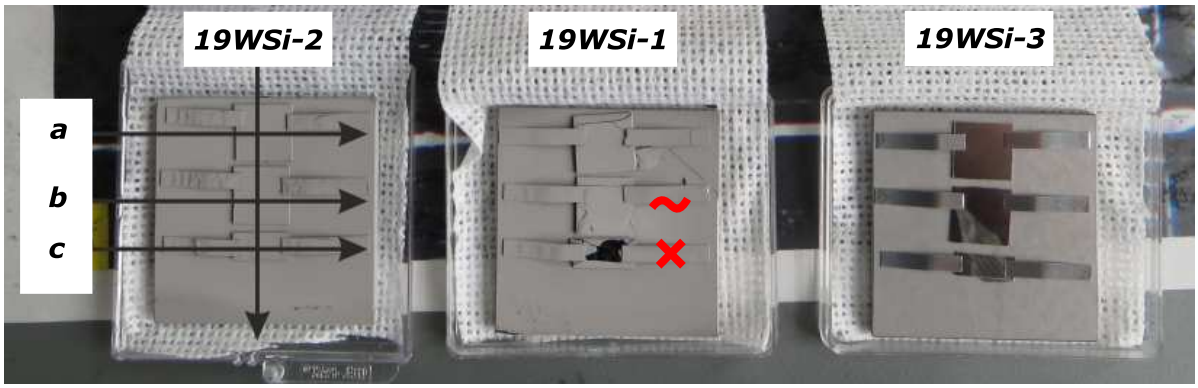

Figure 4.1 – Photo of samples after CVD at *FZ Jülich*. Batch *19WSi-1* had the thickest W layer and highest R_q values. Unfortunately, specimen 2 and 3 were damaged or destroyed during CVD or transportation, respectively. Batch *19WSi-2* had intermediate W layer thickness and R_q values. Batch *19WSi-3* had the thinnest W layer and lowest R_q values.

4.2 Roughness Determination

In this section, results from initial investigations regarding surface roughness of the samples are provided. It was of high importance during the elaboration of this thesis to obtain detailed insights regarding the sample surface topology, since this was an intended variable parameter over the whole set of samples. One approach for a quantitative analysis of surface topologies was a determination of the roughness value R_q. It describes the mean quadratic offset of individually measured heights z_i from the mean line z_m over a certain region of interest, also known as Root Mean Square (RMS) value. The mathematical formulation of this quantity in a single dimension is given via equation (4.2.1):

$$R_q = \sqrt{\frac{1}{n}\sum_{i=1}^{n}(z_i - z_m)^2} \tag{4.2.1}$$

In equation (4.2.1) the parameter n corresponds to the number of measured height positions in total. The R_q value can also be calculated for a two dimensional surface via consideration of another sum along the other space axis. To experimentally determine R_q values for the samples utilised during this project, both Atomic Force Microscopy (AFM) and Con-Focal Microscopy (CFM) were used for investigation. After showing the visual results of both techniques, a table is summarising the final quantitative results. Especially for the smoother specimens, the AFM was expected to be more reliable for determinations of roughness values than CFM, which was rather used for characterisation of the rougher samples.

4.2.1 AFM Measurements

AFM is a powerful tool to investigate surface topologies on the nanoscale. In the course of this thesis, an *Asylum Research Cypher S* device was used for measurements on the experimental samples. This technique is based on the rasterisation of a very precise silicon cantilever over a desired surface region of interest, while a laser beam is reflected via the cantilever backside towards a CCD camera. If the surface topology varies at a certain position, the cantilever tip is moving vertically, leading to a magnified change of the laser projection point at the CCD camera. Via this principle, two-dimensional height profiles of surface regions up to a size of 30 x 30 μm^2 were obtained. For more information regarding the AFM technique, please compare reference [41]. By usage of the open-source software *Gwyddion*, the raw data was further analysed to determine the roughness value R_q [42].

At first, results were obtained for the reference sample *18W4*, which revealed a scaly surface structure (see figure 4.2). Individual peaks ranged up to a height of 900 nm, while a comparable flat topography was found in between. Since the size of individual surface features was already on the same size as the region of interest size, the results obtained for the R_q value based on the AFM method were not assumed to be representative, but the picture is shown for completeness. Nevertheless, the investigation was used to obtain information regarding the surface inclination angle distribution (see section 4.3).
Representative visual AFM results are also shown for the samples *19WSi-1a to 19WSi-3b* (figures 4.3 - 4.6) One can clearly see, how the scale of roughness changed for the individual sample batches.
In figure 4.3, a coarse pyramidal structure with height peak values in the order of 5 μm is visible. For the highest peak, the technical limit of the AFM was exceeded, resulting in a black artefact. Even though the maximum size 30 x 30 μm^2 was chosen for the region of interest, the biggest surface features were still on the same order of size. A calculation of R_q value was possible, but not assumed to be representative for the whole surface. In general, a more reliable determination of R_q values for this batch was expected from the CFM technique.
The same holds for the batch *19WSi-2*, where similar surface topologies were observed (compare figure 4.4). Even though the technical limit was not reached, the height of these structures was assumed to be too macroscopic to achieve quantitative information based on the AFM technique. Nevertheless, a distinct decrease in feature size can be recognised in contrast to the observations for batch *19WSi-1*. By consideration of a different image scale, the pyramidal features decreased in size approximately by a factor of 5.
The results for *19WSi-3* show an ambivalent behaviour within different specimens of the same batch. In general, the surface topology was much smoother with feature sizes at the nanoscale, which made the AFM method well suitable for quantitative analysis. It was interesting to see, that the pyramidal structures from the other sample batches were not observed at all. For the samples *19WSi-3a* and *19WSi-3c*, a smooth surface covered with characteristic blisters was found (compare 4.5). These blisters varied in diameter between 1 - 5 μm and covered the whole sample surface. For the sample *19WSi-3b*, no blisters were found (see

figure 4.6). The R_q values between blister-free spots of sample *19WSi-3a* and the general value for *19WSi-3b* appeared to be identical, leading to the assumption that those blisters can be seen as a local elevation of a substantial part of the tungsten layer.

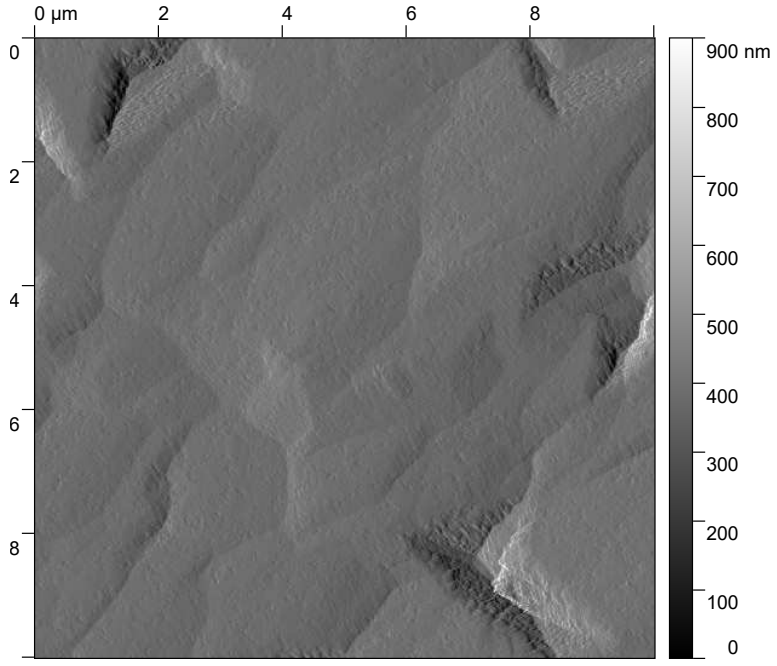

Figure 4.2 – 10 x 10 μm^2 AFM picture of sample *18W4*. The surface shows a scaly topography, with individual peaks ranging up to 900 nm. In between, the topography appears rather smooth. Some features were comparable in size to the picture itself, therefore no R_q values were considered from this specific investigative method.

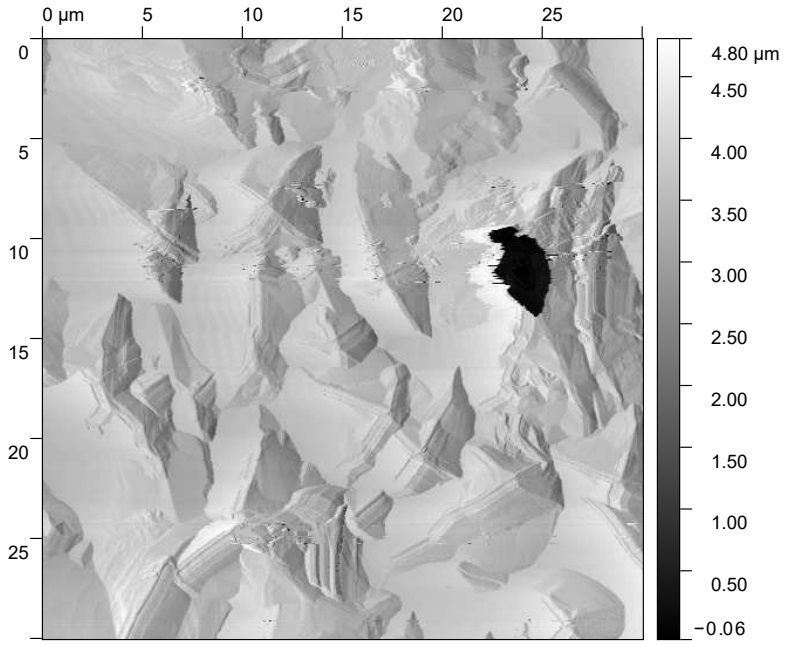

Figure 4.3 – 30 x 30 μm^2 AFM picture for sample *19WSi-1a*. This measurement was on the edge of feasibility, as the cantilever tip reached technical limits (black spot). Measurement was done with the maximum size possible, to encounter the surface feature size. Obtained R_q results were not assumed to be representative for this case.

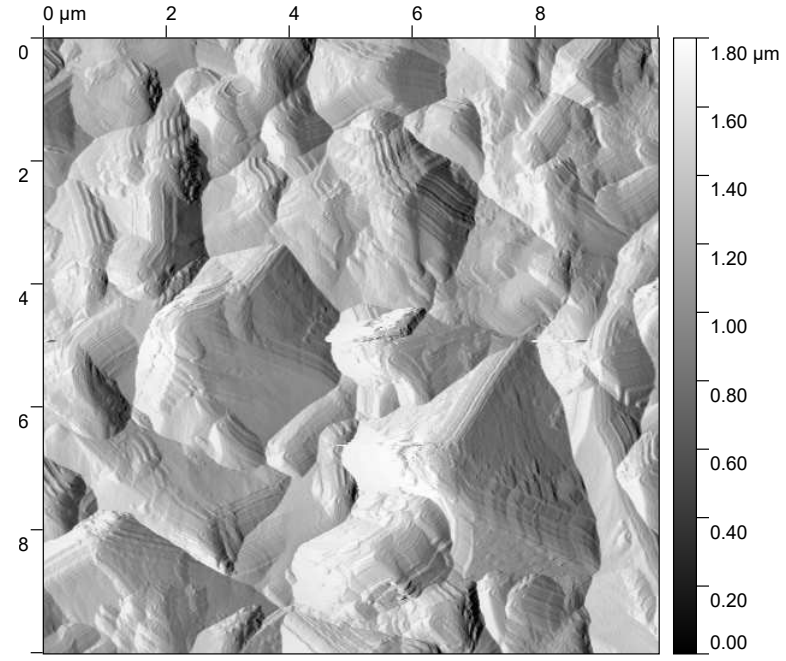

Figure 4.4 – 10 x 10 μm^2 AFM picture for sample *19WSi-2b*. Some surface features were on the edge of AFM technical limits. Obtained R_q results were therefore not assumed to be representative in this case.

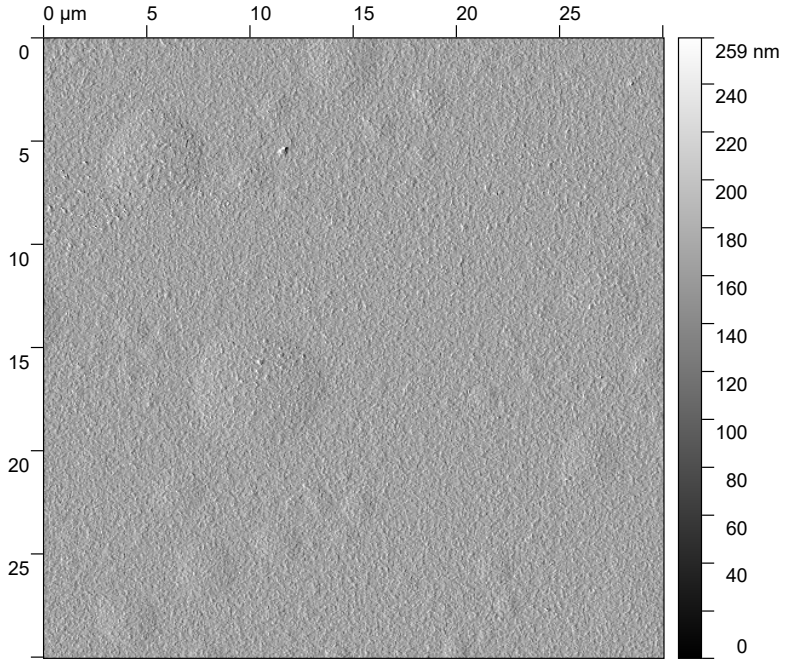

Figure 4.5 – 30 x 30 μm^2 AFM picture for sample *19WSi-3a*. This measurement was taken with the maximum size possible to consider many of the observed blisters. Mean result $R_q = 29$ nm of this sample was considered for this project.

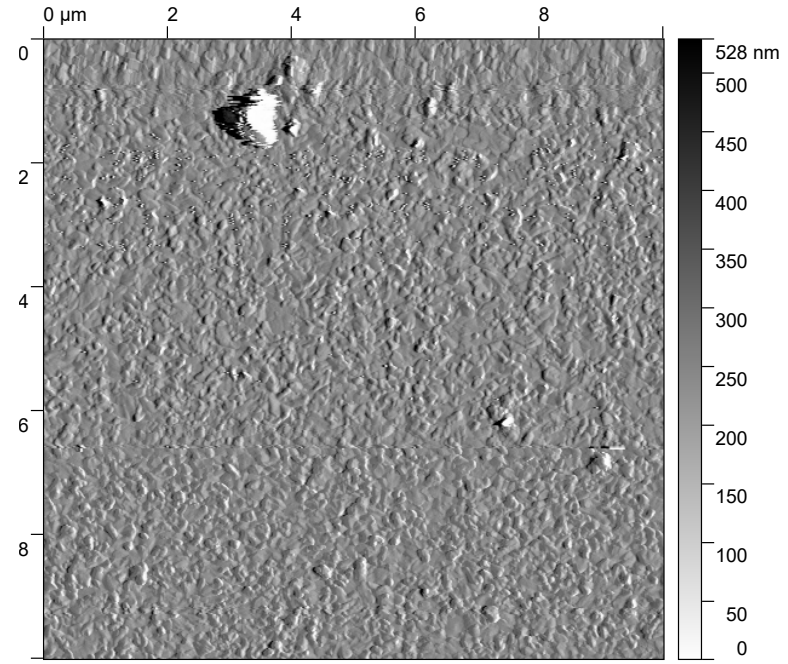

Figure 4.6 – 10 x 10 μm^2 AFM picture for sample *19WSi-3b*. Here, no blisters were observed. One big grain shifts the scale of height values. Mean result $R_q = 22$ nm of this sample was considered for this project.

4.2.2 Confocal Microscope Investigation

In the following, results of a CFM investigation are shown. This technique is based on the utilisation of a LED light source, a CCD camera, a multi-pinhole disc, a piezo drive and an objective. The light is focused through the multi-pinhole disc and objective onto the sample surface, where it gets reflected back through the system. In contrast to other optical microscopes, the multi-pinhole disc only allows transmission of light originating from reflections in the exact focal plane. Via usage of the vertical piezo drive, the sample surface can therefore get investigated via precise discretisation in height, resulting in a three-dimensional profile of a desired surface region. For more information regarding the CFM technique, please compare reference [43]. The CFM system used in the course of this thesis was a *NanoFocus* μ*surf* device, equipped with a 100x objective. The resulting three-dimensional data was obtained from 160 x 160 μm^2 regions of interest, which was posteriori evaluated by usage of a *PYTHON* code regarding R_q determination. It has to be mentioned, that the following pictures (figures 4.7 - 4.11) do not represent the quantitative data, but actual CFM photos of the surface with 100x magnification.
Visual results for the reference sample *18W4* (see figure 4.7) were in agreement with the observations from AFM, but the bigger region of interest provided a better overview and more reliable data. Therefore, quantitative R_q results based on the CFM technique were used as final roughness value.
Similar holds for investigations of the samples *19WSi-1a* and *19WSi-2b* (figure 4.8 and 4.9, respectively). Pyramidal structures with maximum sizes of about 10 μm were found for the first sample, which indicates a polycrystalline surface. *19WSi-2b* shows comparable pyramidal topologies, but with considerable less feature size. For both cases, quantitative values for R_q were taken from CFM, as the individual feature sizes were in satisfying agreement compared to the total image size. For the samples *19WSi-3a* and *19WSi-3c*, a complete coverage of the surface with blisters of various diameter was observed (compare figure 4.10). In contrast to the rougher samples, no pyramidal features were observed here, leading to the assumption that a certain threshold exposition time is needed for creation of such formations. In contrast to the other samples of batch *19WSi-3*, the specimen *19WSi-3b* was mostly showing no blisters. This is surprising, since all specimens of this batch originate from a simultaneous production process (compare section 4.1). It was recognised, that the height profiles measured via CFM for the batch *19WSi-3* consisted of many artefacts from reflections on the comparable flat surface. Thus, it was assumed that CFM method was on the edge of it's technical limits and R_q values were only considered from AFM measurements.

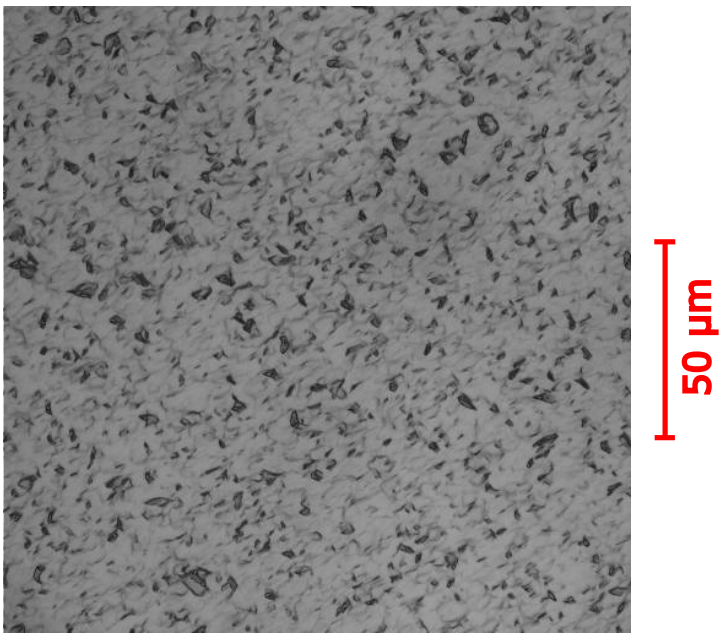

Figure 4.7 – 160 x 160 μm^2 CFM picture for sample *18W4*. The scaly structure can be investigated over the whole range of this reference sample. Obtained result $R_q = 226$ nm was considered for this project.

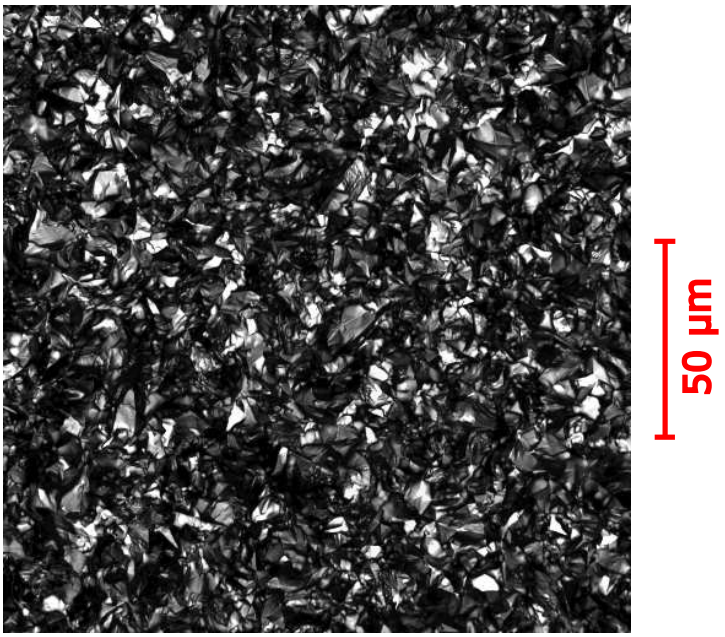

Figure 4.8 – 160 x 160 μm^2 CFM picture for sample *19WSi-1a*. Pyramidal structures with sizes around 10 μm were observed. Obtained result $R_q = 2343$ nm based on CFM was considered for this project.

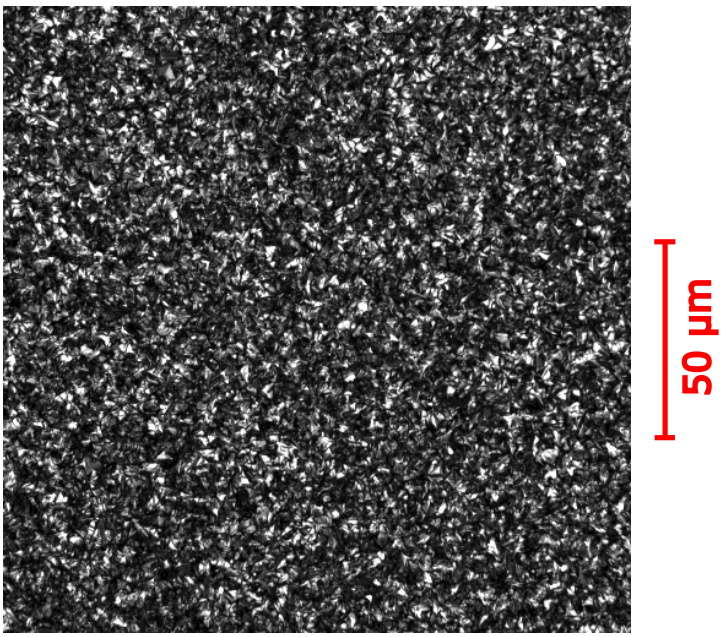

Figure 4.9 – 160 x 160 μm^2 CFM picture for sample *19WSi-2a*. Similar, but smaller pyramidal structures like in figure 4.8 were found. Obtained result R_q = 420 nm based on CFM were considered for this project.

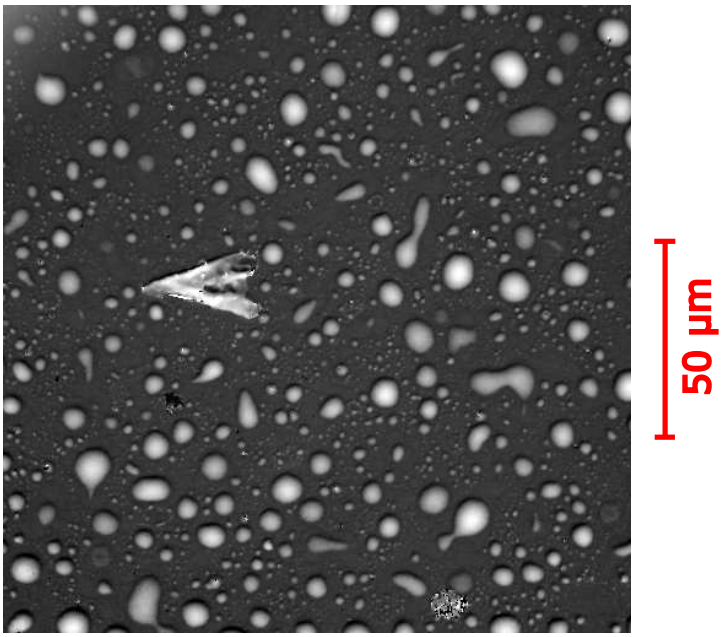

Figure 4.10 – 160 x 160 μm^2 CFM picture for sample *19WSi-3c*. Many blisters were observed with sizes up to 10 μm. Obtained R_q results from this method were not considered but taken from AFM. A similar topography was found for sample *19WSi-3a*.

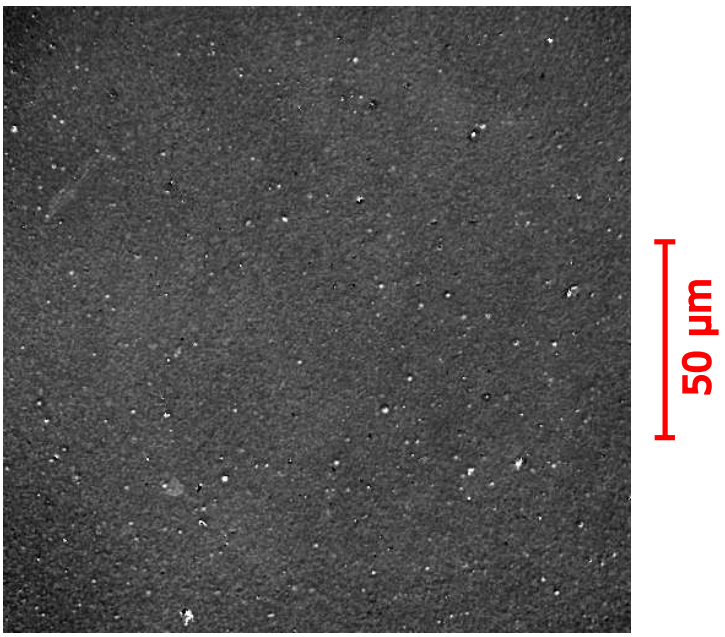

Figure 4.11 – 160 x 160 μm^2 CFM picture for sample *19WSi-3b*. Here, no blisters were observed. Sample appeared to be very flat, therefore R_q values were rather taken from AFM investigations.

Summary Roughness Evaluation:

In table 4.2, a summary of all measured R_q values is provided. The individual results were obtained by investigation of several positions on each sample. Especially for the roughest samples, results from individual regions scattered significantly, but were on the same order of magnitude.

Label	R_q [nm]	Method
18W4	226	CFM
19WSi-1a	2 343	CFM
19WSi-2b	420	CFM
19WSi-3a	29	AFM
19WSi-3b	22	AFM

Table 4.2 – Table with target sample R_q values. The method was considered based on the individual applicability. CFM - Confocal Microscopy, AFM - Atomic Force Microscope.

4.3 Local Surface Angle Distribution

Based on the AFM measurements and further data evaluation with a *PYTHON* code, also a determination of local surface inclination distributions was possible. The measured surface height points are connected with lines in order to form triangles, of which the surface normal vectors can get calculated individually. Via vector operations respective to the global normal vector $\vec{n}$ of the sample, a determination of the angular distribution was feasible. An example of such a result is shown for sample *18W4* in figure 4.12. Especially the values of most frequent angle δ_{max} and FWHM are additional parameters characterising a rough surface. The results for each sample is shown in table 4.3.

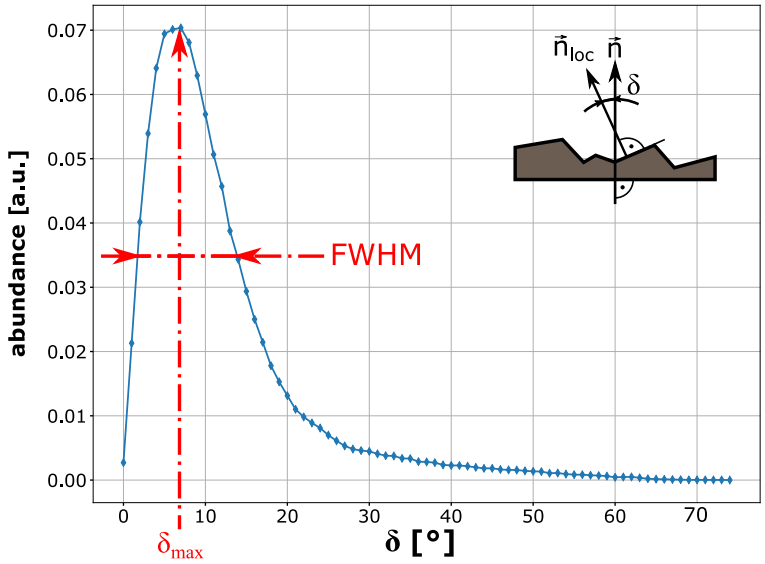

Figure 4.12 – Surface inclination angle distribution of *18W4*. For visualisation, the most frequent angle δ_{max} and the FWHM is added to the graph. This figure is shown as representative for all the determined distributions of the samples, which varied significantly.

Label	δ_{max} [°]	FWHM [°]
18W4	7.0	12.0
19WSi-1a	25.7	38.2
19WSi-2b	42.7	34.9
19WSi-3a	13.8	24.8
19WSi-3b	11.5	20.6

Table 4.3 – Table with key parameters of the inclination angle distribution for all samples. δ_{max} - Most frequent inclination angle, FWHM - Full Width Half Maximum of distribution.

4.4 Elementary Composition

In this section, insights into the target samples elementary composition are given. In order to prevent effects like preferential sputtering (see chapter 2), a check of the sample's coating purity needed to be undertaken. This was done via utilisation of the Elastic Recoil Detection Analysis (ERDA) technique executed at the *Ångströmlaboriet Uppsala, Sweden*. ERDA delivers information regarding elemental abundances over a depth of several hundred [nm] via sample exposition towards a highly energetic ion beam. In the case of investigations shown here, $^{127}_{53}\mathrm{I}^{8+}$ ions with a kinetic energy of 36 MeV collided with atoms from the sample. Recoil atoms were further detected, while a separation in energy and time of flight was possible. This formed a basis for elemental separation in the signal. More information regarding the ERDA technique is available in [44, 45]. At least one representative specimen per *19WSi* batch was investigated to check if impurities were abundant within the tungsten coating.

Figures 4.13 to 4.16 show the ERDA measurement results for the first 300 nm of thickness. For *19WSi-1b* (figure 4.13), the data shows in general a very dominant concentration of tungsten. Within the first 150 nm of depth, some impurities like oxygen, hydrogen and carbon were detected. Further, the tungsten signal did not significantly change over the total measured depth. Therefore, the coating thickness was beyond the range of this investigation method. Similar was found for sample *19WSi-2c* (figure 4.14). In contrast to *19WSi-1b*, also some traces of fluorine were detected, which could originate from the CVD process [46]. In addition, the abundance of silicon starts to rise at locations deeper than 200 nm, indicating a transition of the tungsten layer and the silicon substrate. This is even more dominant for sample *19WSi-3b* (figure 4.15), where this transition starts after 42 nm. Below 120 nm, silicon becomes the most dominant element, while the tungsten concentration decreases accordingly. A similar result was obtained for sample *19WSi-3c* (figure 4.16). *19WSi-3c* did show many blisters at the surface, while *19WSi-3b* did not. Compared to *19WSi-3b*, the data for *19WSi-3c* appears to be more scattered, but the general tendencies of the individual elemental abundances are very similar. Therefore, no indication for any differences regarding those two samples are visible in the elemental depth profiles.

Even though some impurities were found within the investigated samples, the top layer consisted of tungsten majorly. Highest integral values for the main impurities across the layer thickness were O $< 2.1\%$, C $< 1.3\%$ and H $< 0.6\%$ for all of the specimens. It was therefore assumed, that the samples were well suitable for the ion beam experiments in the course of this thesis, as long as the tungsten coating would not get depleted too much. This would especially form a limitation for the samples of batch *19WSi-3*, which show a comparable thin tungsten coating. The elemental composition of the tungsten coated quartz crystal *18W4* was investigated by *Reinhard Stadlmayr* in earlier studies, where a sufficient purity of tungsten was verified. The execution of ERDA investigations as well as the raw data evaluation was done by *Marcos V. Moro, Uppsala Universitet.*

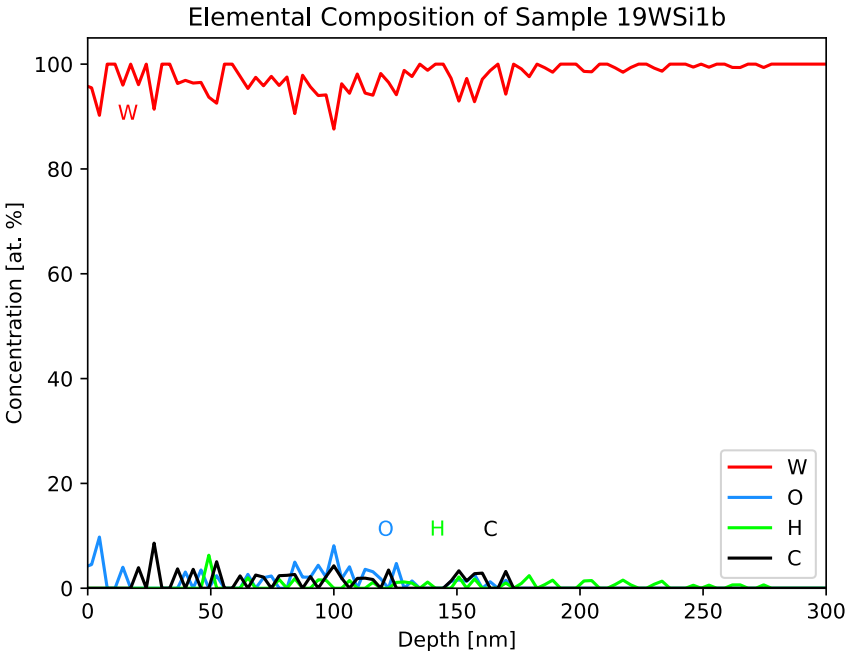

Figure 4.13 – ERDA results of *19WSi-1b*. The elemental concentration in [at.%] is plotted over the depth in [nm]. The tungsten thickness is beyond the range of measurement.

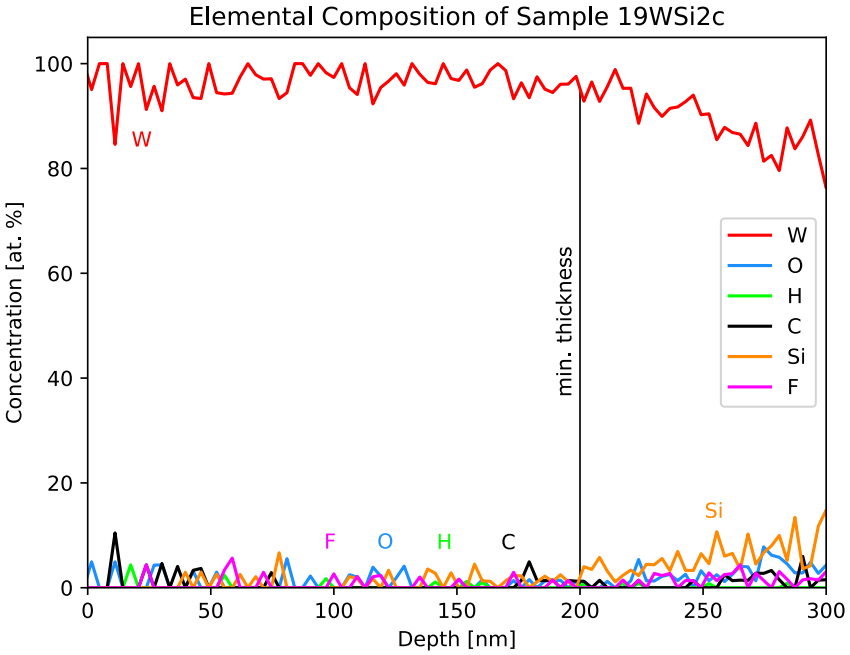

Figure 4.14 – ERDA results of *19WSi-2c*. The elemental concentration in [at.%] is plotted over the depth in [nm]. The W thickness is at least 200 nm, after which Si signal increases.

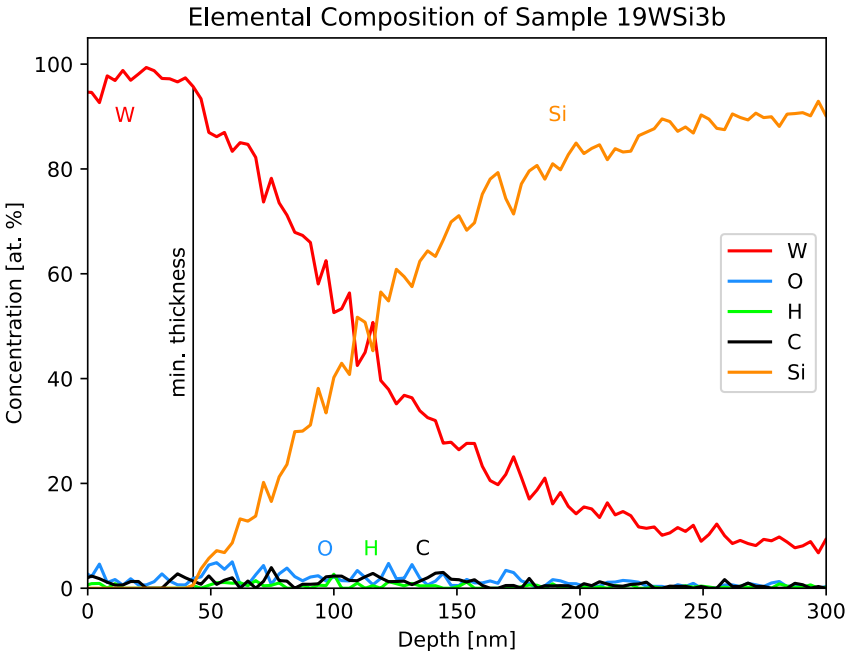

Figure 4.15 – ERDA results of *19WSi-3b*. The elemental concentration in [at.%] is plotted over the depth in [nm]. The W thickness is at least 42 nm, after which Si signal increases.

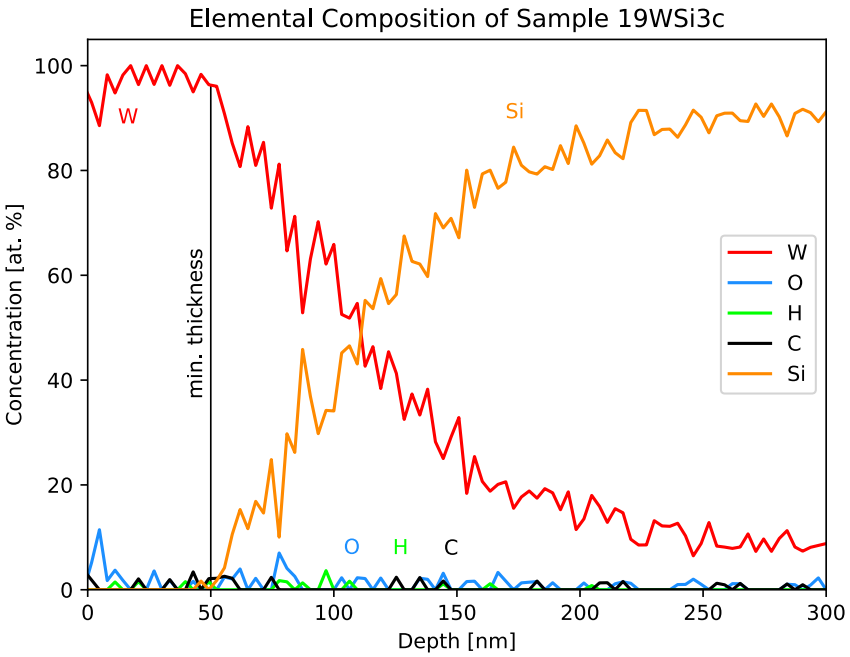

Figure 4.16 – ERDA results of *19WSi-3c*. The elemental concentration in [at.%] is plotted over the depth in [nm]. The W thickness is at least 50 nm, after which Si signal increases.

5 Results of Experiments

In this chapter, the experimental results obtained during this thesis are presented. Generally, two different experimental procedures were followed: *Linear Track* and *Circular Track* measurements. Both of them are based on Ar^{1+} bombardment of a target under fixed incident angle of 60° and catcher yield Y_C determination via a movable QCM (more details in section 3.2). The difference between the individual procedures can be seen in different positioning of the catcher QCM respective the target sample. Figure 5.1 highlights the geometrical characteristics of both approaches in respect to the target coordinate system.
In the beginning, results of the *Circular Track* measurements for all samples are shown in section 5.1, before the results on the basis of the *Linear Track* approach are presented in section 5.2. In order to complement the ion beam experiments, statements regarding the posteriori surface topology investigations are provided in section 5.3. After this, a quantitative comparison between the two different measurement approaches is undertaken in section 5.4. In addition, the integration of individual catcher yield fit functions yielded an estimation of the primary sputter yield Y_T also for the *19WSi* samples with varying roughness. Section 5.5 provides a discussion of the results and a comparison to outcomes of other studies.

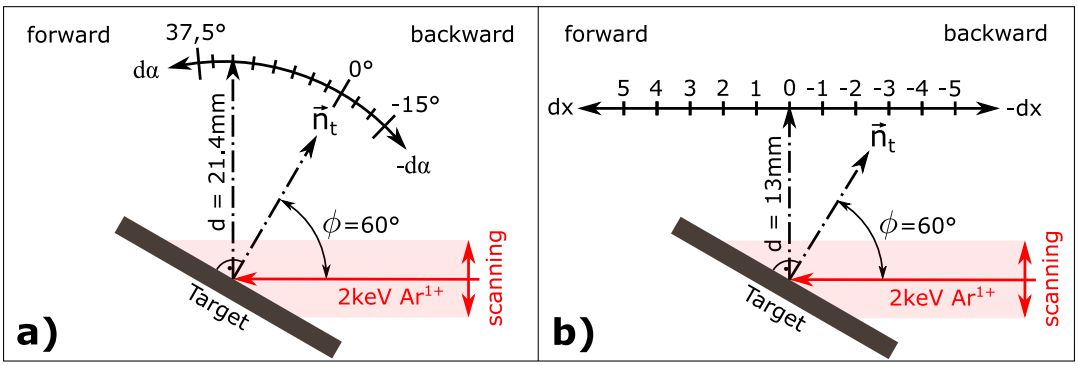

Figure 5.1 – Sketch of catcher QCM track geometries. The target is bombarded under the fixed incident angle $\phi = 60°$, while the ion beam is scanned over a projected square with 5 x 5 mm^2 size. Sputtering towards directions between the incoming ion beam and the surface normal $\vec{n}_t$ is denoted as *backward* sputtering, while *forward* sputtering aims beyond the surface normal. **a)** *Circular Track:* Catcher yield measurements were obtained with a fixed distance of 21.4 mm in an angular interval from -15° to 37.5° in steps of 5°. The last step towards 37.5° was a shift of 2.5° only. **b)** *Linear Track:* Catcher yield measurements were obtained with both fixed distance of 13 mm and tilt angle towards the laboratory y-axis, in a linear interval from -5 to 5 mm along the x-axis in steps of 1 mm.

5.1 Results Circular Catcher QCM Track

In this section, the experimental results on the basis of a *Circular Track* catcher QCM approach are presented. This procedure was characterised by a constant distance d = 21.4 mm between the catcher quartz centre and the target (see figure 5.1 a). In addition, the surface normal of the catcher quartz was always pointing towards the target sample centre. This forms an advantage in contrast to the *Linear Track* approach, where those geometrical properties change during the experimental progress and lead to a substantial influence on the measured signal (compare section 3.2.2 for more details). In total, measurements of the catcher yield were obtained over an angular interval between -15 and 37.5° with an increment of 5°. The experimental data set of each sample was subsequently fitted via a polynomial of order 6 for further data evaluation. The results can be seen in figure 5.2.

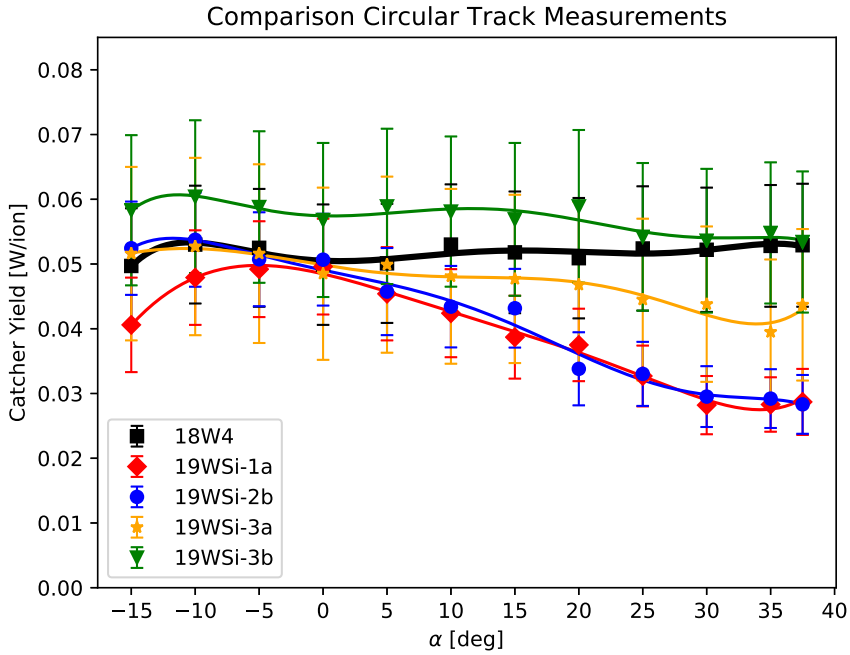

Figure 5.2 – Results for *Circular Track* catcher yield measurements with 2 keV Ar^{1+} irradiation of the targets under 60°. The measured values of Y_C are plotted over the angular interval of -15 to 37.5° for all samples, considering also the absolute errors. Polynomial fits are shown in the colours of the underlying data set.

Black squares with corresponding errorbars represent results for the reference sample *18W4*. The tendency of this plot, which is also highlighted via the black polynomial fit, is relatively constant over the angular interval with a value of 0.05 W/ion. Since this sample was a quartz crystal, a determination of the target sputter yield Y_T was feasible via the *Target QCM Approach* (see section 3.2.1) during simultaneous catcher QCM measurements. The

resulting value of $Y_{T,ref}$ was 1.95 ($\pm$ 2.87%) W/ion, and furthermore of high importance for subsequent sputter yield determinations of the other samples.
Results for sample *19WSi-1a*, which had the highest R_q value, are presented via red diamonds. In contrast to the reference sample, a substantial decrease of the catcher yield Y_C can be seen for angles in the *forward* sputtering regime ($\alpha > 0°$). For positions close to the surface normal direction ($\alpha = 0°$), similar values as for the reference sample were obtained. With increasing angle α, the tendency continuously decreases down to a value of 0.03 W/ion. Similar results were obtained for sample *19WSi-2b*, which had (in comparison to the other samples) intermediate R_q values. The trend indicated via the blue points follows the values of sample *19WSi-1a*, except for angles in the *backward* regime. Here, the catcher yield Y_C rather remains at a level of 0.05 W/ion, comparable to the reference sample tendency. Yellow asterisks highlight the results obtained for sample *19WSi-3a*. It was characterised by rather low R_q values and did show blisters on the surface (compare section 4.1). Especially in the *backward* angular regime between -15° and 0°, catcher yield values similar to the reference sample were measured. With increasing angle in respect to the target surface normal, the values decreased slightly to a level of about 0.04 W/ion.
Sample *19WSi-3b* had a similar roughness value as *19WSi-3a*, but did not show any blisters on it's surface. Results for the corresponding Y_C values are indicated via green triangles, revealing values higher than for the reference sample. Starting from an angle α of -15°, the value of Y_C decreases from an initial maximum of 0.06 W/ion continuously, until it reaches the reference sample value of 0.05 W/ion at 37.5°. It is interesting, that an almost constant offset of 0.01 W/ion can be recognised between the trends of *19WSi-3a* and *19WSi-3b* over the whole angular interval.

5.2 Results Linear Catcher QCM Track

Similar to earlier studies at the IAP TU WIEN, catcher yield measurements following the *Linear Track* procedure were undertaken. The tilt mechanism was fixed towards a catcher quartz orientation along the laboratory y-axis for all measurements, while the catcher QCM was moved along the x-axis in increments of 1 mm between -5 and 5 mm (compare figure 5.1 b). The (projected) distance d = 13 mm was significantly smaller compared to *Circular Track* measurements, but increased for positions different than dx = 0 mm. Also, the projection of the catcher quartz surface varied for different positions.The results of the *Linear Track* approach for all samples are presented in figure 5.3. Black squares highlight the results for the reference quartz target *18W4*. The maximum of Y_C = 0.12 W/ion can be found at position dx = 2 mm, which is in the backward sputtering regime (compare figure 5.1). For positions more negative, the trend gradually decreases until it reaches it's lowest value of about 0.78 W/ion at dx = -5. For positions higher than dx = 2, also a decrease can be seen with a final value of approximately 0.10 W/ion.
For sample *19WSi-1a*, an almost linear decreasing trend can be identified over the range

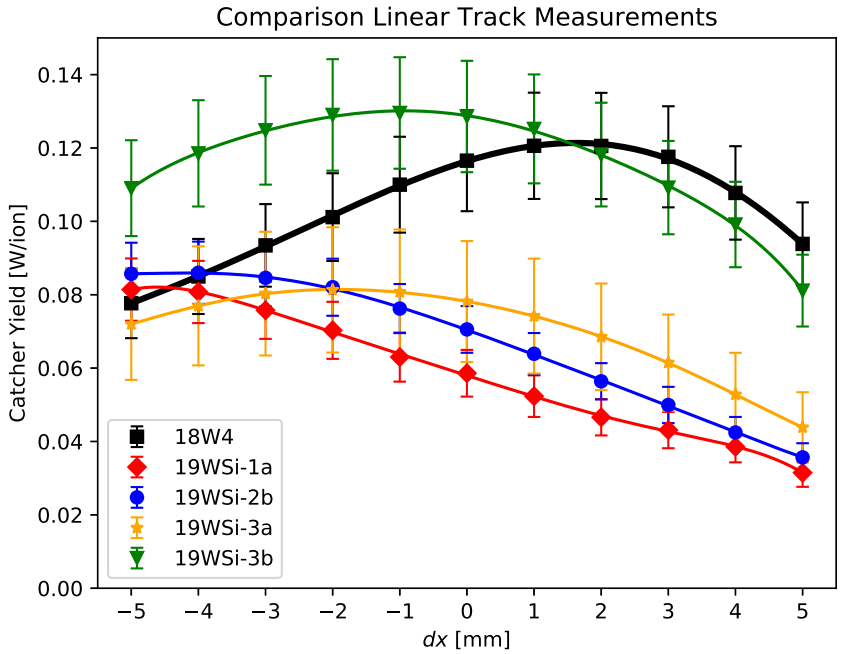

Figure 5.3 – Results for *Linear Track* catcher yield measurements with 2 keV Ar^{1+} irradiation of the targets under 60°. The experimentally measured catcher yields Y_C are plotted over the linear interval for all samples, considering also the absolute errors. Polynomial fits are shown in the colours of the underlying data set.

of the position interval. Starting with a value of 0.08 W/ion at dx = -5 mm, which is comparable to the reference sample value at this position, the tendency falls until it reaches a level of 0.03 W/ion at dx = 5 mm.
Similar trends can be found for the results of sample *19WSi-2b*, which has slightly higher Y_C values over the whole interval and a slightly negative curvature.
The results of sample *19WSi-3a* were characterised by a maximum Y_C value of 0.082 at position dx = -2 mm. Towards more negative values of dx, the tendency falls to 0.072 W/ion, which is slightly less than the reference value. In the *forward* sputter regime, the decrease of Y_C values proceeds down to a value of 0.044 W/ion.
Similar as for the results shown in section 5.1, the values obtained for sample *19WSi-3b* were higher than the reference for a wide range of the dx-interval and the tendency appeared similar to *19WSi-3a* but with a certain offset. The maximum of the trend can be found at dx = -1 mm with a value of 0.13 W/ion. In the direction of the *backward* sputter regime, a decrease is occurring until a final value of 0.11 W/ion is reached at dx = -5 mm. In the opposite direction, also a decrease in the trend can be observed, resulting in the final value of 0.08 W/ion. The measurement set of the reference sample *18W4* was utilised for publication of a scientific paper [20].

5.3 Post-Experimental AFM and CFM

As mentioned in section 4.4, it is important check if the sample's tungsten coating was not eroded too much during the experimental procedures. This is of fundamental importance for the results obtained in the course of this thesis, since temporal modifications were not taken into account for the interpretation of results. Initially, a rule of thumb calculation which considered a regularly obtained total ion fluence per sample of 1.5×10^{20} ions/m^2 and an approximate sputter yield $Y_T \approx 2$ W/ion, resulted in an estimated surface erosion of only 4.7 nm, considering an areal density of 6.3×10^{15} W/(cm^2·nm) for tungsten. A comparable surface erosion depth of 4.6 nm was also determined via usage of the one-dimensional BCA simulation code *TRIDYN*, which considered flat tungsten bombardment under 60° Ar^{1+} incidence [35]. Therefore, surface modifications were not expected to play a significant role during the ion bombardment.
Reproducibility tests did furthermore not show any indication of variations due to increasing fluence. In contrast, significant modification of the surface would have resulted in substantial impacts on the measured Y_C values. In order to double-check if the surface topography was modified during the experiments or not, posteriori CFM investigations were executed.
In accordance to the initial assumptions, no changes in the surface topology were found for any of the samples. Especially for the visual results, no difference to the pictures created prior to the ion beam experiments were recognised. Also calculated R_q values did not indicate severe changes in the surface roughness. It was therefore assumed, that temporary effects can be neglected for all obtained results in the prior sections. Posteriori AFM investigation was not possible, as the device was out of order due to maintenance work and not available until completion of this document.

5.4 Experimental Data Analysis

In this section, the experimentally obtained results from the catcher yield measurements were used for further quantitative analysis. At first, a direct comparison of the results from *Circular Track* and *Linear Track* approach is performed. Afterwards, a re-calculation of the target sputter yields Y_T on the basis of an integration method is executed.

5.4.1 Quantitative Comparison of Catcher Yield Profiles

A direct comparison of the determined catcher yield values between both *Circular Track* and *Linear Track* approach is only possible for a special subset of the data. For the *Linear Track* approach, the data points obtained at dx = 0 mm were measured with catcher orientation along the laboratory y-axis (compare figure 3.1) and a distance of 13 mm towards the

target. In the frame of the *Circular Track* approach, similar geometrical conditions were only established for $\alpha = 30°$, but with an absolute distance of 21.4 mm. Since Y_C can be assumed to follow an intensity law, a quadratic dependence of on the absolute distance d can be estimated.

$$Y_C \sim \frac{1}{d^2} \tag{5.4.1}$$

The ratio R of these individual Y_C values from both experimental approaches should therefore scale with the reciprocal ratio of quadratic distances:

$$R = \frac{Y_{C,lin}}{Y_{C,circ}} = \left(\frac{d_{circ}}{d_{lin}}\right)^2 \tag{5.4.2}$$

Via insertion of $d_{circ} = 21.4$ mm and $d_{lin} = 13$ mm into equation (5.4.2), a value of $R = 2.71$ was calculated. As a next step, the corresponding value of R was also determined for each sample via the corresponding Y_C values of both *Linear Track* and *Circular Track* approach, which are listed in table 5.1. In comparison to the geometric value R, all of the values calculated via the ratio of catcher yields were smaller. Especially for sample *19WSi-3a*, a substantially lower value was recognised.

Label	**Ratio R**
Geometric	2.71
18W4	2.09
19WSi-1a	2.14
19WSi-2b	2.36
19WSi-3a	1.73
19WSi-3b	2.36

Table 5.1 – Table with calculated ratios R for direct comparison of catcher yield values obtained via *Linear Track* and *Circular Track* approach. Only a subset of the data was compared, which originated from measurements with the same catcher QCM orientation along the laboratory y-axis.

5.4.2 Reconstruction of Sputter Yields Y_T

In order to determine target sputter yield Y_T values also for the samples *19WSi*, a procedure as described in the following paragraph was executed: As a start, the polynomial fit functions for the catcher yield which originated from the *Circular Track* approach (see figure 5.2) were numerically integrated over the whole angular interval. The ratios between integrals of samples *19WSi-xx* were calculated in respect to the integral of reference sample *18W4*, which was utilised to scale the determined reference sputter yield $Y_{T,ref}$. This is mathematically formulated in equation (5.4.3):

$$Y_{T,i} \;=\; Y_{T,ref} \cdot \frac{I_i}{I_{ref}} \tag{5.4.3}$$

Via equation (5.4.3), the individual sputter yields $Y_{T,i}$ for each sample of the set *19WSi-xx* can get calculated, if the reference sputter yield $Y_{T,ref} = 1.95$ W/ion and the corresponding integrals I_i and I_{ref} are considered. Since this procedure is utilising both experimentally determined parameters and calculated quantities, the expectable error for this approach is of certain interest. By application of the gaussian error propagation law, an estimate for the absolute error $\Delta Y_{T,i}$ can be given via equation (5.4.4) (further literature: [47]).

$$\Delta Y_{T,i} = \sqrt{\left(\frac{\partial Y_{T,i}}{\partial Y_{T,ref}}\right)^2 \cdot \left(\Delta Y_{T,ref}\right)^2 + \left(\frac{\partial Y_{T,i}}{\partial I_i}\right)^2 \cdot \left(\Delta I_i\right)^2 + \left(\frac{\partial Y_{T,i}}{\partial I_{ref}}\right)^2 \cdot \left(\Delta I_{ref}\right)^2} \tag{5.4.4}$$

Via division of $\Delta Y_{T,i}$ by the corresponding integral value $Y_{T,i}$, the relative error $\sigma_{T,i}$ in percent can get calculated.

$$\sigma_{T,i} = \frac{\Delta Y_{T,i}}{Y_{T,i}} \tag{5.4.5}$$

The error $\Delta Y_{T,ref}$ is known from a multitude of target sputter yield measurements with the quartz sample *18W4*. For the errors of the integrals ΔI_i and ΔI_{ref}, further assumptions were made as follows: Each data point of a measurement set had a corresponding error, calculated during the data analysis procedure described in section 3.4. As a first step of a conservative error estimation, the biggest relative error of all measured points of a set was identified and further considered as error of the respective integral. Via multiplication with it's value I_i, a value for ΔI_i was determined. This strategy was also followed to calculate ΔI_{ref}. The results for Y_T on the basis of integrating the catcher yield profiles from the *Circular Track* approach are listed in table 5.2 for comparison.
In addition, the reconstruction of Y_T was also performed via usage of the catcher yield profiles based on the *Linear Track* approach. The same procedure as described via equations (5.4.3 -5.4.5) was followed, leading to the results presented in table 5.3.

Label	Y_T [W/ion]	σ_T [%]	R_q [nm]	FWHM [°]
18W4	1.95	± 2.87	226	12
19WSi-1a	1.51	± 25.94	2 343	38.2
19WSi-2b	1.58	± 25.06	420	34.9
19WSi-3a	1.79	± 33.96	29	24.8
19WSi-3b	2.16	± 28.14	22	20.6

Table 5.2 – Table with reconstructed target sputter yields Y_T from the *Circular Track* measurements. For *18W4*, the sputter yield was measured directly on the basis of a *Target QCM Approach* (compare section 3.2.1). Via integration of the catcher yield tendencies shown in figure 5.2, the sputter yield calculation was feasible also for the other samples. In addition, also the relative errors are listed, which originate from a gaussian error propagation procedure.

Label	Y_T [W/ion]	σ_T [%]	R_q [nm]	FWHM [°]
18W4	1.95	± 2.87	226	12
19WSi-1a	1.08	± 17.36	2 343	38.2
19WSi-2b	1.24	± 16.39	420	34.9
19WSi-3a	1.31	± 25.10	29	24.8
19WSi-3b	2.17	± 17.37	22	20.6

Table 5.3 – Table with reconstructed target sputter yields Y_T from the *Linear Track* measurements. For *18W4*, the sputter yield was measured directly on the basis of a *Target QCM Approach* (compare section 3.2.1). Via integration of the catcher yield tendencies shown in figure 5.3, the sputter yield calculation was feasible also for the other samples. In addition, also the relative errors are listed, which originate from a gaussian error propagation procedure.

5.5 Discussion of Experimental Results

In this section, a discussion of the experimental results is undertaken. At first, the characteristics of catcher yield measurements are highlighted, before the reconstructed sputter yield values are discussed in detail.

As a start, a focus is put on the *Circular Track* catcher measurements (see figure 5.2). The results of sample *18W4* indicated a profile which was almost constant and comparably high over the whole range of angles α. Even though the roughness value R_q was found to

be comparable with sample *19WSi-2b*, a significant difference in the resulting catcher yield profiles was found. Via consideration of the surface inclination angle distribution parameters, the differences in topology become more clearer. The images obtained via AFM (see 4.2) highlighted, that the surface of sample *18W4* was mostly flat, providing only a few surface features for redeposition of sputtered tungsten atoms.
Another key result of the *Circular Track* measurement was, that a preferential emission of sputtered tungsten atoms along the target surface normal was found for the rougher samples *19WSi-1a* and *19WSi-2a* (compare figure 5.2). Even though their R_q roughness value differed by more than a factor of 5, almost the same catcher yield profile was determined. Nevertheless, a similarity of those samples can be found in the FWHM parameters of surface inclination angle distributions. By comparison of the optical images 4.8 and 4.9, a self-similar pyramidal structure can be found on the surface of both samples.
The samples of batch *19WSi-3* shared similar R_q and also surface inclination distribution parameters. The tendencies of their *Circular Track* catcher yield profiles are comparable, even though an offset can be recognised over the whole angular interval. Generally, the properties regarding surface inclination angle distributions appeared to have a stronger effect on the erosion characteristics than the roughness value R_q.

Now, the *Linear Track* measurements are reflected. In general, the variable geometrical parameters of the *Linear Track* approach significantly influenced the catcher yield values on the individual dx positions (see figure 5.3). In combination with projection effects, an interpretation of these tendencies becomes more challenging. Similar to the main outcome of the *Circular Track* approach, the tendency of the individual Y_C profiles seems to be lower for rougher samples than for the smoother ones. Results for samples *19WSi-1a* and *19WSi-2a* did again show comparable characteristics. In contrast, the offset between the Y_C profiles from samples of batch *19WSi-3* became even more dominant.

The quantitative comparison of the catcher yield profiles did generally show lower ratios R compared to the ideal geometric value. Especially for sample *19WSi-3a*, significant discrepancies were revealed (compare section 5.4.1). Subsequent studies of this sample under 45° ion incidence, which were executed by *Lea Fuchs, IAP TU WIEN*, did show Y_C profiles with a better agreement in terms of the ratio R. The absolute values of the catcher yield for the *Circular Track* measurements were similar, which supports assumptions, that the results for sample *19WSi-3a* obtained during this thesis via the *Linear Track* approach (see figure 5.3) were rather underestimated. Therefore, this data set may be taken into account only with awareness. It has to be mentioned, that also other geometric effects induced via the ion beam scanning or the resulting solid angle of the catcher quartz surface may need to be considered for a more detailed comparison on this basis.

The reconstruction of sputter yields Y_T was performed via usage of both catcher measurement approaches. In general, increasing roughness did lead to smaller sputter yield values. Similar to the outcomes discussed respective the catcher yield profiles, a comparable sputter yield of about 1.55 W/ion was found for samples *19WSi-1a* and *19WSi-2a* from evaluations of the *Circular Track* data. The highest sputter yield of 2.16 W/ion was found for sample

19WSi-3b, which had the lowest R_q roughness value. The calculated data originating from the *Linear Track* approach did show a stronger decrease of Y_T with increasing roughness R_q than the *Circular Track* data. Nevertheless, a similar result for the calculated sputter yield of the smoothest sample*19WSi-3b* was obtained via both approaches.

Via the determination of target sputter yields Y_T for highly corrugated samples, a first application of the new catcher QCM apparatus was successfully demonstrated. These results were further considered for the progress of the *EUROfusion PFC-SP2.4* task and presented during the corresponding *SP2 Annual Meeting* of 2019. Detailed literature research focusing on rough tungsten surface sputtering via argon ion bombardment was not successful. Nevertheless, publications were found which a scope on similar key aspects, like the influence of roughness on the erosion of other materials under different ion bombardment conditions. A more liberal comparison is obtained by consideration of following studies.
A decrease of the absolute target sputter yield for increasing roughness was also found for studies of *Küstner et.al.* [21]. Here, a graphite sample under 2 keV deuterium irradiation with R_q values on the μm scale did show reduced sputter yields especially for ion incident angles higher than 45° (in comparison to a flat sample). Experiments in the course of this thesis were performed under 60° of incidence, and similar observations were found as well. An additional conclusion of this publication is, that the sputter yield of the rougher sample was less variable for different ion incident angles, which was interpreted as an effect from a broad FWHM value of the surface inclination angle distribution. To study this effect for argon ions on tungsten, more experimental data for different ion incidences than 60° would be necessary.
In a study elaborated by *Li et.al.* [23], also a catcher QCM method was utilised to determine the sputter yield of molybdenum samples under 300 eV Ar^{1+} bombardment under 0° incident angle. Compared to a flat sample, the sputter yield was reduced to a level of about 60%. A similar trend can be found in the results of this thesis, where the sputter yield of the roughest sample *19WSi-1a* was about 70% of the flattest specimen *19WSi-3b*. Since the plasma discharge ion source utilised for the cited study provided highly intense ion fluxes, also temporal effects of surface modification revealed a continuous increase of the rough surface sputter yield towards the values obtained for flat molybdenum. In contrast, temporal effects were much less relevant for experiments in the course of this thesis, since much less surface modification occurred during bombardment with a comparable low flux ion source.

6 Comparison to Simulations

Via simulations on the basis of the BCA code *TRI3DYN*, a comparison of numerical data with respect to experimental results was feasible [34]. The execution of simulations was done by *Reinhard Stadlmayr,* IAP TU WIEN. In the following sentences, a short description regarding the specific simulation procedure is given in addition to general information provided in section 2.3. Initially, a set of eight virtual surface topologies with a size of 200 x 200 nm^2 and R_q values between 3 and 150 nm was created by usage of a *PYTHON* code [36]. The surfaces were used as input for the simulations, which were considering Ar^{1+} impact with 2 keV energy under 60° of incidence. The simulations were executed in *static* mode, which did not consider temporal surface modifications. In addition, only pure tungsten was assumed for all simulations. It is important to mention, that the computational volume is substantially limited in size, which forms a limitation for creation of surfaces with roughness values higher than 100 nm. Similar to the argumentation regarding AFM applicability in respect to samples with R_q values on the μm scale, the simulation code may not be assumed to create reliable results for topographies, where individual surface features fill almost the whole computational volume.
During the simulation, the target was bombarded with a number of 4 million pseudo-particles. Each particle is shot towards a random surface position, where a collision cascade was calculated. Next to a wide range of other parameters, the number of successfully sputtered tungsten particles as well as their individual velocity vector was recorded. Via increasing number of simulated pseudo-particles, the statistics of this approach became better.
In the following, numerical results for the target sputter yield Y_T for all virtual surfaces and their corresponding R_q value are shown in contrast to the experimentally determined values from chapter 5 in figure 6.1.
The trend of the simulated values of Y_T is characterised by a strong decline over increasing roughness, which starts already for comparable small R_q values. For $R_q = 3$ nm, a target sputter yield of 2.17 W/ion was found, which appears similar to the calculated value of the experimental sample *19WSi-3b* ($R_q = 22$ nm). For increasing roughness, the trend settles at a level of about 0.8 W/ion between 40 and 100 nm. For the roughest simulated surface topology with $R_q = 150$ nm, the value of Y_T dropped to 0.5 W/ion. In general, the experimentally determined values of Y_T were higher than the numerical results.
The target sputter yields were calculated via the ratio between total pseudo-particle number and the number of successfully sputtered particles. Via usage of the calculated velocity vector for both sputtered particles and for reflected Ar^{1+} ions, also a reconstruction of the catcher yield Y_C was feasible. Similar to the experimental results for the *Linear Track* approach (compare section 5.2), the catcher QCM position was swept in a interval between -5 and

5 mm. The geometrical relations between target and catcher QCM were considered, such that a successful tungsten atom catching event was assumed if the direction of the velocity vector was in agreement with a position on the catcher quartz surface. The number of all virtually caught particles was subtracted by the total amount of secondary sputtered atoms from the catcher and further divided by the total number of pseudo-particles. This resulted in an estimation for the catcher yield Y_C at a certain position dx. More details regarding this procedure can be found in reference [20].

The absolute values for Y_C calculated by *TRI3DYN* were about one order of magnitude lower than the experimental results shown in figure 5.3. Independent of the numerical result's tendencies, this constitutes a fundamental discrepancy between the simulations and experimental data. In order to obtain a comparison of the individual trend lines in respect to selected experimental data sets, the simulated results were rescaled via their individual maximum Y_C value. The results of this procedure are presented in the figures 6.2 and 6.3, which cover a subset of four simulations, respectively. For the numerical data set 1, the tendencies were rescaled towards the results of *19WSi-3b* (R_q = 22 nm), which had the lowest roughness value of all experimental samples. In contrast, the second numerical data set was rescaled in respect to the results of *19WSi-1a* (R_q = 2 343 nm), where the highest roughness value was determined.
As can be seen in figure 6.2, a good agreement in tendency was found for rescaled simulated results of R_q = 10 nm and the trend of *19WSi-3b*. Both curves share a maximum value at dx = -1 mm, while a similar decrease off from this position is recognised within the error bars of the experimental results. For the virtual surface with R_q = 20 nm, the tendency shows significant differences, even though the roughness value would be similar to sample *19WSi-3b*.
In figure 6.3, the best agreement of tendency is found for the simulation of R_q = 100 nm in respect to the experimental sample *19WSi-1a*. In this plot, also an inconsistent evolution for the numerical result trend lines over increasing roughness can be recognised. While R_q values 60, 80 and 100 nm show a continuous shift of the maximum value towards the negative dx regime, a different trend can be investigated for R_q = 150 nm. Here, the trend line settles at a plateau for positions between dx = -5 and -1 mm.
It has to be mentioned, that the roughness values of the virtual surfaces were in general much lower than for the roughest experimental samples. Nevertheless, the simulations show even more drastic influence of the surface roughness on both sputter and catcher yield values than found experimentally. More efforts regarding modelling of the surface inclination angle distribution could provide a basis for better agreement between the results. In addition, a higher amount of pseudo-particles could further improve the statistics of the simulations.

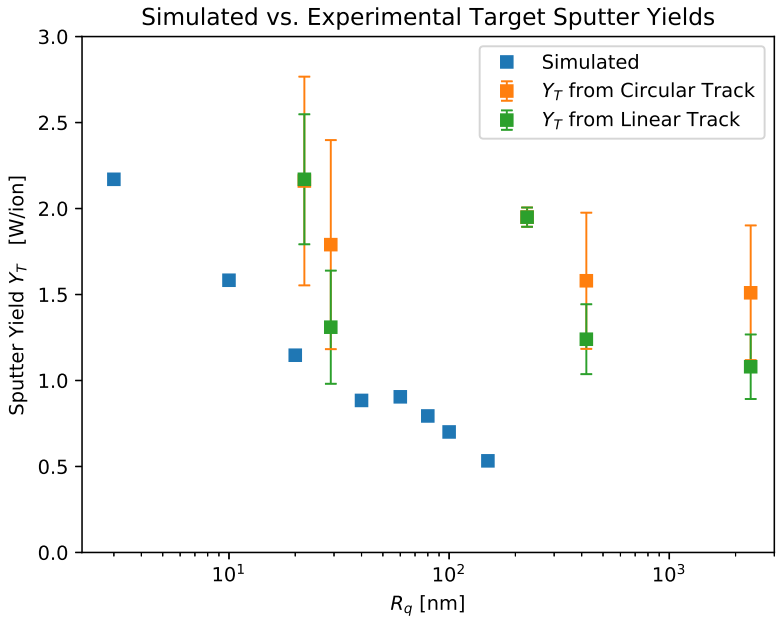

Figure 6.1 – Numerical Results for the sputter yield Y_T vs experimental values. The blue squares represent the results for simulations, where virtual surface topologies were utilised as input. The orange and green data sets represent experimental data from chapter 5.

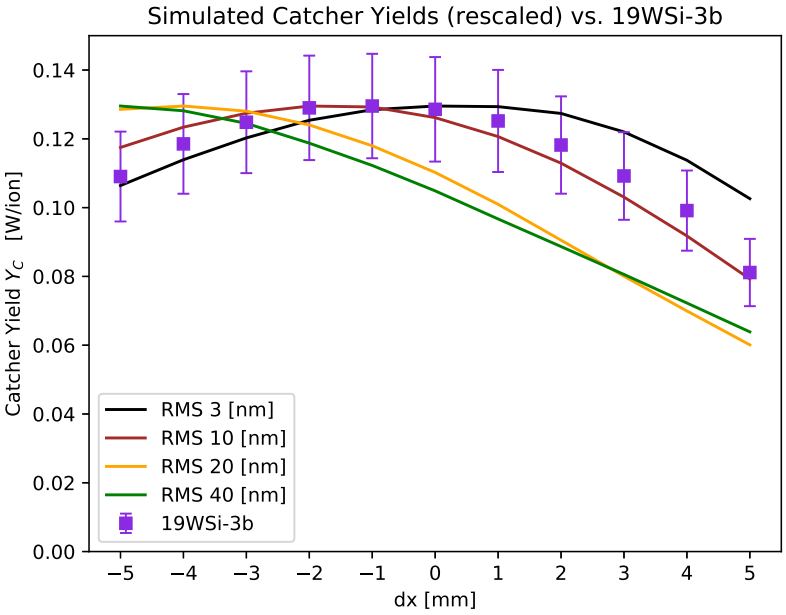

Figure 6.2 – Normalised numerical results for the catcher yield (Set 1). The simulated tendency of Y_C is rescaled in respect to the maximum measured value of sample *19WSi-3b* and plotted over the position interval from -5 to 5 mm.

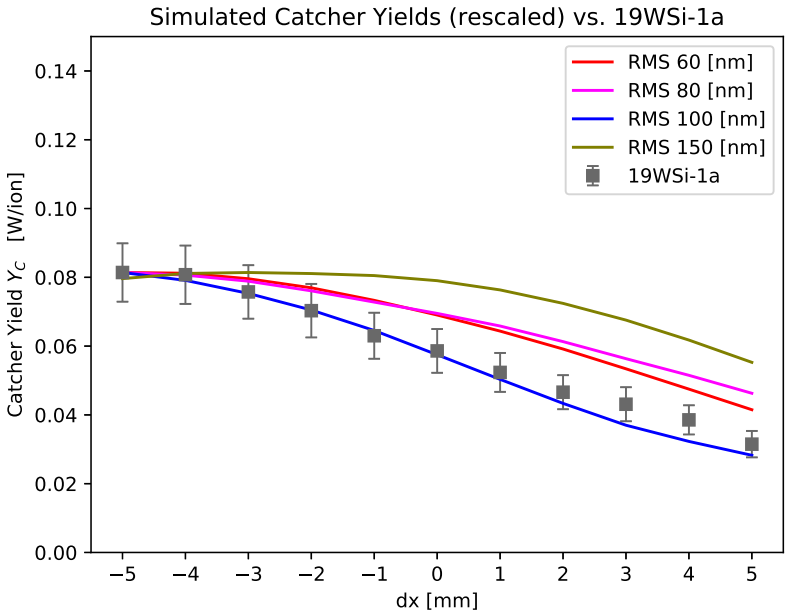

Figure 6.3 – Normalised numerical results for the catcher yield (Set 2). The simulated tendency of Y_C is rescaled in respect to the maximum measured value of sample *19WSi-1a* and plotted over the position interval from -5 to 5 mm.

7 Conclusions and Outlook

This chapter summarises the main results of this master thesis and offers a reflection between initially stipulated key tasks and the final outcomes. In addition, limitations and ideas for future studies are mentioned.

In the beginning of the project, substantial efforts were invested to develop a catcher QCM system for ion beam erosion studies. The design was strongly influenced by already operating systems and accumulated knowledge at the IAP, TU WIEN. In contrast to earlier developed catcher QCM designs, the new apparatus was able to provide more degrees of freedom in three linear and one rotational directions of movement, which forms a substantial advantage. In addition, this system does not necessarily demand a quartz crystal as target, which provided more flexibility regarding sample utilisation. A main part during the development was also to calibrate this system, such that the experimental data satisfied demands regarding reproducibility. A generalised protocol for utilisation of the new apparatus was created in order to support the comparability of the results with future studies.

After a successful development of the experimental method, which can be identified as first solved milestone of this thesis, application was undertaken in the course of a research task defined by collaboration with the *EUROfusion* network. As stipulated in the main goals of the *PFC-SP 2.4.2* campaign in 2019, experimental data regarding the sputter yield Y_T of rough tungsten surfaces was required. Silicon platelets with a top layer of CVD deposited tungsten were chosen as targets for sputtering investigations, which were performed by exposition to Ar^{1+} ions with a kinetic energy of 2 keV under incident angle of 60°.

As initial step, a detailed characterisation of the target samples with respect to their surface topology and elemental composition was performed. Via usage of AFM, R_q values and also representative images were obtained especially for the smoother samples. This method was reaching it's technical limits for the roughest samples. Due to this, the CFM technique was utilised to complement the roughness evaluation. In addition, the AFM technique also facilitated a determination of the surface inclination angle distribution, which offered another parameter for sample surface characterisation. In order to validate the top layer tungsten purity of the CVD coated samples, ERDA experiments were performed, revealing only negligible amounts of impurities.

The catcher yield Y_C was determined at positions following both a circular and a linear path around the target. The tendencies of these data sets were further compared to results obtained during a reference experiment, where both a target and catcher QCM were utilised. Via this, an indirect determination of the desired target sputter yields was feasible, even though the experimental errors of this method were significantly higher than for direct sputter yield determination. A major outcome was, that the sputter yields Y_T tend to decrease

for higher roughness of the sample surface (compare section 5.4.2) which was similar to the results of other studies [21,23]. This is estimated to be beneficial for future nuclear fusion reactors, where materials with low sputtering yields are favourable and also a technical surface roughness can be expected on the inner coating of the reactor vessel. Nevertheless, surface roughness may induce other problems, like i.e. higher tritium retention in the first wall [48]. Another key result of this thesis was, that R_q roughness values alone are not sufficient to fully characterise influences of roughness on sputtering. Also the surface inclination angle distribution is of importance, which was clearly observed for the reference quartz sample *18W4*. Even though it had a comparable moderate R_q value of 226 nm, the catcher yield signal revealed a rather high and homogeneous trend, which was even higher than for sample *19WSi-3a* with a $R_q = 29$ nm. In contrast to this, the parameters δ_{max} and FWHM of *18W4* appeared smaller than for *19WSi-3a*, which is in agreement with the visual results in figure 4.2. Even though some elevated peaks were visible and definitely increased the total R_q value, they appear to be separated wide enough such that redeposition plays only a minor role. In between, a scaly surface with low roughness provided a good starting point for sputtering processes. In the AFM image of *19WSi-3a* (see figure 4.5), the comparable flat surface did show a texture on the nm scale. The FWHM of the surface inclination angle distribution was higher than for the reference quartz, which could potentially be the reason for substantial local redeposition. On the contrary, sample *19WSi-3b*, which had a strong similarity to *19WSi-3a* except of the blister formation, delivered even higher catcher yield values than the reference quartz sample. This shows substantial discrepancies in the erosion characteristics for the samples of batch *19WSi-3x*, even though they originate from the same production process.

In addition to the successful completion of the main task described above, also a comparison of experimental results obtained via the *Linear Track* approach versus numerical data originating from *TRI3DYN* was executed. For values regarding the target sputter yield Y_T, results were in good agreement for very smooth surfaces only, while all other simulated values were considerably lower than the ones calculated on the basis of experimental data and showed a stronger dependence on surface roughness R_q. In addition, the reconstructed profiles of the catcher yield Y_C were more than a order of magnitude lower than measured with the catcher QCM. By rescaling these values, a comparison of the individual tendencies was feasible, showing a good agreement between the smooth sample *19WSi-3b* ($R_q = 22$ nm) and a virtual surface with $R_q = 10$ nm in figure 6.2. Nevertheless, this comparison highlighted limitations of *TRI3DYN* simulations and encourages further benchmark studies. One approach could be to not only model the roughness value R_q, but also trying to match the surface inclination angle distribution of a given experimental sample. Still, the small computational volume remains as a significant limitation of this code, especially when surface features on the μm scale become bigger than the lateral expansion of the simulated surface. Additional comparison studies with other three-dimensional codes like *SDTrimSP-3D* may reveal further insights.

During the execution of this project, ideas for further experimental campaigns arose, which could provide opportunities for future studies or subsequent master projects. In general, more experimental data for ion incidence angles different than 60° would be favourable in order to substantiate results obtained during this thesis. In addition, an investigation via varia-

tion of the incident ion energy may offer more detailed insights. Also other materials like molybdenum or beryllium could be a target for future studies, since they are also candidates for utilisation as a first wall material [49, 50]. Long term studies could also focus on the investigation of surface modification effects, which would demand substantially higher values of total ion fluence compared to the levels reached during experiments in this thesis. Another experimental study could focus on the influence of 'lost' sputtered particles, which were not able to get caught along the described *Circular Track* positions (compare chapter 5). If a rough sample shows a strong sputter preference along the surface normal direction, it can be estimated that most of the atoms were indeed caught inside the catcher QCM solid angle. For samples with a very homogeneous emittance of particles over a wide range of directions from the target, particles may propagate also below or above the QCM position track and would therefore not contribute to the catcher yield tendency. If these particles can be taken into account, an increase of the catcher QCM accuracy might lead to deeper insights into the process of rough surface sputtering.

Acknowledgements

Die folgenden Zeilen sind all jenen Personen gewidmet, die mich im Laufe der letzten Monate und darüber hinaus auf dem Weg zu meinem Studienabschluss begleitet und unterstützt haben.

Zu Beginn möchte ich meinen Eltern Berndt und Gabriele, meiner Schwester Melanie und meinen Großeltern Udo und Rosmarie für die stetige Unterstützung in allen Lebenslagen herzlich danken. Euer ehrlicher Rat, verlässliche Hilfe und Wertschätzung waren wichtige Quellen für meinen Antrieb und gaben mir ein Fundament, von dem ich mein Studium von Beginn an aufbauen konnte.
Insbesondere möchte ich Herrn Prof. Dr. Friedrich Aumayr für die Ermöglichung dieser Diplomarbeit danken! In den vergangenen Monaten durfte ich im Zuge dieser Arbeit viele Herausforderungen meistern und Impressionen sammeln, die erst durch deine Unterstützung möglich wurden. Neben der täglichen Förderung im Rahmen dieser Diplomarbeit profitierte ich sehr von den beiden Forschungsaufenthalten in Uppsala und dem Studienaufenthalt in Garching. Deine Kommunikation auf Augenhöhe sowie ein offenes Ohr für die vielseitigen Anliegen von Kolleginnen und Kollegen sind ein starkes Asset für diese Forschungsgruppe.
Mein ausdrücklicher Dank gilt auch meinem Projektbetreuer, Herrn Ing. Dipl. Ing. Reinhard Stadlmayr. Seit ich im Jahre 2017 unter deiner Regie zum ersten Mal mit Ionen schießen durfte, habe ich sehr viel von dir gelernt. Deine Herangehensweise beim Lösen technischer und wissenschaftlicher Herausforderungen, deine realistische Einstellung und dein ruhiges Gemüt sind mir nach wie vor ein großes Vorbild!
Darüber hinaus möchte ich auch allen weitern Leuten in der Forschungsgruppe danken, die mich durch die tägliche Zusammenarbeit, interessante Diskussionen, kollegiale Hilfe und viele unterhaltsame Gespräche bereichert haben: Anna Niggas, Paul Szabo, Gabriel Szabo, Richard Wilhelm, Janine Schwestka, Martin Müller, Herbert Biber, Lidija Radovanovic, Waldemar Sartison, Georg Harrer, Lea Fuchs, Daniel Mayer und Johanna Fries. Ihr habt meinen Alltag, insbesondere im vergangenen Jahr maßgeblich geprägt und ich freue mich, dass ich auch in Zukunft Teil dieser Forschungsgruppe sein darf!
Zudem möchte ich den Herren Leonard Raumann und Dr. Jan Coenen für die Beschichtung der Wolframproben danken. Furthermore, I want to express my gratitude towards Karim Kantre, Dr. Marcos Moro and Prof. Dr. Daniel Primetzhofer, who enabled the elemental characterisation of the tungsten samples and also provided me the opportunity to gain experiences via scientific collaborations in an international research team.

List of Abbreviations

IEA International Energy Agency

Mtoe Megaton oil equivalents

OECD Organisation for Economic Co-operation and Development

ITER International Thermonuclear Experimental Reactor; also latin word for "The Way"

D-T deuterium-tritium

TOKAMAK Toroidal Chamber with Magnetic Coils (original acronym based on Russian)

DEMO DEMOnstration Power Plant

QCM Quartz Crystal Microbalance

RMS Root Mean Square

BCA Binary Collision Approximation

UHV Ultra High Vacuum

CAD Computer Aided Design

BNC Bayonet Neill Concelman - Type of connector for electric cables

PID Proportional Integral Differential - controller

CVD Chemical Vapour Deposition

AFM Atomic Force Microscopy

CFM Con-Focal Microscopy

CCD Charge Coupled Device (-Camera)

LED Light Emmiting Diode

IAP Institute for Applied Physics, TU WIEN

TU WIEN Technical University of Vienna, Austria

FZJ Forschungszentrum Jülich

IPP Garching Max-Planck Institute for Plasma Physics, Garching

FWHM Full Width Half Maximum

ERDA Elastic Recoil Detection Analysis

AC Alternating Current

MeV mega electron volt

eV electron volt

RBS Rutherford Backscattering Spectroscopy

Bibliography

[1] J. A. J. Gowlett. The discovery of fire by humans: A long and convoluted process. *Philosophical Transactions of the Royal Society B: Biological Sciences*, 371 (2016), 20150164.

[2] F. Birol. Key World Energy Statistics. *International Energy Agency*, (2019).

[3] J. Yang. *Deuterium: Discovery and Applications in Organic Chemistry*. Elsevier Inc., (2016).

[4] F. A. Hernández and P. Pereslavtsev. First principles review of options for tritium breeder and neutron multiplier materials for breeding blankets in fusion reactors. *Fusion Engineering and Design*, 137 (2018), 243.

[5] L. Rodríguez-Penalonga and B. Yolanda Moratilla Soria. A review of the nuclear fuel cycle strategies and the spent nuclear fuel management technologies. *Energies*, 10 (2017), 1235.

[6] ITER. Official Website. *https://www.iter.org/*, accessed 2019-11-10.

[7] W. Demtröder. *Experimental-Physik 4*. Springer-Verlag, (2014).

[8] H. A. Bethe. Energy Production in Stars. *Physical Review*, 55 (1939), 434.

[9] N. Tsoulfanidis. *Nuclear Energy*. Springer, (2018).

[10] U. Stroth. *Plasmaphysik*. Springer Spektrum, (2018).

[11] T. Casper, Y. Gribov, A. Kavin, V. Lukash, R. Khayrutdinov, H. Fujieda and C. Kessel. Development of the ITER baseline inductive scenario. *Nuclear Fusion*, 54 (2014), 013005.

[12] E. A. Azizov. Tokamaks: from A D Sakharov to the present (the 60-year history of tokamaks). *Physics-Uspekhi*, 55 (2012), 190.

[13] R. Neu, A. Kallenbach, M. Balden, V. Bobkov, J. W. Coenen, R. Drube, R. Dux, H. Greuner, A. Herrmann, J. Hobirk, H. Höhnle, K. Krieger, M. Kočan, P. Lang, T. Lunt, H. Maier, M. Mayer, H. W. Müller, S. Potzel, T. Pütterich and J. M. Rapp. Overview on plasma operation with a full tungsten wall in ASDEX Upgrade. *Journal of Nuclear Materials*, 438 (2013), 534.

[14] H. Urano, M. Nakata, N. Aiba, H. Kubo, M. Honda, N. Hayashi, M. Yoshida and Y. Kamada. Roles of argon seeding in energy confinement and pedestal structure in JT-60U. *Nuclear Fusion*, 55 (2015), 033010.

[15] H. Zohm, F. Träuble, W. Biel, E. Fable, R. Kemp, H. Lux, M. Siccinio and R. Wenninger. A stepladder approach to a tokamak fusion power plant. *Nuclear Fusion*, 57 (2017), 086002.

[16] EUROfusion. Official Website. *https://www.euro-fusion.org/*, accessed 2019-11-10.

[17] P. Sigmund. *Sputtering by Particle Bombardment - Theoretical concepts*. Springer-Verlag, (1981).

[18] W. Eckstein, C. Garciá-Rosales, J. Roth and J. László. Threshold energy for sputtering and its dependence on angle of incidence. *Nuclear Inst. and Methods in Physics Research, B*, 83 (1993), 95.

[19] C. Cupak. *Bachelor Thesis: Influence of Surface Structure Modifications on the Sputter Yield of Iron by monoenergetic Argon Ions*, TU Vienna, IAP, (2017).

[20] R. Stadlmayr, P. S. Szabo, C. Cupak, D. Mayer, T. Dittmar, L. Bischof, S. Möller, M. Rasinsky, R. A. Wilhelm, W. Möller and F. Aumayr. Sputtering of nanostructured tungsten and comparison to modelling with TRI3DYN (submitted). *Journal of Nuclear Materials*, (2019).

[21] M. Küstner, W. Eckstein, V. Dose and J. Roth. The influence of surface roughness on the angular dependence of the sputter yield. *Nuclear Instruments and Methods in Physics Research Section B: Beam Interactions with Materials and Atoms*, 145 (1998), 320.

[22] D. N. Ruzic and H. K. Chiu. Modeling of particle-surface reflections including surface roughness characterized by fractal geometry. *Journal of Nuclear Materials*, 162-164 (1989), 904.

[23] G. Z. Li, T. S. Matlock, D. M. Goebel, C. A. Dodson, C. S. R. Matthes, N. M. Ghoniem and R. E. Wirz. In situ plasma sputtering and angular distribution measurements for structured molybdenum surfaces. *Plasma Sources Science and Technology*, 26 (2017), 065002.

[24] F. Aumayr and H. P. Winter. Potential sputtering. *Philosophical Transactions of the Royal Society A: Mathematical, Physical and Engineering Sciences*, 362 (2004), 77.

[25] B. M. Berger, R. Stadlmayr, D. Blöch, E. Gruber, K. Sugiyama, T. Schwarz-Selinger and F. Aumayr. Erosion of Fe-W model system under normal and oblige D ion irradiation. *Nuclear Materials and Energy*, 12 (2017), 42.

[26] B. M. Berger, R. Stadlmayr, G. Meisl, M. Čekada, C. Eisenmenger-Sittner, T. Schwarz-Selinger and F. Aumayr. Transient effects during erosion of WN by deuterium ions studied with the quartz crystal microbalance technique. *Nuclear Instruments and Methods in Physics Research Section B: Beam Interactions with Materials and Atoms*, 382 (2016), 82.

[27] P. S. Szabo, R. Chiba, H. Biber, R. Stadlmayr, B.M. Berger, D. Mayer, A. Mutzke, M. Doppler, M. Sauer, J. Appenroth, J. Fleig, A. Foelske-Schmitz, H. Hutter, K. Mezger, H. Lammer, A. Galli, P. Wurz and F. Aumayr. Solar wind sputtering of wollastonite as a lunar analogue material – Comparisons between experiments and simulations. *Icarus*, 314 (2018), 98.

[28] R. Stadlmayr, P. S. Szabo, B. M. Berger, C. Cupak, R. Chiba, D. Blöch, D. Mayer, B. Stechauner, M. Sauer, A. Foelske-Schmitz, M. Oberkofler, T. Schwarz-Selinger, A. Mutzke, and F. Aumayr. Fluence dependent changes of surface morphology and sputtering yield of iron: Comparison of experiments with SDTrimSP-2D. *Nuclear Instruments and Methods in Physics Research Section B: Beam Interactions with Materials and Atoms*, 430 (2018), 42.

[29] G. Sauerbrey. Verwendung von Schwingquarzen zur Wägung dünner Schichten und zur Mikrowägung. *Zeitschrift für Physik*, 155 (1959), 206.

[30] G. Hayderer, M. Schmid, P. Varga, H. P. Winter and F. Aumayr. A highly sensitive quartz-crystal microbalance for sputtering investigations in slow ion-surface collisions. *Review of Scientific Instruments*, 70 (1999), 3696.

[31] P. S. Szabo. *Diploma Thesis: Experimental and Simulated Sputtering of Gold , Iron and Wollastonite with a Catcher-QCM Setup*, TU Vienna, IAP, (2017).

[32] D. S. Stevens and H. F. Tiersten. An analysis of doubly rotated quartz resonators utilizing essentially thickness modes with transverse variation. *Journal of the Acoustical Society of America*, 79 (1986), 1811.

[33] L. Bachmann and J. Shin. Measurement of the sticking coefficients of silver and gold in an ultrahigh vacuum. *Journal of Applied Physics*, 37 (1966), 242.

[34] W. Möller. TRI3DYN – Collisional computer simulation of the dynamic evolution of 3-dimensional nanostructures under ion irradiation. *Nuclear Instruments and Methods in Physics Research Section B: Beam Interactions with Materials and Atoms*, 322 (2014), 23.

[35] W. Möller and W. Eckstein. Tridyn — A TRIM simulation code including dynamic composition changes. *Nuclear Instruments and Methods in Physics Research Section B: Beam Interactions with Materials and Atoms*, 2 (1984), 814.

[36] How to Generate Random Surfaces in COMSOL Multiphysics. Comsol Official Website. *https://www.comsol.com/blogs/how-to-generate-random-surfaces-in-comsol-multiphysics/*, accessed 2019-11-29.

[37] R. Stadlmayr. *Diploma Thesis: Erosion of Tungsten Nitride and Iron-Tungsten Surfaces under Deuterium Ion Impact*, TU Vienna, IAP, (2016).

[38] D. Mayer. *Diploma Thesis (to be published)*, TU Vienna, IAP, (2019).

[39] A. Rahtu and M. Ritala. Compensation of temperature effects in quartz crystal microbalance measurements. *Applied Physics Letters*, 80 (2002), 521.

[40] KVG Quartz Crystal Technology GmbH. Official Website. *https://www.kvg-gmbh.de/*, accessed 2019-11-10.

[41] G. Binnig, C. F. Quate and Ch. Gerber. Atomic Force Microscopy. *Physical Review Letters*, 56 (1986), 930.

[42] Gwyddion. Official Website. *http://gwyddion.net/*, accessed 2019-11-10.

[43] P. Conn. *Techniques in Confocal Microscopy*. Elsevier Academic Press, (2010).

[44] M. V. Moro, R. Holeňák, L. Zendejas Medina, U. Jansson, and D. Primetzhofer. Accurate high-resolution depth profiling of magnetron sputtered transition metal alloy films containing light species: A multi-method approach. *Thin Solid Films*, 686 (2019), 137416.

[45] J. R. Tesmer, M. Nastasi and J. C. Barbour. *Handbook of modern ion beam materials analysis*. Material Research Society, Pittsburgh, PA, (1995).

[46] J. A. Yarmoff and F. Read McFeely. Mechanism for chemical-vapor deposition of tungsten on silicon from tungsten hexafluoride. *Journal of Applied Physics*, 63 (1988), 5213.

[47] C. Nordling and J. Österman. *Physics handbook for science and engineering*. Studentlitteratur, (2008).

[48] Y. Li, Y. Yang, M. P. Short, Z. Ding, Z. Zeng and J. Li. Ion radiation albedo effect: influence of surface roughness on ion implantation and sputtering of materials. *Nuclear Fusion*, 57 (2016), 6110.

[49] M. Keilhacker. Overview of results from the JET tokamak using a beryllium first wall. *Physics of Fluids B: Plasma Physics*, 2 (1990), 1291.

[50] M. Chen, J. Roszell, E. V. Scoullos, C. Riplinger, B. E. Koel and E. A. Carter. Effect of Temperature on the Desorption of Lithium from Molybdenum (110) Surfaces: Implications for Fusion Reactor First Wall Materials. *Journal of Physical Chemistry B*, 120 (2016), 6110.

Appendix

Project Statistics

In this part of the appendix, a short overview about the total time spent for individual tasks of this thesis is shown. In total, 1605 hours of work were invested within the frame of this project. A declaration of the tasks is provided in the caption of figure 7.1. A significant amount of time was spent for categories 5 and 7, which highlights the applied experimental frame of this thesis.

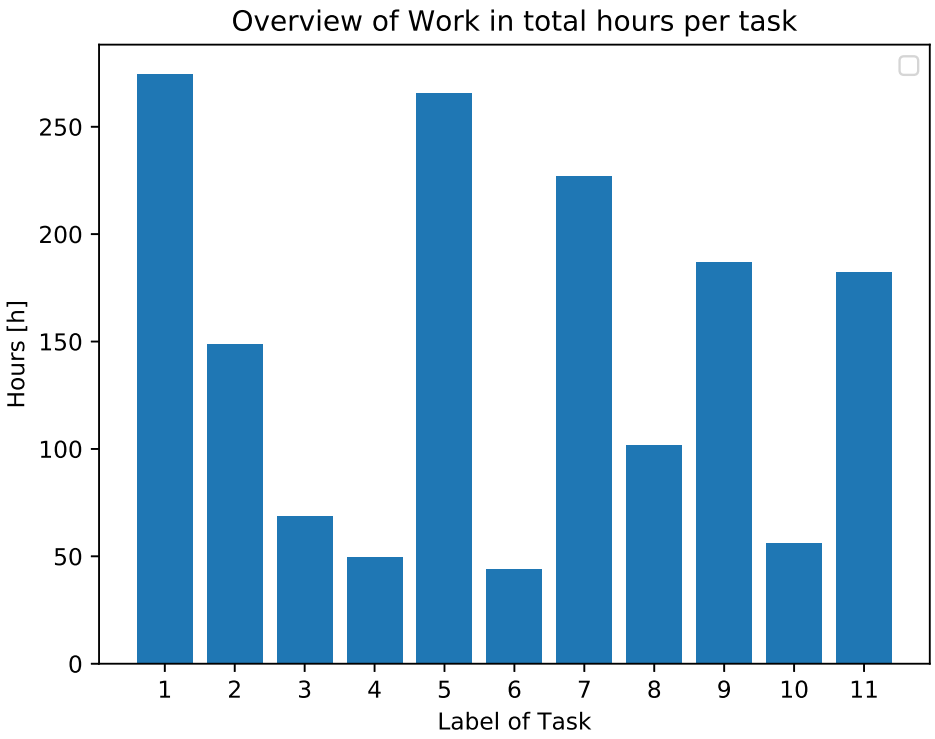

Figure 7.1 – Overview of total working hours per individual task. Declaration of the task labels: (1)-Organisatoral/Meetings, (2)-Literature research, (3)-Hardware development, (4)-Programming, (5)-Practical work/Testing, (6)-Simulations, (7)-Experiments, (8)-Data evaluation, (9)-Documentation, (10)-Supporting project students. (11)-Lunch conversations

Ion Source parameter settings

In the following, a table with commonly utilised ion source parameters is added for future ion beam investigations. These values were found to deliver both satisfying high ion beam currents and also a comparable homogeneous beam profile across the scanning area. It has to be mentioned, that these values were rather the starting point for further fine tuning.
It has to be noted, that parameter *Pos X* modifies not to the horizontal, but to the vertical deflection of the ion beam. Correspondingly, *Pos Y* is indicating horizontal variation of the beam position and parameters *Width X*, *Width Y* apply ion beam scanning in the respective plane. The Wienfilter Type is actually not a parameter, but a certain type of permanent magnet necessary for filtering the Ar^{1+} ion beam. The value of L was chosen 81 or 88 mm, for measurements following the *Linear* or *Circular Track* approach, respectively.

Parameter	**Value**
Energy	2000 eV
Extractor	92 %
Focus 1	81.2 %
Focus 2	4.5 %
I Emmission	10 mA
Wienfilter Type	strong, 0.46 T
Wienfilter Mass	4.87
Stigmator	7.8
Pos X	0.5 mm
Width X	5 mm
Pos Y	0.5 mm
Width Y	2.5 mm
L	81 or 88 mm
I Limit	5.5 A
I Standby	3 A

Table 7.1 – Table with casual ion source parameters

Positioning Table

In the following, a table for positioning during the *Circular Track* catcher QCM approach is added. It has to be noted, that these values are only valid for obtaining a distance (radius of circular path) $d = 21.4$ mm, while the zero-tilt position on the y-nonius has to be exactly 9 mm (hardware mounting criteria).

Interactive Table for Circular Track Cacher QCM Measurements (d = 21.4mm)				
Tilt Angle	**Position y - Nonius [0,0-12,0] mm**	**Position X-Nonius**	**Position Y-Nonius [100-0] mm**	**Position Z-Nonius**
-25	13,22	-4,04	56,99	1,5 (schwarz)
-20	12,45	-2,32	57,71	1,5 (schwarz)
-15	11,63	-0,54	58,27	1,5 (schwarz)
-7,5	10,36	2,21	58,82	1,5 (schwarz)
-5	9,91	3,13	58,92	1,5 (schwarz)
0	9,00	5,00	59,00	1,5 (schwarz)
5	8,08	6,87	58,92	1,5 (schwarz)
10	7,14	8,72	58,67	1,5 (schwarz)
15	6,20	10,54	58,27	1,5 (schwarz)
20	5,27	12,32	57,71	1,5 (schwarz)
25	4,35	14,04	56,99	1,5 (schwarz)
30	3,45	15,70	56,13	1,5 (schwarz)
35	2,58	17,27	55,13	1,5 (schwarz)
40	1,76	18,76	53,99	1,5 (schwarz)
45	0,98	20,13	52,73	1,5 (schwarz)
50	0,26	21,39	51,36	1,5 (schwarz)
55	-0,39	22,53	49,87	1,5 (schwarz)
60	-0,98	23,53	48,30	1,5 (schwarz)
65	-1,49	24,39	46,64	1,5 (schwarz)
70	-1,91	25,11	44,92	1,5 (schwarz)
75	-2,24	25,67	43,14	1,5 (schwarz)
80	-2,49	26,07	41,32	1,5 (schwarz)

Deklaration:	X-Nonius:	Position of quartz along ion beam direction
	Y-Nonius:	Position of quartz perpendicular to ion beam direction
	Z-Nonius:	Position vertically, here always in centre x-y plane of laboratory axis
	y-Nonius:	Linear movement for tilting the catcher quartz; 9mm is corresponding to 0°

Figure 7.2 – Table for catcher QCM positioning with radius 21.4 mm.

Technical Drawings

In the following, technical drawings of the new catcher QCM design are added to provide a basis for future developments. These drawings were utilised for manufacturing in the in-house IAP TU WIEN workshop. The quartz crystal fixation mechanism was adopted from earlier QCM versions, therefore only a assembly drawing is provided here. As motivated in chapter 3.3, the holes for the bearing of the tilt mechanism (see drawing 2 and 4, diameters 2.40 mm) may be drilled with only 2 mm for future projects in order to have less gap. The fabrication of the hardware parts was done by *Herbert Schmidt* and *Rainer Gärtner*, special thanks for your help!

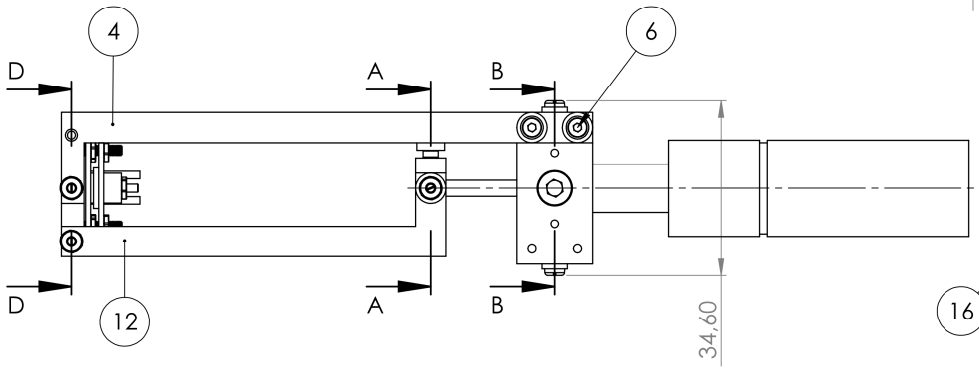

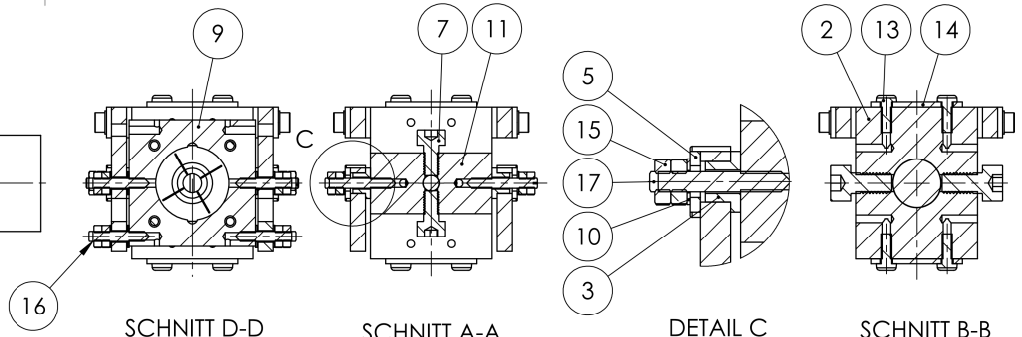

SCHNITT D-D
MAßSTAB 1 : 1

SCHNITT A-A
MAßSTAB 1 : 1

DETAIL C
MAßSTAB 2 : 1

SCHNITT B-B
MAßSTAB 1 : 1

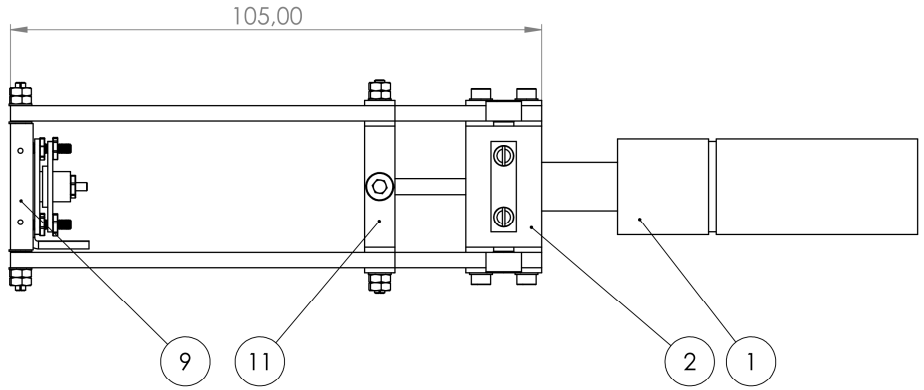

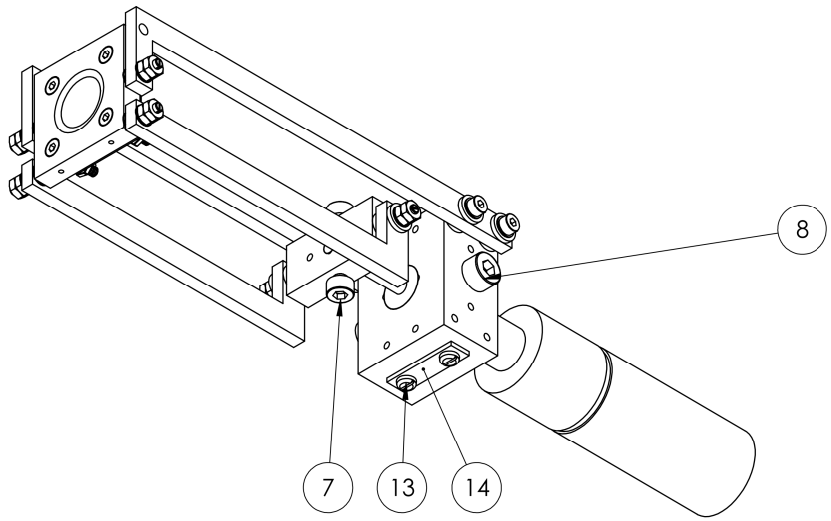

POS-NR.	BENENNUNG	BESCHREIBUNG	MENGE
1	Welle_Manipulator	Darstellung Wellenansatz	1
2	Befestigung_Welle95	Zeichnung 1	1
3	M2_Keramikhut	Zur Isolation - Normteil	6
4	Fixation_L	Zeichnung 2	2
5	WasherM2Ceramic	Zur Isolation - Normteil	6
6	ISO 4762 M2 x 8 - 8S	M2 Schraube zur Befestigung	4
7	ISO 4762 M3 x 6 - 6S	M3 Schraube zur Positionierung	2
8	ISO 4762 M4 x 8 - 8S	M4 Schraube zur Positionierung	2
9	halter_neigbar	Sub - Baugruppe 1	1
10	Washer ISO 7092 - 2	Beilagscheibe	14
11	Befestigung_Welle315	Zeichnung 3	1
12	Fixation_L3	Zeichnung 4	2
13	ISO 1580 - M2 x 6 - 6N	M2 Schraube zur Befestigung	4
14	Klammer	Zeichnung 5	2
15	ISO - 4032 - M2 - D - N	M2 Mutter	12
16	Madenschraube_12mm	Gewindestift M2x12mm	4
17	Madenschraube_14mm	Gewindestift M2x14mm	2

WENN NICHT ANDERS DEFINIERT:
BEMASSUNGEN SIND IN MILLIMETER
OBERFLÄCHENBESCHAFFENHEIT:
TOLERANZEN:
LINEAR:
WINKEL:

OBERFLÄCHENGÜTE:

ENTGRATEN UND SCHARFE KANTEN BRECHEN

ZEICHNUNG NICHT SKALIEREN

ÄNDERUNG

AG Aumayr - Christian Cupak

	NAME	SIGNATUR	DATUM
GEZEICHNET			
GEPRÜFT			
GENEHMIGT			
PRODUKTION			
QUALITÄT			

BENENNUNG:

Gesamtbaugruppe

WERKSTOFF:

ZEICHNUNGSNR.

Assembly

A3

GEWICHT:

MASSSTAB:1:2

BLATT 1 VON 1

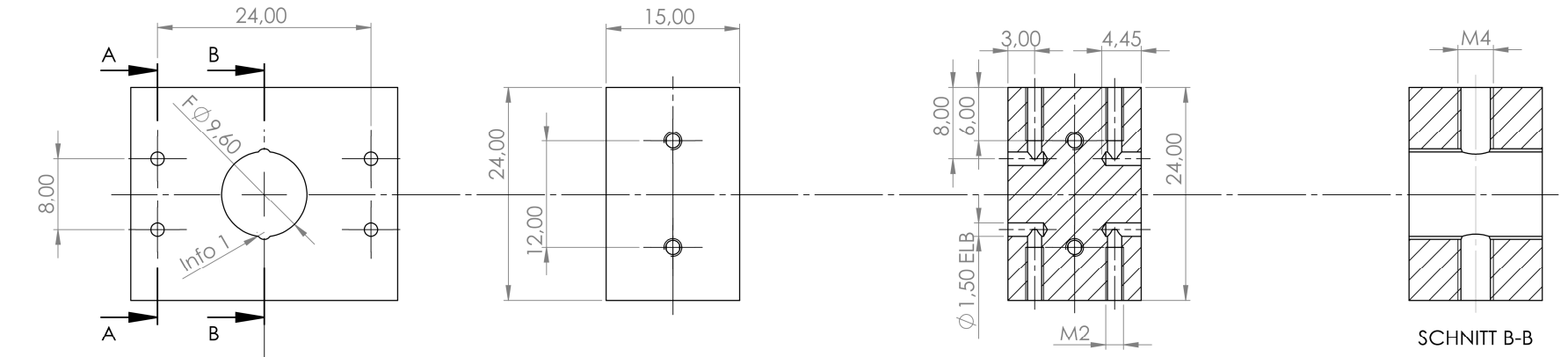

SCHNITT A-A

SCHNITT B-B

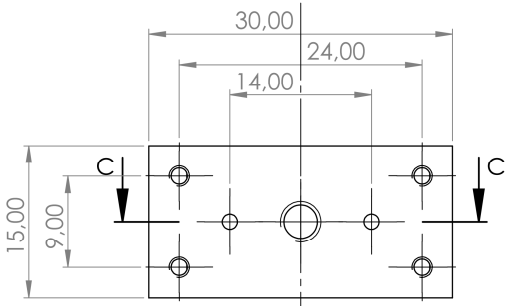

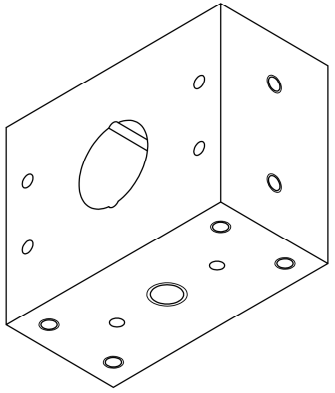

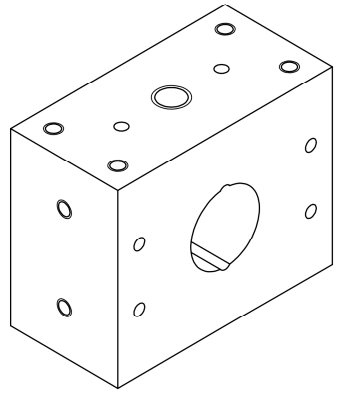

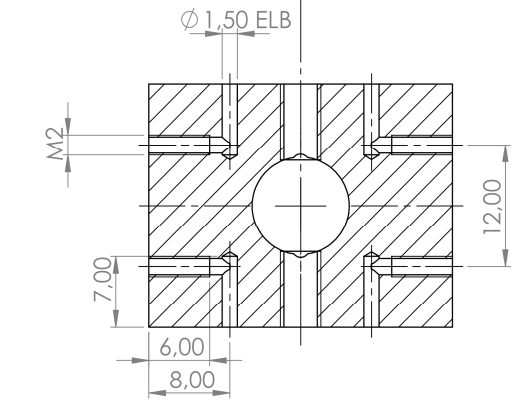

SCHNITT C-C

∅1,5 ELB ... Entlüftungsbohrung
Info 1 ... Entlüftungsfuge fertigen
F∅9,60 ... Funktionsmaß, soll auf Wellenabsatz aufschiebbar sein

WENN NICHT ANDERS DEFINIERT: BEMASSUNGEN SIND IN MILLIMETER OBERFLÄCHENBESCHAFFENHEIT: TOLERANZEN: LINEAR: WINKEL:		OBERFLÄCHENGÜTE:		ENTGRATEN UND SCHARFE KANTEN BRECHEN	ZEICHNUNG NICHT SKALIEREN	ÄNDERUNG	
					AG Aumayr - Christian Cupak		
	NAME	SIGNATUR	DATUM		BENENNUNG:		
GEZEICHNET					Befestigung Welle 9.5		
GEPRÜFT							
GENEHMIGT							
PRODUKTION							
QUALITÄT				WERKSTOFF:	ZEICHNUNGSNR.		A3
				Edelstahl (A4)	1		
				GEWICHT:	MASSSTAB:2:1	BLATT 1 VON 1	

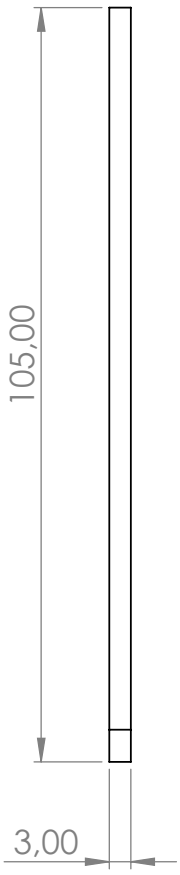

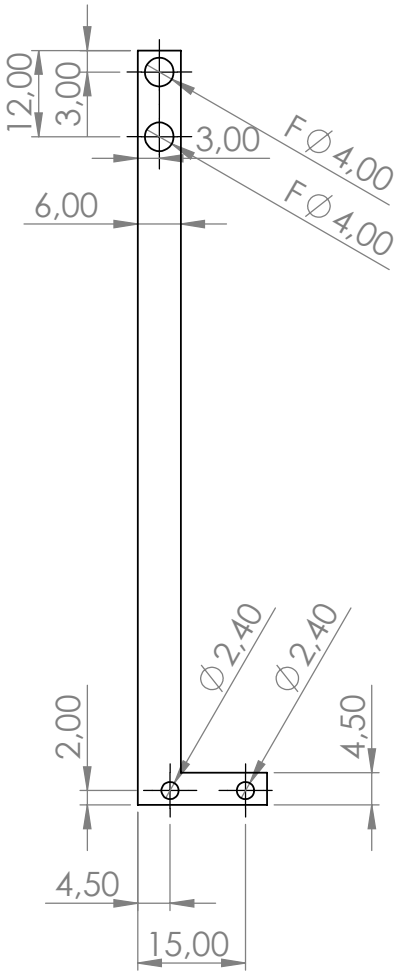

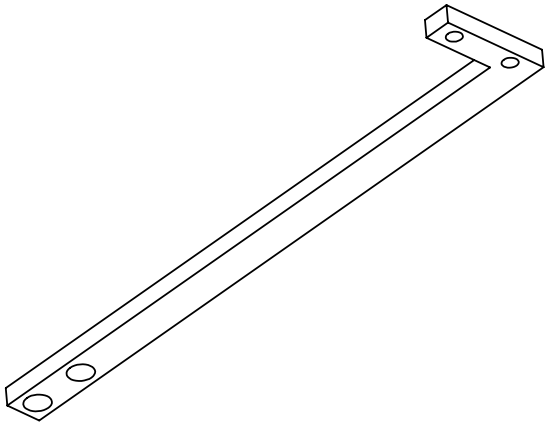

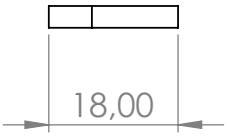

F 4,00 ... Funktionsmaß - Keramikhut hat weiten Toleranzbereich

WENN NICHT ANDERS DEFINIERT: BEMASSUNGEN SIND IN MILLIMETER OBERFLÄCHENBESCHAFFENHEIT: TOLERANZEN: LINEAR: WINKEL:	OBERFLÄCHENGÜTE:	ENTGRATEN UND SCHARFE KANTEN BRECHEN 2 STÜCK	ZEICHNUNG NICHT SKALIEREN ÄNDERUNG V2
			AG Aumayr - Christian Cupak

	NAME	SIGNATUR	DATUM
GEZEICHNET			
GEPRÜFT			
GENEHMIGT			
PRODUKTION			
QUALITÄT			

BENENNUNG:

Stützbalken 1

WERKSTOFF: Edelstahl (A4)	ZEICHNUNGSNR. 2	A4
GEWICHT:	MASSSTAB:1:1	BLATT 1 VON 1

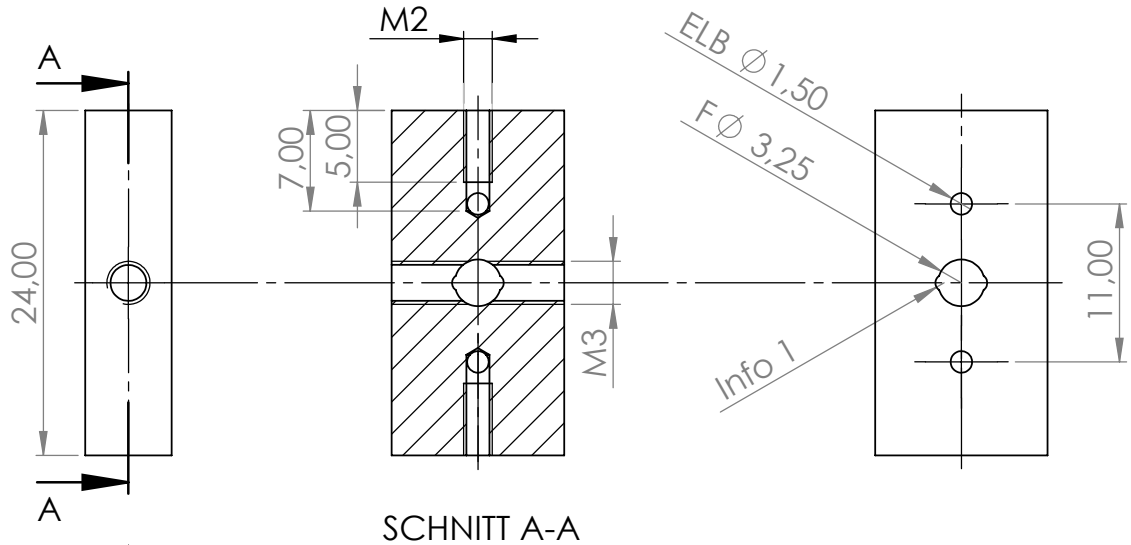

SCHNITT A-A
MAßSTAB 2 : 1

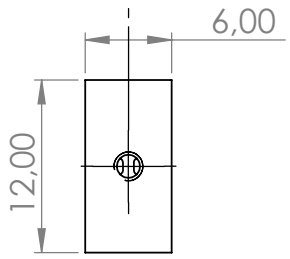

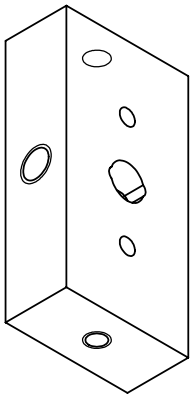

Info 1 ... Entlüftungsfuge fertigen
ELB ∅ 1,5 ... Entlüftungsbohrung
F ∅ 3,25 ... Funktionsmaß, soll auf kleinen Wellenabsatz aufschiebbar sein

WENN NICHT ANDERS DEFINIERT: BEMASSUNGEN SIND IN MILLIMETER OBERFLÄCHENBESCHAFFENHEIT: TOLERANZEN: LINEAR: WINKEL:	OBERFLÄCHENGÜTE:	ENTGRATEN UND SCHARFE KANTEN BRECHEN	ZEICHNUNG NICHT SKALIEREN	ÄNDERUNG		
			AG Aumayr - Christian Cupak			
	NAME	SIGNATUR	DATUM			BENENNUNG:
GEZEICHNET						Befestigung Welle 3.15
GEPRÜFT						
GENEHMIGT						
PRODUKTION						
QUALITÄT				WERKSTOFF: Edelstahl (A4)	ZEICHNUNGSNR. 3	A4
				GEWICHT:	MASSSTAB: 2:1	BLATT 1 VON 1

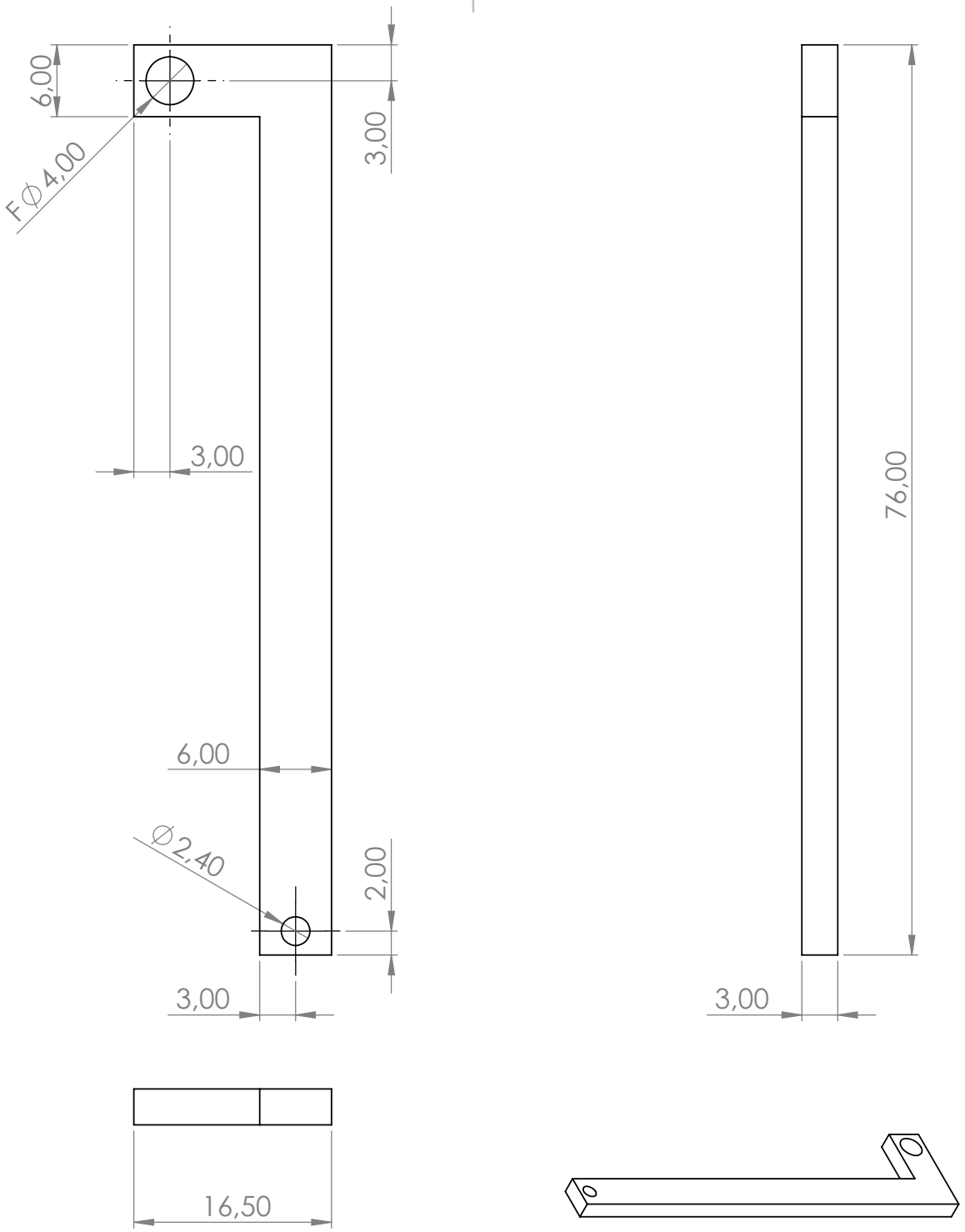

F Ø 4,00 ... Funktionsmaß - Keramikhut hat weiten Toleranzbereich

WENN NICHT ANDERS DEFINIERT: BEMASSUNGEN SIND IN MILLIMETER OBERFLÄCHENBESCHAFFENHEIT: TOLERANZEN: LINEAR: WINKEL:	OBERFLÄCHENGÜTE:	ENTGRATEN UND SCHARFE KANTEN BRECHEN 2 STÜCK	ZEICHNUNG NICHT SKALIEREN ÄNDERUNG V2 AG Aumayr - Christian Cupak

	NAME	SIGNATUR	DATUM
GEZEICHNET			
GEPRÜFT			
GENEHMIGT			
PRODUKTION			
QUALITÄT			

BENENNUNG:

Stützbalken 2

WERKSTOFF: Edelstahl (A4)	ZEICHNUNGSNR. 4	A4
GEWICHT:	MASSSTAB:2:1	BLATT 1 VON 1

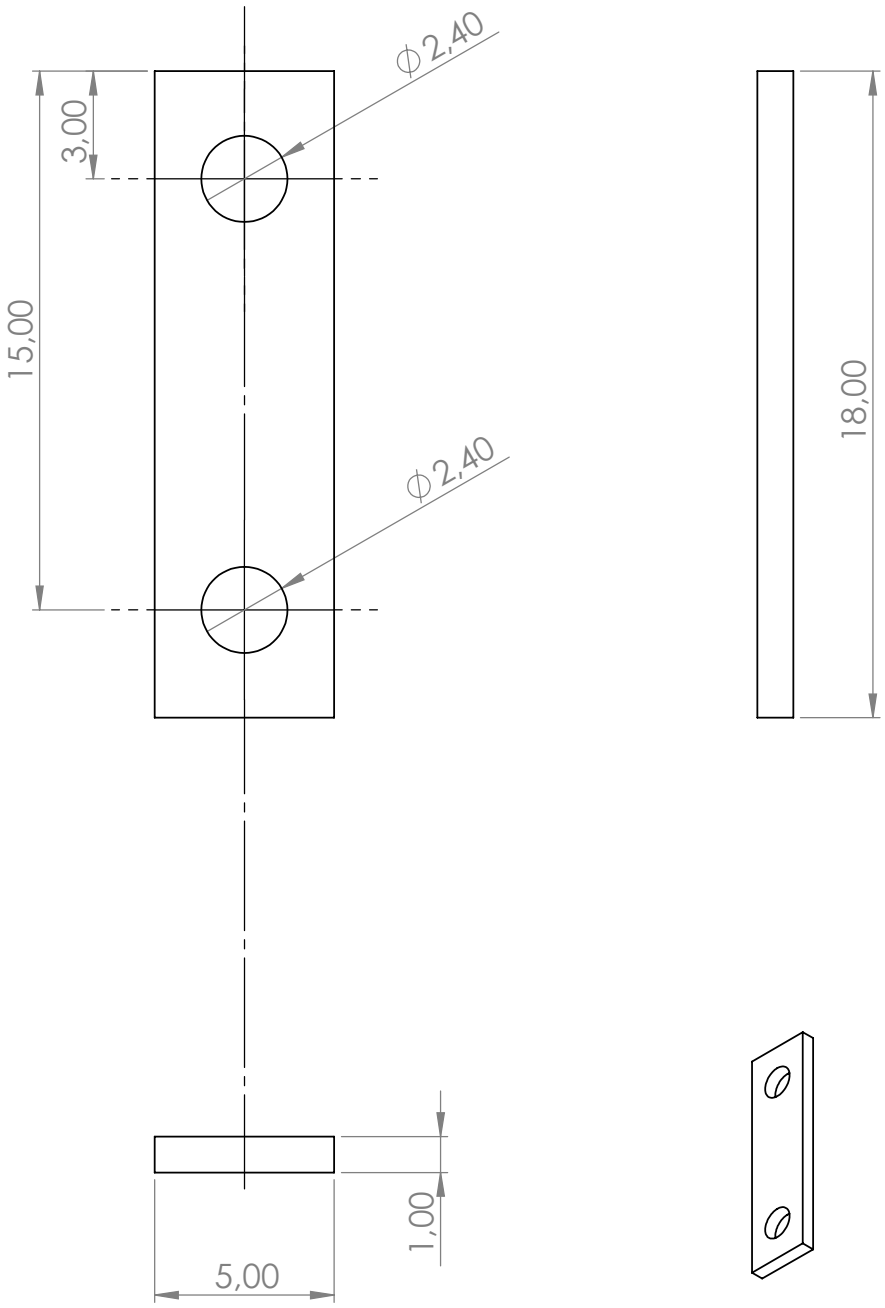

WENN NICHT ANDERS DEFINIERT: BEMASSUNGEN SIND IN MILLIMETER OBERFLÄCHENBESCHAFFENHEIT: TOLERANZEN: LINEAR: WINKEL:	OBERFLÄCHENGÜTE:	ENTGRATEN UND SCHARFE KANTEN BRECHEN	ZEICHNUNG NICHT SKALIEREN / ÄNDERUNG

AG Aumayr - Christian Cupak

	NAME	SIGNATUR	DATUM
GEZEICHNET			
GEPRÜFT			
GENEHMIGT			
PRODUKTION			
QUALITÄT			

BENNENNUNG: Kabel-Befestigungsklammer

WERKSTOFF: Edelstahl (A4)

ZEICHNUNGSNR. 5

A4

GEWICHT:

MASSSTAB:5:1

BLATT 1 VON 1

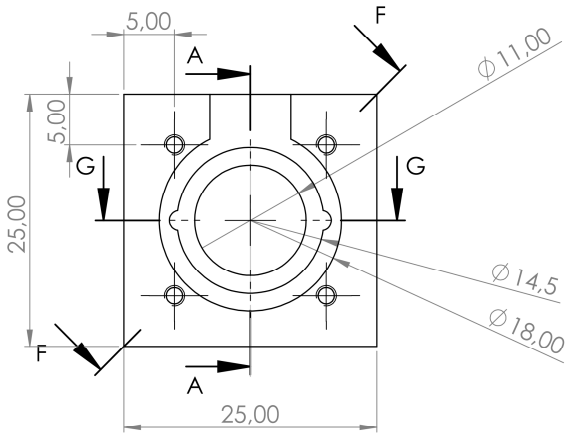

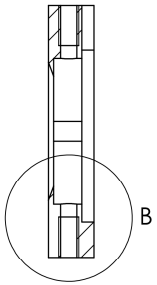

SCHNITT A-A
MAßSTAB 2 : 1

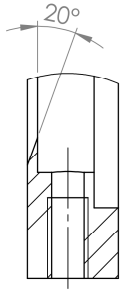

DETAIL B
MAßSTAB 4 : 1

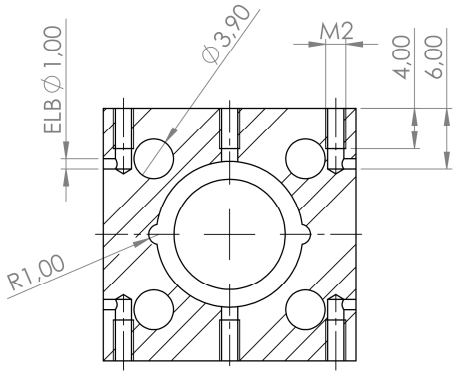

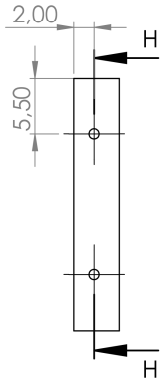

SCHNITT H-H
MAßSTAB 2 : 1

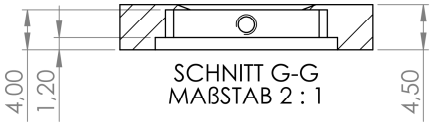

SCHNITT G-G
MAßSTAB 2 : 1

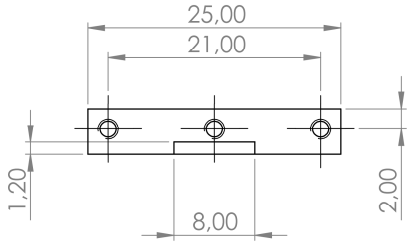

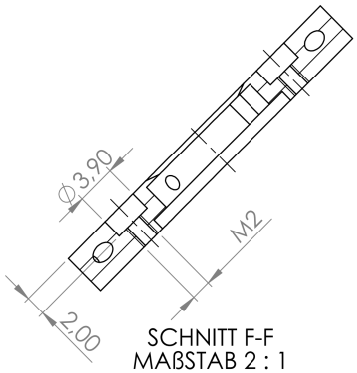

SCHNITT F-F
MAßSTAB 2 : 1

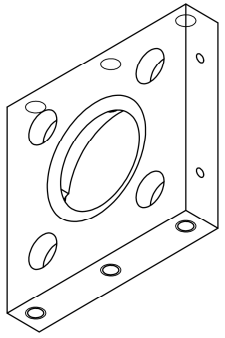

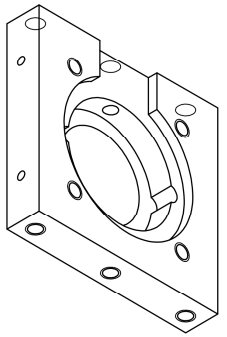

WENN NICHT ANDERS DEFINIERT: BEMASSUNGEN SIND IN MILLIMETER OBERFLÄCHENBESCHAFFENHEIT: TOLERANZEN: LINEAR: WINKEL:	OBERFLÄCHENGÜTE:				ENTGRATEN UND SCHARFE KANTEN BRECHEN	ZEICHNUNG NICHT SKALIEREN / ÄNDERUNG
						AG Aumayr - Christian Cupak
	NAME	SIGNATUR	DATUM			BENENNUNG: Quarzkristall Halter Frontplatte
GEZEICHNET						
GEPRÜFT						
GENEHMIGT						
PRODUKTION						
QUALITÄT				WERKSTOFF: Edelstahl A4		ZEICHNUNGSNR. 6 / A3
				GEWICHT:		MASSSTAB:5:1 / BLATT 1 VON 1

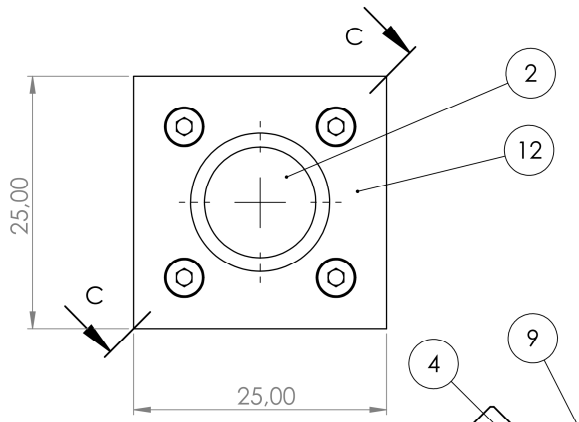

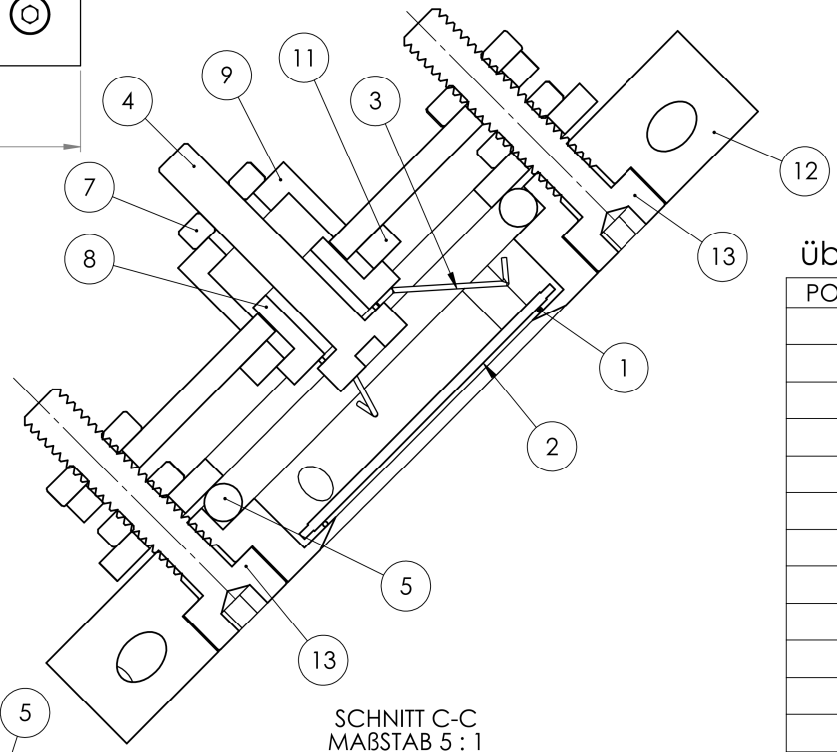

SCHNITT C-C
MAßSTAB 5 : 1

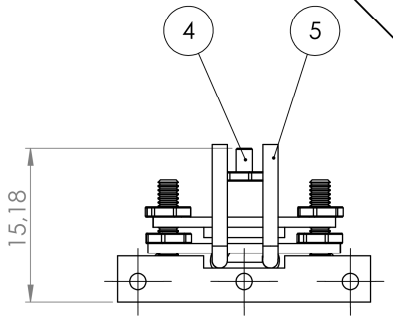

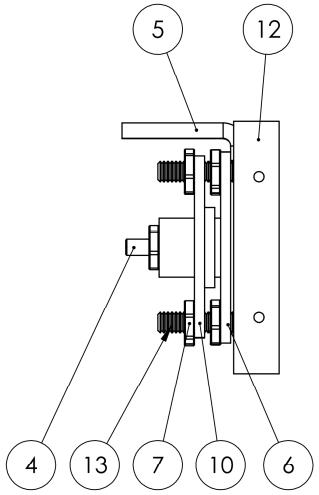

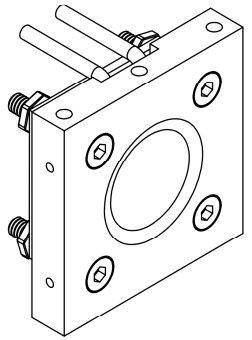

übernommen von früher konstruiertem QCM Konzept

POS-NR.	BENENNUNG	BESCHREIBUNG	MENGE
1	ring_gold	Goldring	1
2	quarz_gold	Quarzkristall	1
3	W_spring	Wolframfeder	1
4	SchraubeM2x10	Schraube M2x10	1
5	heitzdraht	Koaxial Heizdraht	1
6	deckel	Klemmplatte Koaxial Heizdraht	1
7	MutterM2	Mutter M2	9
8	buchse2mm	Keramik Buchse	1
9	huetchen2mm	Keramik Hütchen	1
10	halter feder	Halter Wolframfeder	1
11	scheibe_keramik	Distanzscheibe Keramik	1
12	front_neigbar	Zeichnung 6	1
13	ISO 4762 M2 x 10 - 10S	Schraube M2 x 10mm	4

WENN NICHT ANDERS DEFINIERT:
BEMASSUNGEN SIND IN MILLIMETER
OBERFLÄCHENBESCHAFFENHEIT:
TOLERANZEN:
LINEAR:
WINKEL:

OBERFLÄCHENGÜTE:

ENTGRATEN UND SCHARFE KANTEN BRECHEN

ZEICHNUNG NICHT SKALIEREN | ÄNDERUNG

AG Aumayr - Christian Cupak

	NAME	SIGNATUR	DATUM
GEZEICHNET			
GEPRÜFT			
GENEHMIGT			
PRODUKTION			
QUALITÄT			

BENENNUNG:
Sub Baugruppe

WERKSTOFF:

ZEICHNUNGSNR.
halter_neigbar

A3

GEWICHT:

MASSSTAB:2:1

BLATT 1 VON 1